
Development and Application of an Analysis of Axisymmetric Body Effects on Helicopter Rotor Aerodynamics Using Modified Slender Body Theory

Gloria Yamauchi and Wayne Johnson

July 1984



National Aeronautics and
Space Administration

Development and Application of an Analysis of Axisymmetric Body Effects on Helicopter Rotor Aerodynamics Using Modified Slender Body Theory

Gloria Yamauchi

Wayne Johnson, Ames Research Center, Moffett Field, California



National Aeronautics and
Space Administration

Ames Research Center
Moffett Field, California 94035



SYMBOLS

A	cross-sectional area of body
a	semimajor axis of ellipsoid
a	radius of sphere
a_0	parameter used in the modified slender body theory with tail correction
b	semiminor axis of ellipsoid
\bar{c}	blade mean chord, $\pi R/N$
c_d	rotor blade section drag coefficient
c.g.	center of gravity
c_l	rotor blade section lift coefficient
C_{m_c}	blade pitch moment divided by $\rho \Omega^2 R^4 \bar{c}$
C_{m_x}	blade flapwise bending moment divided by $\rho \Omega^2 R^4 \bar{c}$
C_{m_z}	blade edgewise bending moment divided by $\rho \Omega^2 R^4 \bar{c}$
c_p	surface pressure coefficient
C_P	power coefficient, $\frac{P}{\rho (\Omega R)^3 \pi R^2}$
C_{P_i}	induced power coefficient
$C_{P_{int}}$	interference power coefficient
C_{P_o}	profile power coefficient
C_T	rotor thrust divided by $\rho (\Omega R)^2 \pi R^2$
D	rotor equivalent drag, $\frac{P}{U_o} - PF$
e	eccentricity
f	function used in modified slender body theory with tail correction
K	factor needed to match maximum thickness for ellipsoids using modified slender body theory

\mathcal{K}	factor needed to match maximum thickness for pointed tail bodies using modified slender body theory
KN	factor needed to match maximum thickness for pointed-tail bodies using modified slender body theory with tail correction
l	body length
L/D	rotor lift-to-drag ratio
n	harmonic number
N	number of blades
N	number of steps in numerical integration in body analysis
P	rotor power
PF	propulsive force
q	strength of axial source distribution
R	radius of curvature of nose of ellipsoid
R	rotor radius
RCA	$1/2(RCN+RCT)$
RCN	radius of curvature of body nose
RCT	radius of curvature of body tail
r	radial coordinate, $(z^2 + y^2)^{1/2}$
r_o	radial coordinate defining body streamline
T	$2t$
t	maximum thickness of body (measured from body centerline)
U_o	free-stream velocity
U_r	radial velocity
(U_x, U_y, U_z)	velocity components in (x, y, z) coordinates
XE	amount of extension of body length
(X_F, Y_F, Z_F)	coordinate system with origin at c.g.
(X_S, Y_S, Z_S)	coordinate system with origin at hub position
(x, y, z)	coordinate system with origin at body nose

V_{int}	interference velocity
α	blade section angle of attack
α_S	shaft angle
α_{TPP}	tip-path-plane angle
β_{1c}	longitudinal tip-path-plane angle
β_{1s}	lateral tip-path-plane angle
θ_{1c}	lateral cyclic control angle
λ	induced velocity at rotor disk relative to shaft axes
λ_{int}	vertical interference inflow ratio
μ	advance ratio, $\frac{U_o}{\Omega R}$
(μ, ν, ω)	elliptic coordinate system
ξ	axial coordinate of source distribution
ξ^*	compressed coordinate
ξ_1, ξ_2	parameters used in the modified slender-body theory with tail correction
ρ	air density
σ	rotor solidity (total blade area divided by disk area)
ϕ	velocity potential of an axial source distribution
ψ	stream function of an axial source distribution
ψ	rotor blade azimuth position
Ω	rotor rotational speed

SUMMARY

A computationally efficient body analysis designed to couple with a comprehensive helicopter analysis is developed in order to calculate the body-induced aerodynamic effects on rotor performance and loads. A modified slender body theory is used as the body model. With the objective of demonstrating the accuracy, efficiency, and application of the method, the analysis at this stage is restricted to axisymmetric bodies at zero angle of attack. By comparing with results from an exact analysis for simple body shapes, it is found that the modified slender body theory provides an accurate potential flow solution for moderately thick bodies, with only a 10%-20% increase in computational effort over that of an isolated rotor analysis. The computational ease of this method provides a means for routine assessment of body-induced effects on a rotor. Results are given for several configurations that typify those being used in the Ames 40- by 80-Foot Wind Tunnel and in the rotor-body aerodynamic interference tests being conducted at Ames. A rotor-hybrid airship configuration is also analyzed.

INTRODUCTION

The aerodynamic interaction between the rotor and the fuselage of a helicopter requires careful consideration when assessing performance and loads. This interaction has been shown experimentally to have significant effects (e.g., in refs. 1 and 2). Ideally, analytical models of the rotor-induced effects at the body and the body-induced effects at the rotor need to be combined. Because of the complex nature of the flow field of a helicopter, however, the end result of such a combination would require the coupling of complex body and rotor computer codes in order to calculate the system behavior. Typical past efforts (refs. 3 and 4) have coupled potential flow panel methods for fuselage aerodynamic analysis with simplified rotor analytical models. For investigations emphasizing the rotor, an efficient analytical model for the fuselage is desirable, rather than a complex and time-consuming paneling code.

This paper presents the initial results of an investigation intended to develop an efficient body model for use in comprehensive helicopter analyses, such as CAMRAD (ref. 5), in order to calculate body-induced effects on rotor performance and loads. The requirement for efficiency does not, however, diminish to any degree the need to maintain the accuracy of the body flow field. Computational efficiency is usually achieved by using simple methods; in this case, a direct rather than an inverse or iterative method is desired. Slender body theory is the logical starting point for the analysis, but modifications to the theory will be required to achieve the accuracy desired for moderately thick bodies.

This investigation will ultimately lead to a general model for the body shape, and will include flows at nonzero angle of attack. The results of the present paper are the initial steps of the investigation, including (1) development of a model for a body of revolution at zero angle of attack; (2) demonstration of the accuracy and

limits of the model; and (3) calculations of the isolated body-induced effects on the rotor.

Ames Research Center is engaged in an experimental program to measure the aerodynamic interaction between the rotor and fuselage. Several small-scale tests have been completed (refs. 6-8), and more are planned; full-scale tests will be conducted in the near future. For the baseline fuselage bodies, these investigations use axisymmetric shapes. Hence, although the present analytical investigation is restricted to axisymmetric shapes for the purpose of demonstrating its accuracy and limits, the method is directly applicable to the configurations of this experimental program. The two test modules routinely used for full-scale rotor tests in the Ames 40- by 80-Foot Wind Tunnel — the Rotor Test Apparatus (RTA) and the Easter Egg (EE) — provide body shapes for calculation of rotor performance and loads. Calculations can also be made with this body model to examine the ability to obtain isolated rotor behavior from measurements on these standard test modules.

This report presents the development of a modified slender body theory to calculate the flow field of an axisymmetric body at zero angle of attack. This analysis is coupled with a comprehensive helicopter analysis for calculation of the body-induced effects on the rotor performance and loads. The approach is verified by comparing the results for performance and loads from the modified slender body theory with results from an exact analysis for simple shapes. This comparison also provides a first look at the source of the rotor performance and load changes. Next, the body-induced effects on the rotor are calculated for several realistic cases: a typical full-scale rotor test configuration, configurations representing the model and full-scale aerodynamic interference tests at Ames, and a rotor-hybrid airship configuration. Finally, the efficiency of the modified slender body theory computations is discussed.

BACKGROUND OF ROTOR-BODY INTERACTION

Body-induced effects on the rotor have received somewhat less attention than rotor-induced effects on the body, although the entire topic of rotor-body aerodynamic interaction has been subject to intensive investigation only since the late 1970s. The following is a brief summary of some of the work dealing with body-induced effects on rotor behavior.

Reference 2 analyzes the effects of a model Lynx fuselage on rotor behavior. Calculations were made of the fuselage upwash effects on blade lift, torque, and bending moments. The change in blade angle of attack caused by the body, as well as the effects of rotor-body separation on upwash velocity, is presented. Body-induced effects on hub forces and moments are also shown. Reference 3 shows measurements of the effects of fuselage width and rotor-body separation on blade moments. A model fuselage and a fully articulated model rotor were used. Reference 4 presents calculations showing the effect of the fuselage on rotor blade angle of attack for two advance ratios. A sparse contour plot of the fuselage upwash velocity in the rotor plane is also shown. In addition, reference 4 provides a summary of some of the analytical work done in the rotor body interaction area.

Reference 6 presents experimentally the effects of a body of revolution on rotor performance. Advance ratio, tip-path-plane angle, body angle, rotor-body separation, and hub position are varied to cover a range of configurations. In reference 7, however, it was concluded that the data obtained in reference 6 were not accurate

enough for making conclusions about the influence of the body in rotor performance. Reference 8 is part of the interactional aerodynamics program being conducted at Ames, which includes references 6 and 7. Of particular interest to the present paper are the results shown in reference 8 for the surface pressure distribution of an isolated body of revolution.

Reference 9 shows the calculated upwash velocity contour in the rotor plane for a general fuselage model for several rotor-body separation distances. Also shown is the calculated influence of the fuselage on the local blade angle of attack and local blade lift for several rotor-body separation distances. Reference 10 shows the calculations for the fuselage upwash velocities in the rotor plane and the change in the blade angle of attack. Two analytical models were used in calculating the change in angle of attack owing to the body. The more refined model showed changes of smaller magnitude than the less complex model.

Reference 11 provides calculations of the effect of the fuselage on the edgewise bending moments for several flight conditions. The change in the local blade angle of attack caused by two body shapes (a helicopter fuselage and a wind tunnel test module) is shown. Reference 12 presents data from a model YUH-61A. The effects on blade bending moments and blade torsion resulting from variations in rotor-body separation and forward speed are presented. From the tabulated data presented in reference 13, the effect of two model fuselages on the rotor drag-to-thrust ratio can be found (effects shown in ref. 10).

Overall, there appears to be almost no performance measurements and no data for axisymmetric bodies when considering body-induced effects on the rotor. There has been little analysis of axisymmetric shapes (ref. 11) and little use of slender body theory with rotor calculations.

DEVELOPMENT OF THEORY

In developing an analytical model for the body flow field, the primary consideration was the computational efficiency of the method. The calculation of isolated rotor performance and loads is already a computationally expensive task. If the combined rotor-body analysis is to be predicted for routine use, it must require the same order of computer time as the isolated rotor problem. A number of panel methods have been developed for calculating the flow field of arbitrary bodies. These methods typically require several times the computer time of the rotor analysis; hence their usefulness is limited. A more efficient method is thus required. Considering the sources of the large computation time required for the panel codes, it is concluded that an efficient technique must use on the order of 100 singularities, and must obtain the singularity strength directly from the body shape (without inversion or iteration steps). Slender body theory, using small integration steps to evaluate the body-induced velocities, satisfies these requirements. For the cases considered here (axisymmetric bodies at zero angle of attack) it is possible to develop a surface singularity method that would be reasonably efficient. Unlike slender body theory, however, such a technique would not retain its efficiency when extended to the more general problem.

Slender Body Theory

The basis for the body model is slender body theory; potential flow is assumed. The body thickness is assumed to be much less than the body length. Since axisymmetric bodies are assumed, the potential and stream function of an axial source distribution are used (ref. 14):

$$\phi(x,r) = -\frac{1}{4\pi} \int_A^B \frac{q(\xi)d\xi}{[(x-\xi)^2 + r^2]^{1/2}}$$

$$\psi(x,r) = -\frac{1}{2} \int_A^B \frac{q(\xi)(x-\xi)d\xi}{[(x-\xi)^2 + r^2]^{1/2}}$$

The coordinate system and geometry used are shown in figure 1. Here, q represents the source distribution and A and B represent the endpoints of the body. The problem is to find a distribution q that will model the body. The following conditions must also be satisfied:

$$\frac{\partial\phi}{\partial n} = 0 \text{ (velocity normal to the body surface is zero)} \quad (1)$$

$$\int_A^B q(x)dx = 0 \text{ (net source strength is zero for a closed body)} \quad (2)$$

Applying conditions (1) and (2), in addition to assuming $r/x \ll 1$, the following result is obtained (see ref. 14) for details of derivation):

$$q(\xi) \cong U_0 A'(\xi) \quad (3)$$

Here, A is the cross-sectional area of the body. For a body of revolution, $A'(\xi) = 2\pi r_0(\xi)r_0'(\xi)$. Substituting for q in the expressions for ϕ and ψ yields:

$$\begin{aligned} \phi(x,r) &= U_0 \left\{ x - \frac{1}{2} \int_A^B \frac{r_0(\xi)r_0'(\xi)d\xi}{[(x-\xi)^2 + r^2]^{1/2}} \right\} \\ \psi(x,r) &= U_0 \pi \left\{ r^2 - \int_A^B \frac{r_0(\xi)r_0'(\xi)(x-\xi)d\xi}{[(x-\xi)^2 + r^2]^{1/2}} \right\} \end{aligned} \quad (5)$$

Note that the above two equations now include the free-stream velocity U_0 .

To obtain the axial and radial velocity components induced by the body, the Cauchy-Reimann relations are used, that is,

$$\frac{\partial\phi}{\partial x} = \frac{1}{2\pi r} \frac{\partial\psi}{\partial r} = U_x$$

$$\frac{\partial \phi}{\partial r} = -\frac{1}{2\pi r} \frac{\partial \psi}{\partial x} = U_r$$

Since the zero streamline, $\psi = 0$, defines the body surface, the stream function rather than the potential is used in subsequent equations and calculations. Applying the Cauchy-Riemann relations yields

$$U_x = U_o \left\{ 1 + \frac{1}{2} \int_A^B \frac{r_o(\xi)r_o'(\xi)(x - \xi)d\xi}{[(x - \xi)^2 + r^2]^{3/2}} \right\}$$

$$U_r = \frac{U_o}{2} \int_A^B \frac{r_o(\xi)r_o'(\xi)r d\xi}{[(x - \xi)^2 + r^2]^{3/2}}$$

Ideally, the stagnation points of the flow field are located at the nose and tail of the body. For bodies with blunt noses and tails, the stagnation points will be forward of the nose and aft of the tail, if the source distribution is allowed to run from the nose to the tail. The stagnation point is found by setting the equation for U_x equal to zero at $r = 0$ and solving the resulting equation for x by iteration. Figure 2(a) shows the amount of overshoot of the stagnation point versus the maximum thickness of several ellipses. To correct for this overshoot, the limits of integration were modified. For bodies with blunt ends, reference 15 shows that good approximations for the locations of the limits of integration are points that are halfway between the nose and the center of curvature of the nose, and halfway between the tail and the center of curvature of the tail.

Location of Integration Limits

The required offset for the limits of integration can be derived in the following way. Assume some offset ϵ at the nose. Physically, $U_x = 0$ at the actual body nose, that is, $U_x = 0$ at $(x,r) = (A - \epsilon, 0)$. So,

$$0 = 1 - \frac{1}{2} \int_A^B r_o(\xi)r_o'(\xi)(\xi - A + \epsilon)d\xi$$

First consider the case of a blunt or rounded nose. For this case, $r_o(A) = 0$ and $r_o'(A) = \infty$, but $r_o(A)r_o'(a)$ is finite. In fact, $r_o(A)r_o'(A) = RCN$, where RCN is the radius of curvature of the nose. This can be shown by examining the equation for a circle with radius of curvature RCN and tangent to the body nose:

$$RCN^2 = (x - RCN)^2 + r_o^2(x)$$

The derivative is

$$0 = 2(x - RCN) + 2r_o(x)r_o'(x)$$

So at $x = 0$,

$$RCN = r_o(0)r_o'(0)$$

Evaluating the above integral for a rounded nose gives

$$\begin{aligned}
 2 &= \int_A^B r_o(\xi) r_o'(\xi) (\xi - A + \epsilon)^{-2} d\xi \\
 &\cong r_o(A) r_o'(A) \int_A^B (\xi - A + \epsilon)^{-2} d\xi \\
 &= RCN \int_0^l (z + \epsilon)^{-2} dz \\
 &= RCN \left(\frac{1}{\epsilon} - \frac{1}{l + \epsilon} \right) \\
 &= \frac{RCN}{\epsilon}
 \end{aligned}$$

or $\epsilon = RCN/2$.

For a pointed nose, $r_o'(A) = S$ is finite (S is slope at nose). This gives,

$$\begin{aligned}
 2 &= \int_A^B r_o(\xi) r_o'(\xi) (\xi - A + \epsilon)^{-2} d\xi \\
 &\cong [r_o'(A)]^2 \int_A^B (\xi - A) (\xi - A + \epsilon)^{-2} d\xi \\
 &= S^2 \int_0^l z (z + \epsilon)^{-2} dz \\
 &= S^2 \ln(l + \epsilon) - \ln \epsilon - \frac{l}{l + \epsilon} \\
 &\cong -S^2 \ln \epsilon
 \end{aligned}$$

or

$$\epsilon = e^{-2/S^2}$$

So, for a pointed nose, ϵ is very small for a moderate slope.

Correction Factor K

For moderately thick bodies, slender body theory underpredicts the maximum thickness. Figure 2(b) shows the calculated maximum thickness for ellipsoids. For bodies that are symmetric fore and aft, that is, for ellipsoids, a factor of K is all that is needed to match the maximum thickness. As a result, for ellipsoids, the following expression for ψ was used:

$$\psi(x,r) = U_0 \pi \left(r^2 - \int_{AA}^{BB} \frac{K r_0(\xi) r_0'(\xi) (x - \xi) d\xi}{[(x - \xi)^2 + r^2]^{1/2}} \right)$$

where

$$AA = A + RCN/2$$

$$BB = B - RCT/2$$

For an ellipse, $RCN = RCT = t^2/a$, where t is the maximum thickness and a is the length of the semimajor axis (see fig. 1(b)). In this study, the semimajor axis will always be 1/2 and the body will span from 0 to 1. Now, a value of K is desired such that $r = t$ at $x = 1/2$. Setting the above equation for ψ equal to 0 and expressing the limits of integration in terms of $R = 2t^2$, the following equation for K is obtained:

$$K = \left\{ R \ln \left[\frac{-1 + R + (1 + R^2)^{1/2}}{1 - R + (1 + R^2)^{1/2}} \right] + (1 - R)(1 + R^2)^{1/2} \right\}^{-1}$$

An approximate form for $K(t)$ can be obtained by expanding the log term and square root term. This results in

$$K \cong [1 - R + R \ln(R/2) + (3/2)R^2 + O(R^3)]^{-1}$$

A plot of K versus t is shown in figure 3. Figure 4 shows the amount of overshoot of the stagnation point, using the modified slender body theory. Comparing figures 2(a) and 4, the modified theory shows a reduction in the overshoot.

Compressed Coordinate System

For the case of more general bodies that are not symmetric fore and aft, a compressed coordinate system was introduced to maintain net zero source strength. Now,

$$q(\xi) = \mathcal{K} q_{SB}(\xi^*)$$

where

$$\xi^* = \frac{\xi - RCN/2}{1 - RCA}$$

RCN = radius of curvature of nose

RCT = radius of curvature of tail

$$RCA = (1/2)(RCN + RCT)$$

Note:

$$\xi^* = 0 \quad \text{at} \quad \xi = \frac{RCN}{2}$$

$$\xi^* = 1 \quad \text{at} \quad \xi = 1 - \frac{RCT}{2}$$

$$0 \leq \xi^* \leq 1$$

and

$$q_{SB}(\xi^*) = U_o A'(\xi^*)$$

Applying this compressed coordinate system to an ellipsoid gives

$$\begin{aligned} q_{SB}(\xi^*) &= -\left(\xi - \frac{1}{2}\right)4t^2 \\ q(\xi) &= -\mathcal{K}\left(\xi^* - \frac{1}{2}\right)4t^2 \\ &= -\mathcal{K}\left(\frac{\xi - 1/2}{1 - RCA}\right)4t^2 \\ &= \frac{\mathcal{K}}{1 - RCA} q_{SB}(\xi) \\ &= Kq_{SB}(\xi) \end{aligned}$$

In the above equation, K is that value calculated previously for an ellipsoid. For a more general shape, then,

$$q(\xi) = \mathcal{K}q_{SB}(\xi^*) = K(1 - RCA)q_{SB}(\xi^*)$$

For these general shapes, K can be calculated based on an ellipsoid with $R = RCA$. Alternatively, \mathcal{K} can be evaluated directly from the requirement that the maximum thickness of the body be matched. The following expression for ψ was thus used:

$$\psi(x, r) = U_o \pi \left\{ r^2 - \int_{AA}^{BB} \frac{K(1 - RCA)q(\xi^*)(x - \xi)d\xi}{[(x - \xi)^2 + r^2]^{1/2}} \right\}$$

Numerical Integration of Equations

A computer program was written to integrate numerically the equations for the stream function and velocities using Simpson's rule. For example, if a body streamline is desired, the equation for ψ is set equal to zero; then for each value of x , a value of r is found by means of an interval-halving scheme such that $\psi = 0$. The body shapes are kept in separate subroutines so that different shapes may be used with relative ease. One hundred integration steps ($N = 100$) was found to be sufficient in most cases for integrating ψ (or the velocities). For locating stagnation points, $N > 100$ was sometimes needed. For body shapes requiring a compressed coordinate system, ξ was transformed to ξ^* before entering the body-shape subroutines. A flowchart of the procedure is shown in figure 5. The subroutine VEL which computes the velocity components, is similar to the subroutine STREAM, except that the equations for U_x and U_r are integrated instead of ψ .

Source Strength Distribution for a Pointed Tail

Results obtained for the zero streamline using the above expression for ψ show that the nose is well modeled, but a pointed tail is not. Regular slender body theory, however, models the tail shape quite well, but breaks down near the nose. Multiplying the source strength by a factor of $K(1 - RCA)$ alone for a body with a pointed tail increases the predicted body slope. An additional condition was therefore needed to improve the mathematical model; that is, the derivative of the singularity strength at a pointed nose or tail was maintained in order to match the body slope. A new formulation for q was thus developed for the pointed-tail case.

Tail Correction Procedure

The following equation for the source distribution,

$$q(\xi) = Kq_{SB}(\xi^*)$$

models the nose of the body well. But using this distribution gives for the tail

$$q'(1) = K\xi^{*'} q'_{SB}(1)$$

Since slender-body theory models the tail region well, the desired form of q at the tail is

$$q'(1) = q'_{SB}(1)$$

Thus, let q take on the following form:

$$q(\xi) = KNq_{SB}(\xi^*) + f(\xi^*)(\xi^* - 1)(1 - KN\xi^{*'})q'_{SB}(1)$$

where

$$q_{SB}(\xi^*) = 2\pi U_o r_o(\xi^*) r_o'(\xi^*)$$

$$q'_{SB}(1) = 2\pi U_o [r_o'(1)]^2$$

and KN is a factor such that $r = t$ at the point of maximum thickness. Note that $q'(1) = q'_{SB}(1)$ if $f(1) = 1/\xi^{*'}$, which is the desired result. For a closed body,

$$\int_0^1 q(\xi) d\xi = 0$$

which gives

$$\int_0^1 f(\xi^*)(\xi^* - 1) d\xi^* = 0$$

In addition, the condition of $f(0) = 0$ must also be met to maintain the source distribution at the nose.

In summary, f must satisfy the following three requirements:

1. $f(0) = 0$

2. $f(1) = 1/\xi^{*1}$

3. $\int_0^1 f(\xi^*) (\xi^* - 1) d\xi^* = 0$

In addition to the above requirements, it was desired that f be a continuous function to prevent difficulties in the numerical integration scheme. Therefore, f was chosen to be piecewise linear for simplicity. Knowing the desired form of f , the following distribution of f was chosen:

$$f(\xi^*) = \begin{cases} \frac{-a_0 \xi^*}{\xi_1 \xi^{*1}} & \text{for } 0 \leq \xi^* \leq \xi_1 \\ \frac{-a_0 (\xi_2 - \xi^*) + (\xi^* - \xi_1)}{(\xi_2 - \xi_1) \xi^{*1}} & \text{for } \xi_1 < \xi^* \leq \xi_2 \\ \frac{1}{\xi^{*1}} & \text{for } \xi_2 < \xi^* \leq 1 \end{cases}$$

A sketch of f versus ξ^* is shown in figure 6. As shown there, there are three parameters to be determined: a_0 , ξ_1 , and ξ_2 . By applying condition 3 from above, a_0 is chosen to be

$$a_0 = \frac{3(\xi_1 + \xi_2 - 1) - (\xi_2^2 + \xi_1^2 + \xi_1 \xi_2)}{\xi_2 (\xi_1 + \xi_2 - 3)}$$

For a given body shape, ξ_1 and ξ_2 are determined by trial and error. Given ξ_1 and ξ_2 , the value of KN can be found by numerically integrating (also using Simpson's rule) the following expression:

$$KN = \frac{t^2 - \int_{AA}^{BB} \frac{f(\xi^*) (\xi^* - 1) (x_0 - \xi) q'_{SB}(1) d\xi}{[(x_0 - \xi)^2 + t^2]^{1/2}}}{\int_{AA}^{BB} \frac{[q_{SB}(\xi^*) (x_0 - \xi) - f(\xi^*) (\xi^* - 1) (x_0 - \xi) q'_{SB}(1) \xi^{*1}] d\xi}{[(x_0 - \xi)^2 + t^2]^{1/2}}}$$

Here, x_0 is the x -coordinate of the point of maximum thickness.

The tail correction procedure may be difficult to generalize to other body shapes, especially those with abrupt changes in body slopes. Several attempts were necessary to choose the ξ_1 and ξ_2 values for the cases in this report.

Treatment of Test Module Shapes

The EE and the RTA test modules have blunt ends; however, the radii of curvature of the tails are very small relative to the body lengths (see table 1). To apply the modified slender body theory with tail correction, the tails of the EE and RTA were extended to a point. The extension increased the length of the EE by about 7.7%; the RTA length increased by 9.9%. In the analysis thus far, all body lengths were normalized to one, as was the free-stream velocity. Because the extensions caused the lengths of the EE and RTA to be greater than one, a "stretching" of the coordinate system for these two cases was necessary. A brief explanation of this procedure follows.

Before entering the body shape subroutine, the coordinates are compressed, as discussed earlier. The amount by which the EE (or RTA) is extended is computed in the body shape subroutine. Before it is entered into the equations that describe the body shape, the variable ξ^* is multiplied by the amount of the extension, XE. For example, XE for the EE is 1.077308; for the RTA, XE = 1.098950. Also, $r_0(\xi^*XE)$ is multiplied by $1/XE$. The body slope must remain the same as the physical body, so $r'_0(\xi^*XE)$ is not multiplied by $1/XE$. The body streamline generated by this procedure has a range of $0 \leq x \leq 1$ and has a maximum thickness of t/XE , where t is the maximum thickness as defined earlier for the actual EE (or RTA) with unextended tail. A diagram of the procedure is shown in figure 5(c). Note that $2\pi U_0 r_0 r'_0$ and $2\pi U_0 [r'_0(1)]^2$ are equivalent to q_{SB} and $q'_{SB}(1)$, respectively.

Body Shapes

Table 1 gives the equations for the actual body shapes used in this study. Table 2 gives the values of ξ_1 , ξ_2 , a_0 , and KN, which produced body streamlines that closely matched the actual body shapes.

Exact Solutions

Exact solutions describing the flow about a sphere or an ellipsoid can be found in the fluid mechanics literature. For a sphere, the potential and stream function are given by (see ref. 16)

$$\phi(x,r) = U_0 x \left[1 - \frac{a^3}{2(x^2 + r^2)^{3/2}} \right]$$

$$\psi(x,r) = U_0 \pi r^2 \left[1 + \frac{a^3}{(x^2 + r^2)^{3/2}} \right]$$

where a is the radius of a sphere centered at $(x,r) = (0,0)$. This gives for the velocities

$$U_x = U_0 - \frac{U_0 a^3}{(x^2 + r^2)^{3/2}} \left[1 - \frac{3}{2} \left(\frac{r^2}{x^2 + r^2} \right) \right]$$

$$U_y = \frac{3a^3}{2} \frac{xy}{(x^2 + r^2)^{5/2}}$$

$$U_z = \frac{3a^3}{2} \frac{xz}{(x^2 + r^2)^{5/2}}$$

For a coordinate system centered at the body nose, x should be replaced by $(x - a)$. For a sphere of unit length, $a = 1/2$.

For flow about an ellipsoid, the potential is given in elliptic coordinates by the following expression (see ref. 16):

$$\phi(\mu, \nu, \omega) = U_o k \mu \nu + A \mu \left[\frac{1}{2} \nu \ln \left(\frac{\nu + 1}{\nu - 1} \right) - 1 \right]$$

where (for $\nu > 1$)

$$x = f(\mu, \nu, \omega) = k \mu \nu$$

$$y = g(\mu, \nu, \omega) = k \cos \omega (1 - \mu^2)^{1/2} (\nu^2 - 1)^{1/2}$$

$$z = h(\mu, \nu, \omega) = k \sin \omega (1 - \mu^2)^{1/2} (\nu^2 - 1)^{1/2}$$

$$\tan \omega = z/y$$

$$k = (a^2 - b^2)^{1/2}$$

$$A = \frac{U_o a}{\frac{1}{1 - e^2} - \frac{1}{2e} \ln \left(\frac{1 + e}{1 - e} \right)}$$

$$e \triangleq \text{eccentricity} = \frac{(a^2 - b^2)^{1/2}}{a}$$

$$a \triangleq \text{semimajor axis}$$

$$b \triangleq \text{semiminor axis}$$

To obtain the velocity components, the following relations are used:

$$U_x = \frac{\partial \phi}{\partial \mu} \frac{\partial \mu}{\partial x} + \frac{\partial \phi}{\partial \nu} \frac{\partial \nu}{\partial x}$$

$$U_y = \frac{\partial \phi}{\partial \mu} \frac{\partial \mu}{\partial y} + \frac{\partial \phi}{\partial \nu} \frac{\partial \nu}{\partial y}$$

$$U_z = \frac{\partial \phi}{\partial \mu} \frac{\partial \mu}{\partial z} + \frac{\partial \phi}{\partial \nu} \frac{\partial \nu}{\partial z}$$

Note: $\partial \phi / \partial \omega = 0$. From the expression for $\phi(\mu, \nu)$, one obtains

$$\frac{\partial \phi}{\partial \mu} = U_o \nu k + A \left[\frac{1}{2} \nu \ln \left(\frac{\nu + 1}{\nu - 1} \right) - 1 \right]$$

$$\frac{\partial \phi}{\partial \nu} = U_o \mu k + A \mu \left[\frac{1}{2} \ln \left(\frac{\nu + 1}{\nu - 1} \right) - \frac{\nu}{\nu^2 - 1} \right]$$

In order to find the partial derivatives with respect to the Cartesian coordinates, the following matrix inversion is necessary:

$$\begin{bmatrix} \frac{\partial \mu}{\partial x} & \frac{\partial \mu}{\partial y} & \frac{\partial \mu}{\partial z} \\ \frac{\partial v}{\partial x} & \frac{\partial v}{\partial y} & \frac{\partial v}{\partial z} \\ \frac{\partial \omega}{\partial x} & \frac{\partial \omega}{\partial y} & \frac{\partial \omega}{\partial z} \end{bmatrix} = \begin{bmatrix} \frac{\partial f}{\partial \mu} & \frac{\partial f}{\partial v} & \frac{\partial f}{\partial \omega} \\ \frac{\partial g}{\partial \mu} & \frac{\partial g}{\partial v} & \frac{\partial g}{\partial \omega} \\ \frac{\partial h}{\partial \mu} & \frac{\partial h}{\partial v} & \frac{\partial h}{\partial \omega} \end{bmatrix}^{-1}$$

Inverting the matrix results in

$$\begin{aligned} \frac{\partial \mu}{\partial x} &= \frac{v}{k} \frac{(1 - \mu^2)}{(v^2 - \mu^2)} & \frac{\partial \mu}{\partial y} &= \frac{-\mu \cos \omega (1 - \mu^2)^{1/2} (v^2 - 1)^{1/2}}{k(v^2 - \mu^2)} & \frac{\partial \mu}{\partial z} &= \frac{-\mu \sin \omega (1 - \mu^2)^{1/2} (v^2 - 1)^{1/2}}{k(v^2 - \mu^2)} \\ \frac{\partial v}{\partial x} &= \frac{\mu(v^2 - 1)}{k(v^2 - \mu^2)} & \frac{\partial v}{\partial y} &= \frac{v \cos \omega (1 - \mu^2)^{1/2} (v^2 - 1)^{1/2}}{k(v^2 - \mu^2)} & \frac{\partial v}{\partial z} &= \frac{v \sin \omega (1 - \mu^2)^{1/2} (v^2 - 1)^{1/2}}{k(v^2 - \mu^2)} \\ \frac{\partial \omega}{\partial x} &= 0 & \frac{\partial \omega}{\partial y} &= \frac{-\sin \omega}{k(1 - \mu^2)^{1/2} (v^2 - 1)^{1/2}} & \frac{\partial \omega}{\partial z} &= \frac{\cos \omega}{k(1 - \mu^2)^{1/2} (v^2 - 1)^{1/2}} \end{aligned}$$

Hence, the velocity components are given by

$$\begin{aligned} U_x &= U_0 + \frac{A}{k} \left[\frac{1}{2} \ln \left(\frac{v+1}{v-1} \right) - \frac{v}{v^2-1} \right] \\ U_y &= \frac{-A\mu \cos \omega (1 - \mu^2)^{1/2}}{k(v^2 - \mu^2)(v^2 - 1)^{1/2}} \\ U_z &= \frac{-A\mu \sin \omega (1 - \mu^2)^{1/2}}{k(v^2 - \mu^2)(v^2 - 1)^{1/2}} \end{aligned}$$

Given (x,y,z), v can be found, which then gives μ, as follows

$$\begin{aligned} y^2 + z^2 &= k^2 (1 - \mu^2) (v^2 - 1) \\ &= k^2 (v^2 + \mu^2 - \mu^2 v^2 - 1) \\ &= k^2 v^2 + x^2/v^2 - x^2 - k^2 \end{aligned}$$

or

$$0 = v^4 - v^2 \left(\frac{x^2 + y^2 + z^2 + k^2}{k^2} \right) + \left(\frac{x}{k} \right)^2$$

The above quadratic equation results in four roots. Since v must be greater than 1, three of the roots are eliminated and so:

$$v = \left\{ \frac{x^2 + y^2 + z^2 + k^2}{2k^2} + \frac{\left[\frac{(x^2 + y^2 + z^2 + k^2)^2}{k^2} - 4\left(\frac{x}{k}\right)^2 \right]^{1/2}}{2} \right\}^{1/2}$$

The value of k is determined by the maximum thickness of the ellipse ($b = t$); the value of the semimajor axis will always be $l/2$.

Incorporation of Body-Induced Velocities into a Comprehensive Rotor Analysis

After the various body models were developed to a satisfactory degree, the next step was to introduce the body-induced velocities into the comprehensive helicopter analysis CAMRAD (ref. 17). The solution procedure for the rotor behavior is basically unchanged, since no iteration between the body and rotor is involved (except to update the body-induced velocities when the rotor position relative to the body changes as the trim iteration proceeds). The cases considered in this report involve a single rotor, and a body at zero angle of attack. Hence, the wind-tunnel configuration of reference 17 can be used, with zero pitch and yaw angles of the body axes. The axis systems used are shown in figure 7. The calculation of the body-induced velocities is performed for each location on the rotor disk. The blade position on the rotor disk (scaled with the body length) relative to the body nose is (see fig. 7):

$$\bar{r} = (-\bar{r}_B + \bar{r}_R + R_{SF}^T \bar{r}_b) \frac{R}{l}$$

where

l/R = body length/rotor radius

\bar{r}_B = position of the body origin relative to the body c.g. (body axes)

\bar{r}_R = position of the rotor hub relative to the body c.g. (body axes)

\bar{r}_b = blade position relative to the hub location (shaft axes)

R_{SF} = matrix which transforms body-axis system (origin at c.g.) to shaft-axis system (origin at hub position); defined by shaft pitch angle θ_r and cant angle ϕ_r

The calculation of \bar{r}_b is defined in reference 17 (p. 143). The blade position \bar{r} is sent to a subroutine that calculates the body-induced velocities. The velocities are then included as perturbations in the rotor section velocity components. Since CAMRAD computes the rotor section velocities relative to the shaft axes, it is necessary to transform the body-induced velocities to the shaft axes system. Hence,

$$\bar{\lambda} = R_{SF} \bar{V} \begin{pmatrix} U \\ \Omega R \end{pmatrix}$$

where

$\bar{V} = (V_x, V_y, V_z)$ = body-induced velocity relative to body axes, scaled by free-stream velocity

ΩR = rotor tip speed

$\bar{\lambda}$ = induced velocity at rotor disk relative to shaft axes

The location on the rotor disk at which the body-induced velocities are calculated depends on the blade motion; therefore, ideally the induced velocities should be calculated at least once per circulation iteration within CAMRAD. However, this resulted in a large number of induced velocity calculations which were found to be unnecessary in achieving convergence. Calculation of the induced velocities once per control iteration was found to be more than sufficient, since the rotor position changes little during the final stages of the trim iteration, as shown in figure 8, for a representative forward flight analysis. Options to compute the velocities at other locations in CAMRAD are possible.

Figures 9(a) and 9(b) show the entry points of the body-induced velocity subroutine into CAMRAD. To assess the influence of the various body shapes discussed thus far, eight options were programmed. These eight options and the necessary inputs required by CAMRAD are shown in figure 9(c). A list of the subroutines in CAMRAD, which were modified, and a list of new subroutines, which were added, are shown in figure 9(d). A skeleton of the subroutine BODYI is shown in figure 9(e). Complete details of the CAMRAD program structure and input are given in reference 18.

For the case of OPSHAP = -1 or -2, an unformatted file of velocities is read; no calculations of body-induced velocities are made. The velocity file is generated by a panel code or by some other means independent of CAMRAD. The disadvantage of this method for accounting for body-induced effects is that the velocities cannot be updated if the rotor blade position relative to the body changes during the analysis. The file has the logical name VELOCITYFILE, and will be read by a statement of the form

```
READ(NFILE) (((VINT(K,I,J),K = 1,3),I = 1,MRA),J = 1,MPSI)
```

where K is the index for the three velocity components, I is the index for the blade radial station, and J is the index for the blade azimuth position. The velocity should be calculated at the midpoints of the blade aerodynamic panels defined by the parameter RAE in namelist NLRTR (see ref. 18); the total number of stations, MRA, is also from namelist NLRTR. The azimuth positions are $\psi = 360 * J/MPSI$ (deg), where the total number MPSI is from namelist NLTRIM. For OPSHAP = -1, a velocity file of $\bar{V}(r,\psi)$ relative to the (X_F, Y_F, Z_F) coordinate system is read (see fig. 7). The velocities are scaled by the free-stream velocity. These velocities will be transformed to $\bar{\lambda}$ as described above. For OPSHAP = -2, a velocity file of $\bar{\lambda}(r,\psi)$ relative to the (X_S, Y_S, Z_S) coordinate system is read. In this case, the velocities are scaled by the tip speed ΩR .

ANALYTICAL MODEL OF ROTOR

Three types of rotors (table 3) were used in the present study. Nonuniform inflow and a free wake geometry (for two or three revolutions of the wake) were used to model the rotor environment. Results obtained from use of a prescribed wake geometry showed no significant change from the free wake results. Aerodynamic calculations were performed at 15 radial stations along the blade and at every 15° of azimuth. The radial stations along the blade become more concentrated near the blade tip. For rotor A, a teetering flap mode with one harmonic of motion was used. For

rotors B and C, six flap/lag bending modes (including the rigid body modes) and one (blade) pitch mode were used; seven harmonics of motion were used for each mode. Rotor A is a stiff model rotor, for which only the performance was calculated. Both rotor performance and loads were calculated for rotors B and C.

All the calculations were performed for sea level standard conditions. The rotor tip Mach number was held constant (see table 3), and the advance ratio was in the range $\mu = 0.15$ to 0.50 , depending on the case considered (see table 4). The rotor thrust and the tip-path-plane tilt relative to the rotor shaft were trimmed to specified values by varying the rotor collective pitch and cyclic pitch control angles. The thrust was varied from $C_T/\sigma = 0.05$ to 0.09 , typically, and the lateral flapping angle was always trimmed to zero. The longitudinal flapping angle (and hence the tip-path-plane angle) were trimmed to values depending on the case considered (see table 4).

The body velocities were recalculated after each control change during the rotor trim iteration, ensuring that the velocities were evaluated at the correct, that is, at the final trimmed rotor position.

The adequacy of the rotor model can be assessed by comparing the theory with experimental rotor data. Figure 10 shows the L/D as a function of thrust for rotor A over a range of advance ratios. The data were obtained from reference 6. The correlation is good, although the experimental data were not accurate enough to show a trend with tip-path-plane angle (for a fixed advance ratio). Figure 11 shows L/D versus advance ratio for two values of C_T/σ for rotor B. Figure 12 shows the one-half peak-to-peak blade loads for rotor B. Figures 12(b) and 12(c) were calculated at the 70% and 60% blade radial station, respectively. The data were obtained from reference 19. Both the data and the theory for figures 11 and 12 include the effects of the RTA, but as will be shown later in the paper, the RTA has a very small effect on the rotor behavior. The correlation is good to fair; similar correlation is shown in reference 11.

No data are available yet for the isolated behavior of rotor C.

Nonuniform Inflow

The changes in blade loads and profile power are due to changes in the complex flow field of the rotor blade. The perturbation velocities are fixed by the body. These velocities do not simply produce an incremental change in the blade loads and power. Because of the nonlinear relationship between the perturbation velocities and the blade loads and the profile power, proper calculation of the blade angle of attack distribution is necessary. Changes in the induced power caused by the body would be zero if a uniform inflow model (momentum theory with empirical corrections) was used. Even the direct interference power requires a detailed thrust distribution over the rotor disk. Hence, a nonuniform inflow model is necessary to assess body-induced effects on rotor behavior.

Wake Geometry

As stated earlier, a free wake geometry was used for all calculations presented in this paper. Comparisons were made with prescribed wake results, and no significant changes were found in performance or loads caused by the wake distortion. It follows that body-induced wake geometry variations would not be important either. Therefore,

the absence of the distortion of the wake geometry by the body in the present analysis is not significant. The change in the body flow field due to the rotor, which then changes the perturbation velocities at the rotor, is also neglected.

Trimming (Convergence of Solution)

Results presented here are for a fixed tip-path-plane angle, α_{TPP} . An alternate approach would be to trim to a specified propulsive force. The presence of the body does change the propulsive force for a fixed α_{TPP} ; therefore, slightly different results are obtained for trimming to propulsive force rather than trimming to α_{TPP} . These differences were not found to be significant for the cases presented here, which are for small propulsive force.

RESULTS: VERIFICATION OF APPROACH

The accuracy of the modified slender body theory will be examined for case 1 of table 4: ellipsoids and axisymmetric bodies with a NACA four-digit airfoil thickness distribution. The ellipsoid case is useful because the exact solution for the body-induced velocities is known. The airfoil shapes are a reasonable approximation for typical wind tunnel test modules. The complete modified slender body theory with tail correction will serve as the "exact" solution for the airfoil shaped bodies. Since the purpose is to establish the limits of the method, high values of the body thickness (up to $t = 0.50$) are used.

Ellipsoids

The validity of the models developed using slender body theory can be determined by first considering the flow field of ellipsoids, for which the exact solution is available.

Figure 13 shows the dividing streamline (body shape) of ellipsoids, as obtained by unmodified and modified slender body theory. Compared with the exact body shape, the modified theory shows good accuracy for the 60%-thick body, and fair accuracy for the 80%-thick body. The 100%-thick body is even less accurate, but the modified theory always matches the maximum thickness.

Figures 14 and 15 show the flow field (velocity magnitude and angle of attack, respectively) about a 60%-thick ellipsoid in a plane above the body. Figures 16 and 17 and figures 18 and 19 show the flow field about 80%- and 100%-thick ellipsoids, respectively. The body-plane separation for all three bodies is 10% of the body length. Relative to the exact solution, slender body theory shows significant errors for all three bodies. The modified theory predicts both the velocity magnitude and angle of attack well, even though the body shape was not matched exactly (fig. 13). Note that for the 60%-thick body, the modified theory gives results that are nearly identical to those of the exact solution.

Figures 20-25 show the section angle of attack change induced by the body on a rotor blade for 60%-, 80%-, and 100%-thick ellipsoids. The rotor radius is equal to the body length, and the rotor-body separation is equal to 10% of the body length. The advance ratio is 0.4. The rotor hub is located above the body center in figures 20, 22, and 24; it is located above the body quarter chord in figures 21, 23,

and 25. Again, the modified slender body theory results are almost identical to those of the exact solution for 60%- and 80%-thick bodies. The modified theory results for the 100%-thick body show fair agreement with the exact solution. The body-induced changes in the velocity magnitude seen by the rotor are not significant, as shown by figure 26 (note that fig. 26(d) is for the isolated rotor). Here, the body is 80%-thick, the advance ratio is 0.4, and the rotor hub is located above the body center. The parameters for figures 27 and 28 are the same as in figures 22 and 23 except that the advance ratio is 0.2. At the lower advance ratio, the modified slender body theory results are also quite accurate.

Airfoil Shaped Bodies

The applicability of the theoretical method will be examined by comparing the predicted and actual dividing streamlines for more general (and more useful) body shapes than the ellipsoids. Typical results are as follows. Figure 29 shows axisymmetric bodies with a NACA four-digit airfoil thickness distribution. The 10%-thick body is well modeled by slender body theory except for the nose stagnation point location, which is correctly placed by using the modified theory. For the 30%- and 50%-thick bodies, results are shown from the modified theory with and without the tail correction. It is seen that the full, modified slender body theory gives good results.

The angle of attack change at the rotor blade is shown in figure 30 for a 30%-thick airfoil. The advance ratio is 0.4, the body length is equal to the rotor radius, and the rotor-body separation is again equal to 10% of the body length. The rotor is located above the body maximum thickness point for the symmetrical airfoil; this point is located at the body 0.3-chord station. Aft of the hub position, the full modified theory is actually closer to slender body theory than it is to the modified theory without the tail correction (because slender body theory models the shape of the tail correctly). Forward of the hub position, the modified theory without the tail correction and slender body theory solutions are quite similar.

Error in Performance and Loads

After satisfactory modeling of the ellipsoids and airfoils had been achieved, the next step was to determine the difference in rotor performance and loads as calculated using modified slender body theory and the exact solution (for airfoil shapes, modified slender body theory with tail correction results served as the "exact" solution). All values in this paper for edgewise and flapwise bending moments are one-half peak-to-peak values taken from steady-state time histories.

Figures 31(a) and 31(b) show, as a function of thrust, the error in the calculated lateral cyclic control angle and the rotor lift-to-drag ratio, respectively, caused by ellipsoids of various thicknesses. Rotor A was used for these calculations; other parameters are given in table 4, case 1. The errors are given by

$$\Delta(\theta_{1c}) = (\theta_{1c}) - (\theta_{1c})_{\text{exact body}}$$

$$\Delta(L/D) = (L/D) - (L/D)_{\text{exact body}}$$

Clearly, slender body theory shows significant errors, except for thin ellipsoids. The modified slender body theory results are good for moderately thick bodies. Figure 32 shows similar results for airfoil shaped bodies. The errors are given by

$$\Delta(\theta_{1c}) = (\theta_{1c}) - (\theta_{1c})_{\text{MSBT with tail correction}}$$

$$\Delta(L/D) = (L/D) - (L/D)_{\text{MSBT with tail correction}}$$

Figures 33(a) and 33(b) are plots of the errors in the oscillatory edgewise and flapwise bending moments, respectively, as a function of thrust for various ellipsoids. The moments were calculated at the 60% radial station. Rotor B was used for these calculations together with the values given in case 1 of table 4. The errors were calculated using the same procedure for calculating the performance parameters that was used above and are plotted as a fraction of the oscillatory loads for the exact body solution. Even for large thickness ratios, modified slender body theory shows very little error compared with the exact solution for both edgewise and flapwise bending moments. Slender body theory, however, shows large errors for both cases. Figure 34 shows similar results for the edgewise bending moment for various airfoil shapes. The flapwise bending moment showed little effect of the body, so no error calculations are presented. For a 50%-thick airfoil, modified slender body theory shows an improvement over slender body theory. Without the tail correction, there is an error of about 7.5% for the edgewise bending loads. For the 10%- and 30%-thick airfoils, slender body theory gives errors that are less than 5%.

Influence of Body on Rotor

The effects of various bodies on rotor performance and loads were next analyzed. Ideal body shapes are considered here since the results provide insight into the mechanisms involved in the body-induced changes of rotor performance and loads. Figures 35(a) and 35(b) show the changes in lateral cyclic control and lift-to-drag ratio, respectively, caused by various body shapes. Rotor A was used together with the parameters in case 1 of table 4. The ellipsoid results were calculated using the exact solution; the airfoil shaped body results were calculated using the modified slender body theory with tail correction. Figure 35(a) shows that for a given body shape, there is relatively no change in $\Delta\theta_{1c}$ with rotor thrust.

The body produces a basic once-per-revolution variation of the vertical interference velocity seen by the rotor blade, with maximum amplitude at azimuth angles $\psi = 0^\circ$ and 180° . Hence a lateral cyclic pitch change is needed to maintain the tip-path-plane lateral inclination at zero. Figure 35(b) shows the decrease in L/D caused by the body. Figure 36 shows the lift-to-drag ratio of rotor A caused by various body shapes. The performance loss increases in magnitude as the body thickness increases. The loss is significant only for large thickness ratios.

Rotor B, together with the parameters of case 1, was used to generate the results shown in figures 37 and 38. Figure 37 shows the changes in lift-to-drag ratio, oscillatory edgewise bending load, and oscillatory flapwise bending load for various ellipsoids and airfoil shapes. Unlike rotor A, rotor B shows an increase in performance up to about $C_T/\sigma = 0.075$ (compare figs. 37(a) and 35(b)). In figure 37, the blade oscillatory bending moments are plotted as a fraction of the isolated rotor loads. The bending loads increase for all body shapes over the given range of thrust. Figure 38 shows the edgewise and flapwise oscillatory loads as a function of thrust.

Pitch link loads were also calculated, but no significant influence of the body was found (5%-10% change for the ellipsoids, 3%-5% change for the airfoil shapes). Also, there was little difference in the pitch link loads predicted using the various body theories compared above.

Source of Performance Loss Caused by Body

To determine the cause of the performance change produced by the body, a detailed analysis of the effect of an 80%-thick ellipsoid on rotors A and B was performed.

Table 5 shows the breakdown of C_p/σ (power coefficient divided by solidity) for rotor A as affected by an 80%-thick ellipsoid. The rotor thrust was $C_T/\sigma = 0.08$ (case 1). From table 5, it follows that there is a small increase in the performance directly caused by the interference velocity. The loss caused by the profile power and induced power is larger, however, than the gain caused by the interference power. Thus, the lift-to-drag ratio decreases. Note that the same behavior is shown for both tip-path-plane angle trim and propulsive force trim.

Polar plots were generated for λ_{int} (interference inflow ratio = $V_{int}/\Omega R$), α (blade section angle of attack), c_d (drag coefficient), C_{p_0} (profile power coefficient), c_l (lift coefficient), C_T (thrust coefficient), C_{p_i} (induced power coefficient), and $C_{p_{int}}$ (interference power coefficient) to determine how each parameter varied over the rotor disk. A brief summary of the plots is discussed below.

The vertical interference velocity λ_{int} was found to be negative (up) on the front of the disk, and positive (down) on the rear of the disk. Hence, λ_{int} was roughly proportional to $\cos \psi$ (a 1/rev variation with for/aft symmetry). Lateral cyclic, $\Delta\theta_{1c}$, is needed to cancel the resulting change in flap moment, ΔM_F , resulting from this 1/rev variation. The lateral cyclic control angle, $\Delta\theta_{1c}$, and λ_{int} are both proportional to $\cos \psi$, but θ is independent of r and λ is larger near the hub. Roughly, $\lambda_{int} = (\lambda_t/r^2)\cos \psi$, where λ_t is the value of λ at the tip. The flap moment is given by

$$\Delta M_F \sim r^2 (r\theta - \lambda_{int}) = (r^3 \Delta\theta_{1c} - \lambda_t) \cos \psi$$

It follows that the total blade flap moment change, which must be zero for an articulated rotor, is

$$\int_0^1 \Delta M_F dr = 0 = \int_0^1 (r^3 \Delta\theta_{1c} - \lambda_t) \cos \psi dr = \left(\frac{\Delta\theta_{1c}}{4} - \lambda_t \right) \cos \psi$$

or

$$\Delta\theta_{1c} = 4\lambda_t$$

Now, the change in angle of attack can be expressed as

$$\Delta\alpha = \theta - \frac{\lambda_{int}}{r} = \lambda_t \cos \psi \left(4 - \frac{1}{r^3} \right)$$

Thus, we expect that $\Delta\alpha = 0$ at $r = 4^{-1/3} = 0.63$. Results show $\Delta\alpha$ to be zero at approximately $r = 0.75$.

In general, α was found to increase inboard and decrease outboard on the front of the disk. On the rear of the rotor disk, α decreased inboard and increased outboard. Figure 39 shows the angle of attack change caused by the body over the rotor disk for this case. This angle of attack change produces a change in the blade section drag coefficient, but the pattern is different because c_d is a nonlinear function of α . The drag coefficient c_d was found to increase inboard of the region of $\psi = 180^\circ$. On the advancing side, however, c_d increased outboard. The change in α caused by the body on the retreating side of the disk shifts the stall region by a small amount. The lower values of α on the rear of the disk reduce the drag somewhat. Although α is negative in the tip region in the second quadrant of the rotor disk, the magnitude is such that the c_d is increased on most of the advancing side in the tip region. The profile power coefficient C_{p0} was found to vary similarly to c_d .

The rotor-blade lift coefficient c_l and the thrust coefficient C_T were found to vary similarly to α . The maximum circulation (which determines the wake-induced velocities) is found to be greater at both $\psi = 0^\circ$ and at $\psi = 180^\circ$ at constant C_T/σ , so the radial distribution of the circulation is being changed. The induced velocity was somewhat higher on the front and back of the disk when the body was included.

The induced power coefficient C_{pi} was found to vary similarly to C_T . There is a small net increase in C_{pi} since λ_i generally increases from the front to the back of the rotor disk. The interference power coefficient C_{pint} varies similarly to λ_{int} . The rotor thrust coefficient C_T is higher on the front of the disk (partly because of body effects), so the power increase from the front of the disk is greater than the power loss from the rear of the disk.

Table 6 shows the breakdown of C_p/σ for rotor B as affected by an 80%-thick ellipsoid (case 1). The same basic behavior in rotor A is also observed in rotor B. A high value of C_T/σ is needed, however, in order for the sum of the increases in induced and profile power to be greater than the interference power (note that $C_T/\sigma = 0.08$ for table 5).

Source of Bending Load Increase Caused by the Body

To analyze the body effects on the rotor loads, rotor B was used in combination with an 80%-thick ellipsoid. Figures 40(a) and 40(b) show the time histories of the edgewise and flapwise bending loads, respectively. Figure 40 was generated under the conditions of case 1, with $C_T/\sigma = 0.08$ (see also table 6). The bending moments were calculated at the 60% radial station. Figure 40 shows that the effect of the body is mainly on the front of the disk from $\psi = 90^\circ$ to $\psi = 270^\circ$. Referring to figures 37(b) and 37(c), the increase in the edgewise and flapwise bending moments caused by the body is 74% and 26%, respectively, for an 80% ellipsoid at $C_T/\sigma = 0.08$. The change in the edgewise bending moment is positive on the front of the disk, corresponding to a lead motion. The change in the flapwise bending moment is negative in this region, corresponding to a downward flapping motion. As stated earlier, α was found to increase inboard and decrease outboard on the front of the disk, as did C_T and c_d , which explains the behavior of the bending moments.

Figures 41(a) and 41(b) show the modulus of the harmonics of the oscillatory edgewise and flapwise bending moments, respectively, as a function of the number of the harmonic, n . The 1/rev is the dominant harmonic. There is an increase in the modulus of both bending moments because of the body for $n = 1$ to $n = 3$. The peak in the area of $n = 5$ for the edgewise bending moment is due to a coupled flap-lag blade natural frequency near 5Ω . The effect of the body is thus not just a local phenomenon, but rather changes the entire pattern of blade loading.

RESULTS: ROTOR-BODY AERODYNAMIC INTERFERENCE

The effects of the body on rotor performance and loads will be examined for cases 2 to 5 of table 4. Even though the modified slender body theory has been developed here only for axisymmetric bodies at zero angle of attack, a number of practical configurations can be analyzed: a typical full-scale rotor test in the Ames 40- by 80-Foot Wind Tunnel; the Ames small-scale interactional aerodynamics tests; the future Ames full-scale interactional aerodynamics tests; and a rotor-hybrid airship configuration.

Wind Tunnel Test Modules

The next step in the analysis was to model the test modules used in the 40- by 80-Foot Wind Tunnel at Ames and to determine their effects on rotor performance and loads.

Figure 42 shows the shapes of the RTA and EE test modules. Modified slender body theory modeled these shapes with no significant error in body streamlines (recall that these test modules are modeled with the tails extended to a point). All the following results for the influence of the RTA and EE test modules were obtained using the modified slender body theory with tail correction.

The surface pressure distribution on a 1/6-scale EE, obtained from reference 8, is compared with the distribution calculated by the modified slender body theory with tail correction in figure 43. The theory compares well with the data and with the panel code from reference 8, except for $x > 0.95$. An explanation for the lack of agreement in this vicinity is that the data represent the occurrence of flow separation. The theory, at this stage of development, does not model separation. The influence of the rotor on the body pressure is greater than the error caused by separation at the tail (see ref. 8).

Full-Scale Test Configuration

The combination of rotor B and the RTA is a configuration typical of a full-scale wind tunnel test in the Ames 40- by 80-Foot Wind Tunnel. Such tests are intended to measure the isolated rotor characteristics. Figures 44 to 50 were generated under the conditions of case 2 in table 4. Figure 44 shows the change in angle of attack produced by the RTA for the baseline values of case 2. The advance ratio is 0.4.

Figure 45 shows the increase in the lift-to-drag ratio of rotor B caused by the RTA for various advance ratios. As shown, there is a negligible performance improvement caused by the RTA ($\Delta(L/D) = 0$ to 0.2). The profile and induced power are basically

unaffected by the presence of the body; the change in L/D is due almost entirely to the interference power.

Figures 46(a) and 46(b) show the increase in the oscillatory edgewise and flapwise bending moments, respectively. The edgewise moments, which were calculated at the 60% radial station, show a 10%-15% increase because of the body. The flapwise bending moments, which were calculated at the 70% radial station, show a 5%-10% increase caused by the RTA. The calculated influence of the RTA on the pitch-link loads was negligible ($\pm 2\%$).

Figure 47 shows the lift-to-drag ratio of rotor B with and without the presence of the RTA for various advance ratios. As noted earlier, very little change is caused by the body. Figures 48(a) and 48(b) show the edgewise and flapwise bending moments, respectively.

Figures 49(a) and 49(b) show the time histories of the edgewise and flapwise bending moments, respectively. The advance ratio is 0.5 and the C_T/σ is 0.07. The edgewise moment shows small changes at a few azimuth locations. The flapwise moment shows almost no change as the blade progresses around the rotor disk. Figure 50 shows the moduli of the harmonics of the edgewise bending moment as a function of the harmonic number.

Small-Scale Interactional Aerodynamic Test Configurations

To simulate some of the small-scale rotor-body interactional tests conducted at Ames (refs. 6-8), the effects of scaled-models of the RTA and EE on rotor A were analyzed.

Figures 51(a) and 51(b) show the change in angle of attack of the rotor blade caused by the EE for the two longitudinal hub positions in case 3. The baseline values for the advance ratio and the rotor-body vertical separation were used. Moving the hub position aft, as shown in figure 51(b), changes the angle of attack distribution significantly.

The baseline conditions of case 3 in table 4 apply to table 7 and to figures 51 to 55. The parameter variations for case 3 were chosen to match those in reference 7. The baseline configurations for the RTA and EE approximately model the full-scale test configurations.

Figure 52 shows the lift-to-drag ratio for rotor A as affected by the RTA and EE for the baseline configuration at two different advance ratios. The decrease in L/D caused by the EE increases as the advance ratio is increased. The RTA causes a small increase in L/D at the higher advance ratio.

Figure 53 shows the effect of changing hub position on the lift-to-drag ratio. The body used is the EE. Moving the hub aft with respect to the body nose creates a positive increase in L/D as compared with the isolated rotor. The advance ratio for figure 53 is 0.3. Table 7 shows the contributions to the power at $C_T/\sigma = 0.07$ for the isolated rotor case, and for the cases of rotor A in combination with the RTA and EE. There are small increases in the profile and induced power, but the change in the total performance is due primarily to the direct interference power. Figures 54(a) and 54(b) show the change in L/D caused by variations in advance ratio, rotor height, and hub position for the RTA and EE, respectively. In figure 54(a), the variation in rotor height has little effect on the change in L/D . Moving the rotor aft with respect to the body nose increases the change in L/D . The increase in advance ratio from $\mu = 0.15$ to 0.2 causes a decrease in $\Delta(L/D)$. As

μ is increased from 0.2 to 0.3, however, $\Delta(L/D)$ is increased. For the EE, increasing the rotor height causes a small increase in $\Delta(L/D)$ as shown in figure 54(b). As the hub position is moved aft, there is an increase of $\Delta(L/D)$ of about 0.4. The increase in advance ratio causes $\Delta(L/D)$ to decrease.

Figure 55 shows the lift-to-drag ratio for rotor A as affected by the EE for various tip-path-plane angles at an advance ratio of 0.3. As α_{TPP} becomes more negative, L/D is seen to decrease. Figures 56(a) and 56(b) show the change in L/D as affected by the RTA and EE, respectively, for several tip-path-plane angles at an advance ratio of 0.3. Figure 56(a) does not show any discernible trend of $\Delta(L/D)$ with α_{TPP} , whereas in figure 56(b), $\Delta(L/D)$ is seen to become less negative as α_{TPP} becomes more negative.

Although these calculations are for the small-scale test configurations of references 6-8, it is not possible to validate the theory using the rotor performance data of reference 6, a result of the systematic error now believed to exist in the data. Reference 6 gives data for the rotor alone and with the RTA model. Figure 4 of reference 6 shows no trend of the isolated rotor performance with α_{TPP} , whereas the calculations show $\Delta(L/D) = 0.5$ to 1.0 for an 8° change in α_{TPP} (fig. 55). Figures 5(a) and 8(b) of reference 6 show changes in $\Delta(L/D)$ of the order of 0.5 for the range of advance ratios, hub positions, and rotor-body separation distances investigated; but the calculations show an influence of these parameters that is much less (fig. 54(a)). Hence, all that can be concluded is that the calculations support the conclusion that there are systematic errors of the order of 0.5 in the measured rotor L/D .

Full-Scale Interactional Aerodynamic Test Configurations

The combination of EE and rotor C is a configuration to be used as part of the full-scale interactional aerodynamic tests at Ames (case 4 of table 4). Table 8 shows the contributions to the power coefficient for the baseline values of case 4. Comparing tables 7 and 8, shifting the hub position aft has a less favorable effect on the interference power for rotor C than for rotor A. Also, the induced power shows an increase as a result of the aft shift in hub position for rotor C, whereas rotor A shows a decrease in the induced power as well as in the profile power. Table 8 shows an overall net performance gain of 2% caused by the aft shift in hub position, whereas table 7 shows a 6% net performance gain.

Figure 57 shows the effect of the hub position on the lift-to-drag ratio at two advance ratios. Figure 58 shows the effect of hub position on the change in L/D caused by the presence of the EE at two advance ratios. The effect of the EE is seen to be very small ($\Delta(L/D) = \pm 0.1$). Figures 59(a) and 59(b) show the increase caused by the EE in the oscillatory edgewise and flapwise bending moments, respectively, as affected by the hub position at two advance ratios. The moments were calculated at the 50% radial station. The change in the edgewise bending moment decreases as the advance ratio is increased (hub position fixed), and increases as the hub position is moved aft (advance ratio fixed). The change in the flapwise bending moment, however, increases as the advance ratio is increased.

Figures 60(a) and 60(b) show the oscillatory edgewise and flapwise bending moments, respectively, as affected by the hub position at two advance ratios. The edgewise moment shows an increase of 10%-20% caused by the body for the baseline hub position and a 25%-45% increase for the aft hub position. The flapwise moment shows an increase of 5%-15% because of the body. There is little effect of the hub position

on the flapwise moment. The calculated effect of the EE on the pitch link loads was small (a 4%-8% increase).

Figures 61 and 62 show the time histories of the bending moments at the 50% radial station for $C_T/\sigma = 0.07$. The advance ratio is 0.3 and 0.4 for figures 61 and 62, respectively. The effect of the EE on the edgewise moment is greatest at the front of the rotor disk. The flapwise moment shows small changes caused by the body at various locations on the rotor disk. Figure 63 shows the moduli of the harmonics of the edgewise moment as a function of the harmonic number.

Rotor-Airship Interference

Because an airship is similar in shape to an ellipsoid, performance calculations were made for a typical hybrid airship configuration using a 50%-thick ellipsoid. Case 5 of table 4 lists the parameter values used for the calculations. This aircraft operates at low speed ($\mu = 0.15$ here). Four rotors, two forward and two aft, were placed at the bottom edge of the body. Figure 64 shows the lift-to-drag ratio of a front rotor and a rear rotor. The presence of such a large body produces a significant effect on the L/D. The L/D of the rear rotor is seen to increase by approximately 17%, and the L/D of the front rotor decreases by 15%. The effect of the body had negligible influence on the profile and the induced power. The effect on power required was due almost entirely to the interference power. Note that the induced velocity is downward at the front of the body and upward at the rear of the body.

COMPUTATION EFFICIENCY

The computational efficiency of modified slender body theory can be assessed by comparing the time required for the body analysis and the time needed for the rotor portion of the analysis. The amount of time required for the body analyses depended on the frequency at which the body velocities were updated within CAMRAD. Two approaches were used to estimate the computational efficiency of the body analysis.

1. Update body velocities (over entire rotor disk) once per wake iteration (OPINTV = 2).
2. Update body velocities once per control change in trim iteration (OPINTV = 3)

One wake iteration involves typically 5 to 15 steps of control changes (see fig. 8). Note that the rotor analysis begins with a uniform inflow solution, then proceeds to a nonuniform inflow with prescribed wake geometry (iterated if desired), and then to a nonuniform inflow with free wake geometry (iterated if desired) (see fig. 9(a) and refs. 17-18).

Approach (2) can be considered a fully converged body velocity calculation, since the rotor motion, hence the rotor position relative to the body, changes very little during the final steps of the trim iteration (see fig. 8). The following table shows the percentage of the time required for the entire job that was used in the wake influence coefficient calculations and the body induced velocity calculations using (1) and (2). Approach (2) requires more updates (a factor of 10-20) of the body-induced velocities than approach (1).

Approach	Wake influence coefficient calculation, %	Body velocity calculation, %
1	35-40	5-10
2	15-25	40-70

Regarding the accuracy of approaches (1) and (2), approach (1) with two wake iterations gave less than a 1% difference in performance and loads than approach (2). Also, approach (1), with two iterations, required about the same total time, or even less, than approach (2), with one wake iteration. For an optimally accurate and computationally efficient solution, a more complex method of determining when to update the body-induced velocities is needed. It would be sufficient to update the body velocities three to five times at the beginning of the trim iteration. Updating the velocities at the end of each trim iteration degrades the efficiency significantly, as seen by the results of approach (2). Listed below is a summary of relative computation times required by the different analyses.

Analysis	Relative time
Body-induced velocities calculated by modified slender body theory	15-25
Free wake geometry	60-100
Wake influence coefficient matrix	150-200
Complete rotor solution (each wake iteration)	400-600
Body-induced velocities calculated by panel method	1000-3000

If the body velocities are updated 3-5 times per wake iteration in the rotor solution, then the body velocities, as calculated by modified slender body theory, will require 10%-20% of the time required for a complete rotor solution. If a panel method is used, however, the time required to calculate the velocities will be 2-6 times that required for a complete rotor solution, depending on the complexity of the panel code. (Although a more efficient panel code could be constructed for the case of an axisymmetric body at zero angle of attack, the above comparison of computation time refers to the more general problem.)

CONCLUSIONS

Modified slender body theory was used to assess body-induced effects on rotor behavior. The effects of several body shapes on three different rotors were studied. The wide range of configurations covered was made possible by the computational efficiency of the body model. Conclusions drawn from this study are listed below.

1. Moderately thick ellipsoids are modeled well by modified slender body theory.

2. The streamlines of body shapes with pointed ends can be closely matched by the modified slender body theory with tail correction, but a trial and error procedure is necessary to find ξ_1 and ξ_2 .

3. In assessing the effects of simple body shapes on the rotor, slender body theory produced significant errors (relative to the exact solution) except for thin shapes, whereas the modified slender body theory was accurate for moderately thick bodies.

4. Since the body-induced effects depend on the detailed aerodynamic environment of the rotor blade, nonuniform inflow induced velocity calculations must be used in the rotor analysis. A free wake model produced essentially the same results as a prescribed wake geometry model, implying that the neglect of body-induced distortions of the wake geometry is acceptable.

5. The calculated influence of the body on the rotor performance was generally small for the cases considered here. The direct interference power can be positive or negative, depending on the body configuration. The interference power is typically not zero, even for cases with exact fore-aft symmetry of the interference velocity, a result of the asymmetry of the rotor loading distribution. For the cases considered here, the profile power and induced power were always increased by the presence of the body. The profile power increase was generally greater than the induced power increase. The net performance change caused by the body could be favorable or unfavorable, depending on the sign of the direct interference power and its magnitude relative to the profile power change.

6. The calculated oscillatory blade bending moments were always increased by the body for the cases considered here. The edgewise bending moment changes were larger than the flapwise bending moment changes. In some cases, the loads were increased by a significant fraction of the isolated rotor loads. The interference effects were due to the general changes in the rotor flow pattern, rather than to localized effects of the body. The influence of the body on the blade loads occurred primarily on the front of the rotor disk. No significant effects on pitch link loads were found.

7. For the case of a typical full-scale rotor test in the 40- by 80-Foot Wind Tunnel, negligible effects of the Rotor Test Apparatus (RTA) on the rotor performance and pitch link loads were calculated. Only small increases in the blade bending moments were found. Hence, such a test does produce essentially isolated rotor behavior.

8. For the case of the Ames small-scale aerodynamic interference tests, a performance change of about $\Delta(L/D) = 0.2$ was predicted for the Easter Egg (EE) body shape. A 6% performance change ($\Delta(L/D) = 0.4$) was calculated for the two body longitudinal positions tested. The corresponding influence of the RTA body shape was small. The calculated influence of rotor-body vertical separation was small for both body shapes.

9. For the case of the Ames full-scale aerodynamic interference tests, it is predicted that the EE body will produce negligible performance changes. The oscillatory edgewise bending moments will be 10%-20% higher than for the isolated rotor with the EE at the baseline position. If the EE body were shifted forward, the loads would be 25%-45% higher than for the isolated rotor. Smaller effects are predicted for the influence of the body on the flapwise bending moment.

10. For the case of a rotor-hybrid airship, a significant performance increase and decrease were predicted for the rear and front rotors, respectively ($\Delta(L/D) = \pm 15\%$).

11. The computational efficiency of the body model is one or two orders of magnitude better than that of a typical potential flow panel code. The body analysis using the modified slender body theory required only 10% to 20% of the computation time required for the rotor analysis.

RECOMMENDATIONS

The predicted influence of the body on the rotor should be verified by comparison with experimental data. Such comparisons should be done initially for simple shapes, such as the RTA and EE wind tunnel test modules, for which the accuracy of the isolated body analysis is well established.

The modified slender body theory should be extended to eliminate the restrictions to axisymmetric bodies and zero body angle of attack. It is anticipated that the computational efficiency of the method will be easily maintained, but that some loss in accuracy representing the body streamline will result. The present results imply that for practical shapes the accuracy will remain acceptable. Techniques for modeling flow separation should be established, and a more general approach for the pointed-tail correction would be desirable. The incorporation of rotor-induced effects on the body aerodynamics should also be considered for the modified slender body theory.

REFERENCES

1. Sheridan, P. F.; and Smith, R. P.: Interactional Aerodynamics — A New Challenge to Helicopter Technology. J. Am. Helicopter Soc., vol. 25, no. 1, 1980.
2. Wilby, P. G.; Young, G.; and Grant, J.: An Investigation of the Influence of Fuselage Flow Field on Rotor Loads and the Effects of Vehicle Configuration. Vertica, vol. 3, no. 2, 1979.
3. Freeman, C. E.; and Wilson, J. C.: Rotor-Body Interference (ROBIN) — Analysis and Test. 36th Annual Forum of the American Helicopter Society, Washington, D.C., May 1980.
4. Clark, D. R.; and Maskew, B.: Calculation of Rotor/Airframe Interference for Realistic Configurations. European Rotorcraft and Powered Lift Aircraft Forum, Aix-en-Provence, France, Sept. 1982.
5. Johnson, W.: Development of a Comprehensive Analysis for Rotorcraft. Vertica, vol. 5, nos. 2 and 3, 1981.
6. Betzina, M. D.; and Shinoda, P.: Aerodynamic Interactions between a 1/6-Scale Helicopter Rotor and a Body of Revolution. NASA TM-84247, 1982.
7. Betzina, M. D.; Smith, C. A.; and Shinoda, P.: Rotor/Body Aerodynamic Interactions. NASA TM-85844, 1983.
8. Smith, C. A.; and Betzina, M. D.: A Study of the Aerodynamic Interaction between a Main Rotor and a Fuselage. 39th Annual Forum of the American Helicopter Society, St. Louis, Mo., May 1983.
9. Huber, H.; and Polz, G.: Studies on Blade-to-Blade and Rotor-Fuselage-Tail Interference. AGARD Conference Proceedings No. 334, London, May 1982.
10. Landgrebe, A. J.; Moffitt, R. C.; and Clark, D. R.: Aerodynamic Technology for Advanced Rotorcraft. J. Am. Helicopter Soc., vol. 22, no. 3, July 1977.
11. Jepson, D.; Moffitt, R.; Hilzinger, K.; and Bissell, J.: Analysis and Correlation of Test Data from an Advanced Technology Rotor System. NASA CR-3714, 1983.
12. Sheridan, P. F.: Interactional Aerodynamics of the Single Rotor Helicopter Configuration. U.S. Army Research and Technology Laboratories, TR 78-23, Sept. 1978.
13. Wilson, J. C.; and Mineck, R. E.: Wind-Tunnel Investigation of Helicopter-Rotor Wake Effects on Three Helicopter Fuselage Models. NASA TM X-3185, 1975.
14. Curle, N.; and Davies, H. J.: Modern Fluid Dynamics. D. Van Nostrand Company, Ltd., Canada, 1968.
15. Thwaites, B.: Incompressible Aerodynamics. Clarendon Press, Oxford, 1960.

16. Durand, W. F., ed.: Aerodynamic Theory, Vol. I. Julius Springer, Berlin, 1934.
17. Johnson, W.: A Comprehensive Analytical Model of Rotorcraft Aerodynamics and Dynamics. Part I. Analysis Development. NASA TM-81182, 1980.
18. Johnson, W.: A Comprehensive Analytical Model of Rotorcraft Aerodynamics and Dynamics. Part II. User's Manual. NASA TM-81183, 1980.
19. Johnson, W.: Performance and Loads Data from a Wind Tunnel Test of a Full-Scale Rotor with Four Blade Tip Planforms. NASA TM-81229, 1980.

TABLE 1.- EQUATIONS FOR VARIOUS BODY SHAPES

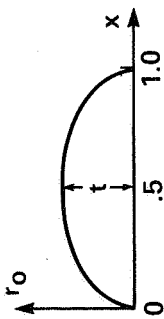
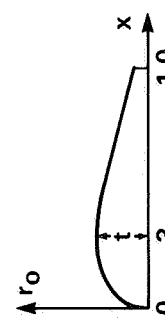
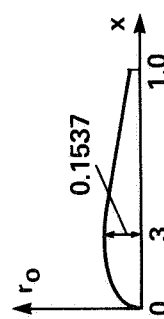
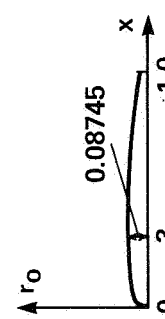
BODY	GEOMETRY	$r_o(x)$
ELLIPSE		$r_o(x) = t \sqrt{1 - \left(\frac{x - 0.5}{0.5}\right)^2}$
NACA AIRFOIL		$r_o(x) = \frac{t}{0.10} (0.2969 \sqrt{x - 0.1260x} - 0.3516x^2 + 0.2843x^3 - 0.1036x^4)$
EASTER EGG		$0 \leq x \leq 0.6987 : r_o(x) = \frac{0.1537}{0.10} (0.2969 \sqrt{x - 0.1260x} - 0.3516x^2 + 0.2843x^3 - 0.1015x^4)$ $0.6987 < x \leq 0.99069 : r_o(x) = -0.248755 (x - 1.077308)$ $x > 0.99069 : r_o(x) = \sqrt{(0.012271375)^2 - (x - 0.987728625)^2}$
RTA		$0 \leq x \leq x_1 : r_o(x) = \sqrt{(0.058497075)^2 - (x - 0.058497075)^2}$ $x_1 < x \leq x_2 : r_o(x) = 0.2503817x + 0.045618326$ $x_2 < x \leq x_3 : r_o(x) = 0.1366667x + 0.061821902$ $x_3 < x \leq x_4 : r_o(x) = 0.087445627$ $x_4 < x \leq x_5 : r_o(x) = -0.04819277x + 0.107085609$ $x_5 < x \leq x_6 : r_o(x) = -0.08504854x + 0.123023088$ $x_6 < x \leq x_7 : r_o(x) = -0.1407186x + 0.168597889$ $x_7 < x \leq x_8 : r_o(x) = -0.2013423x + 0.221265129$ $x_8 < x \leq 1.0 : r_o(x) = \sqrt{(0.024298785)^2 - (x - 0.975701214)^2}$ $x_1 = 0.044247787 \quad x_3 = 0.187490625 \quad x_5 = 0.432428378 \quad x_7 = 0.868756562$ $x_2 = 0.142492875 \quad x_4 = 0.407529623 \quad x_6 = 0.818659067 \quad x_8 = 0.980500975$

TABLE 2.- VALUES OF ξ_1 , ξ_2 , a_0 , AND KN FOR DIFFERENT BODY SHAPES

Body	Thickness ratio, %	t	RCN	RCT	ξ_1	ξ_2	a_0	KN	Extended length
Ellipsoid	60	0.30	0.18	0.18	---	---	---	2.3227	---
Ellipsoid	80	.40	.32	.32	---	---	---	4.5377	---
Sphere	100	.50	.50	.50	---	---	---	12.8526	---
NACA airfoil	10	.05	.0110	0	0.10	0.95	0.4629	1.2680	---
NACA airfoil	30	.15	.0992	0	.10	.95	.4629	2.6539	---
NACA airfoil	50	.25	.2755	0	.10	.95	.4629	5.5858	---
RTA	17.49	.08745	.0585	0	.05	.06	15.4504	.9261	1.0990
EE	30.74	.1537	.6774	0	.10	.65	.8530	2.2642	1.0773

TABLE 3.- ROTOR TYPES USED IN ANALYSIS

Type	Rotor A (teetering)	Rotor B (articulated)	Rotor C (articulated)
Number of blades	2	4	4
Radius, m	1.12	6.71	7.01
Solidity ratio	.0651	.0748	.0705
Twist, deg	-10	-10 (nonlinear)	-14 (nonlinear)
Lock number	3.44	9.08	7.19
Tip Mach number	.60	.60	.70

TABLE 4.- SUMMARY OF CASES

	Case 1	Case 2	Case 3	Case 4	Case 5
Rotor	A, B	B	A	C	A
μ	0.4	0.3, 0.4, 0.5	0.15, 0.2, 0.3 ^a	0.3, α 0.4	0.15
α_s	0	0	0	-4	0
β_{1c}	4	0	0, α 4, 8	0	0
α_{TPP}	-4	0	0, α -4, 8	-4	0
Body	Ellipsoids	RTA	Model RTA	EE	Ellipsoid
λ/R	1.0	1.5152	1.515	0.942	8.0
T/ λ	0.6, 0.8, α 1.0	.1749	.1749	.3074	.5
(x/ λ)hub ^b	0.1, 0.3, α 0.5	.295	0.295, α 0.355	0.206, α 0.500	0.25, 0.75
($\Delta z/\lambda$)hub ^c	0.5	.088	0.053, α 0.068	0.85	-0.466
(y/ λ)hub ^d	.1	0	0.057, 0.070, α 0.101	0	\pm .375
	0	0	0	0	

Notes: Case 1 = assessment of modified slender body theory; Case 2 = typical full-scale rotor in 40- by 80-Foot Wind Tunnel; Case 3 = Ames model interactional aerodynamics tests; Case 4 = full-scale interactional aerodynamics tests; Case 5 = hybrid airship.

^aBaseline. ^bRelative to nose. ^cRelative to top of body. ^dRelative to centerline.

TABLE 5.- PERFORMANCE LOSSES FOR ROTOR A AT $C_T/\sigma = 0.08$ WITH 80%-THICK ELLIPSOID (CASE 1)

	Trim to $\alpha_{TPP} = 0^\circ$			Trim to $PF^\alpha = 0$		
	With body	No body	Difference	With body	No body	Difference
	C_{p_i}/σ (induced power)	0.00226	0.00187	0.00039	0.00237	0.00191
$C_{p_{int}}/\sigma$ (interference power)	-.00066	0	-.00066	-.00072	0	-.00072
C_{p_o}/σ (profile power)	.00426	.00305	.00121	.00437	.00312	.00125
$C_p/\sigma = \frac{(C_{p_i} + C_{p_{int}} + C_{p_o})}{\sigma}$.00586	.00492	.00094	.00602	.00503	.00101
L/D	5.46	6.50	-1.04	5.32	6.36	-1.04
α_{TPP}	0	0	0	1.01	.43	.58
$(\beta_{1s})_{NFP}^b$	-3.99	-1.51	-2.48	-4.03	-1.53	-2.50
$(\beta_{1c})_{NFP}^c$	-9.18	-8.59	-.59	-9.53	-8.78	-.75

^aPropulsive force.

^bLateral tip-path-plane angle in the no-feathering-plane coordinate system.

^cLongitudinal tip-path-plane angle in the no-feathering-plane coordinate system.

TABLE 6.- PERFORMANCE CHANGES FOR ROTOR B WITH 80%-THICK ELLIPSOID (CASE 1)

	Trim to $C_T/\sigma = 0.06$			Trim to $C_T/\sigma = 0.09$		
	With body	No body	Difference	With body	No body	Difference
C_{p_i}/σ (induced power)	0.00127	0.00090	0.00037	0.00231	0.00180	0.00051
$C_{p_{int}}/\sigma$ (interference power)	-.00087	0	-.00087	-.00094	0	-.00094
C_{p_o}/σ (profile power)	.00202	.00169	.00033	.00309	.00244	.00065
$C_p/\sigma = \frac{(C_{p_i} + C_{p_{int}} + C_{p_o})}{\sigma}$.00242	.00259	-.00017	.00446	.00424	.00022
L/D	9.94	9.27	.67	8.12	8.50	-.38

TABLE 7.- PERFORMANCE CHANGES FOR ROTOR A WITH
RTA AND EE (CASE 3)

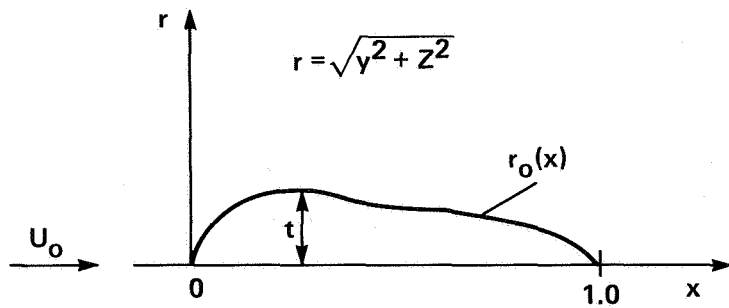
	Trim to $C_T/\sigma = 0.07$			
	Isolated rotor	With RTA	With EE	With EE ^a
C_{P_i}/σ (induced power)	0.00102	0.00103	0.00106	0.00104
$C_{P_{int}}/\sigma$ (interference power)	---	-.00005	.00001	-.00012
C_{P_o}/σ (profile power)	.00178	.00181	.00182	.00181
$C_p/\sigma = \frac{(C_{P_i} + C_{P_{int}} + C_{P_o})}{\sigma}$.00280	.00279	.00289	.00273
$\Delta(C_{P_i}/\sigma)$	---	.00001	.00004	.00002
$\Delta(C_{P_{int}}/\sigma)$	---	-.00005	.00001	-.00012
$\Delta(C_{P_o}/\sigma)$	---	.00003	.00004	.00003
$\Delta C_p/\sigma$	---	-.00001	.00009	-.00007
L/D	7.50	7.54	7.26	7.70

^a $(x/l)_{hub} = 0.471.$

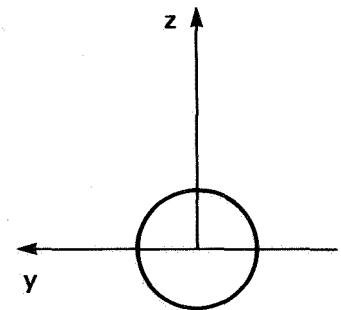
TABLE 8.- PERFORMANCE CHANGES FOR ROTOR C
WITH EE (CASE 4)

	Trim to $C_T/\sigma = 0.07$		
	Isolated rotor	With EE	With EE ^a
C_{p_i}/σ (induced power)	0.00116	0.00120	0.00122
$C_{p_{int}}/\sigma$ (interference power)	---	-.00004	-.00011
C_{p_o}/σ (profile power)	.00185	.00187	.00187
$C_p/\sigma = \frac{(C_{p_i} + C_{p_{int}} + C_{p_o})}{\sigma}$.00301	.00304	.00298
$\Delta(C_{p_i}/\sigma)$	---	.00004	.00006
$\Delta(C_{p_{int}}/\sigma)$	---	-.00004	-.00011
$\Delta(C_{p_o}/\sigma)$	---	.00002	.00002
$\Delta(C_p/\sigma)$	---	.00003	-.00003
L/D	6.99	6.92	7.05

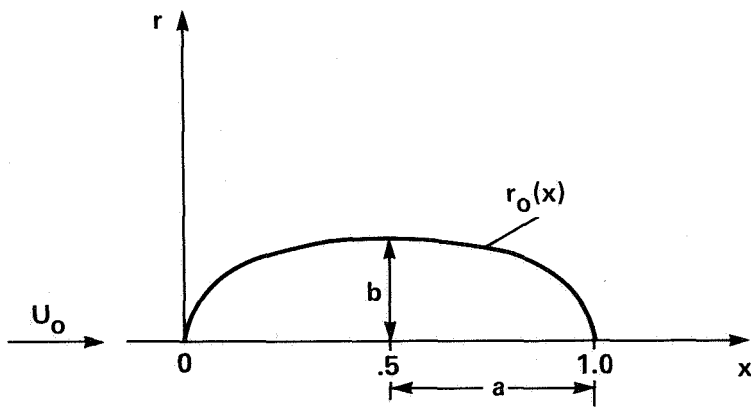
^a $\alpha(x/l)_{hub} = 0.500.$



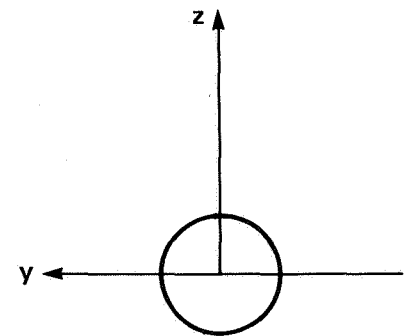
(a)



LOOKING AFT

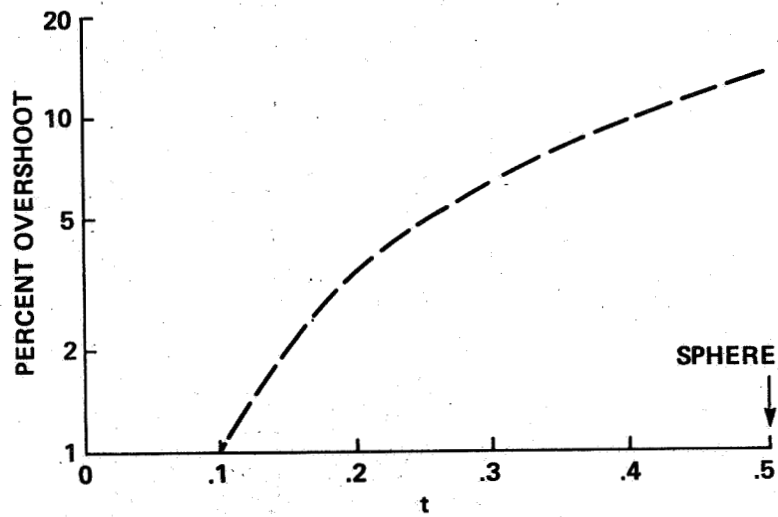


(b)

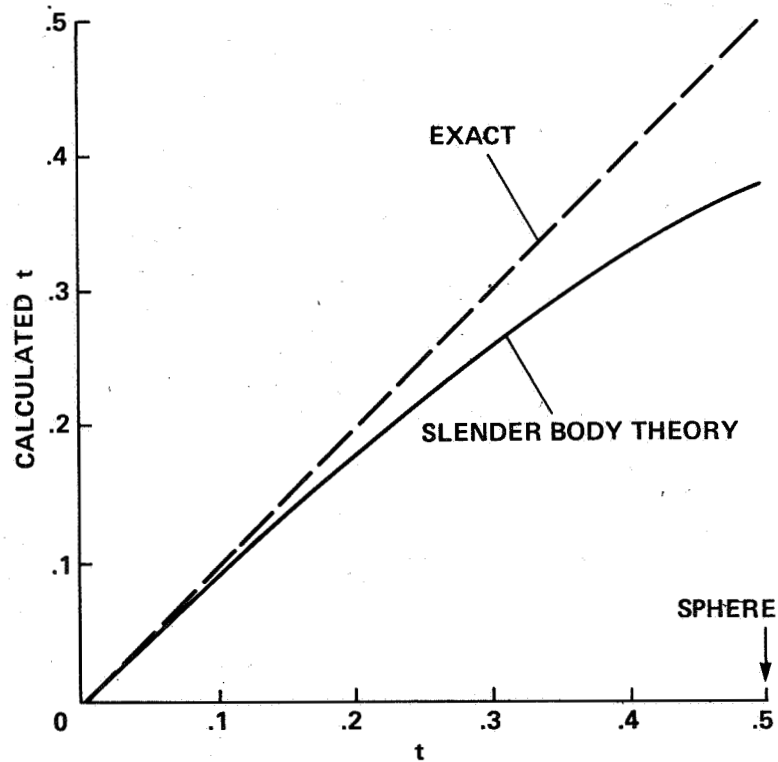


LOOKING AFT

Figure 1.- Coordinate system and geometry used to define body shapes.
 (a) General axisymmetric body; (b) prolate spheroid.



(a) Amount of overshoot of stagnation point as a percent of body length using slender body theory for ellipsoids.



(b) Calculated maximum thickness using slender body theory for ellipsoids.

Figure 2.- Amount of overshoot of stagnation point and calculated maximum thickness.

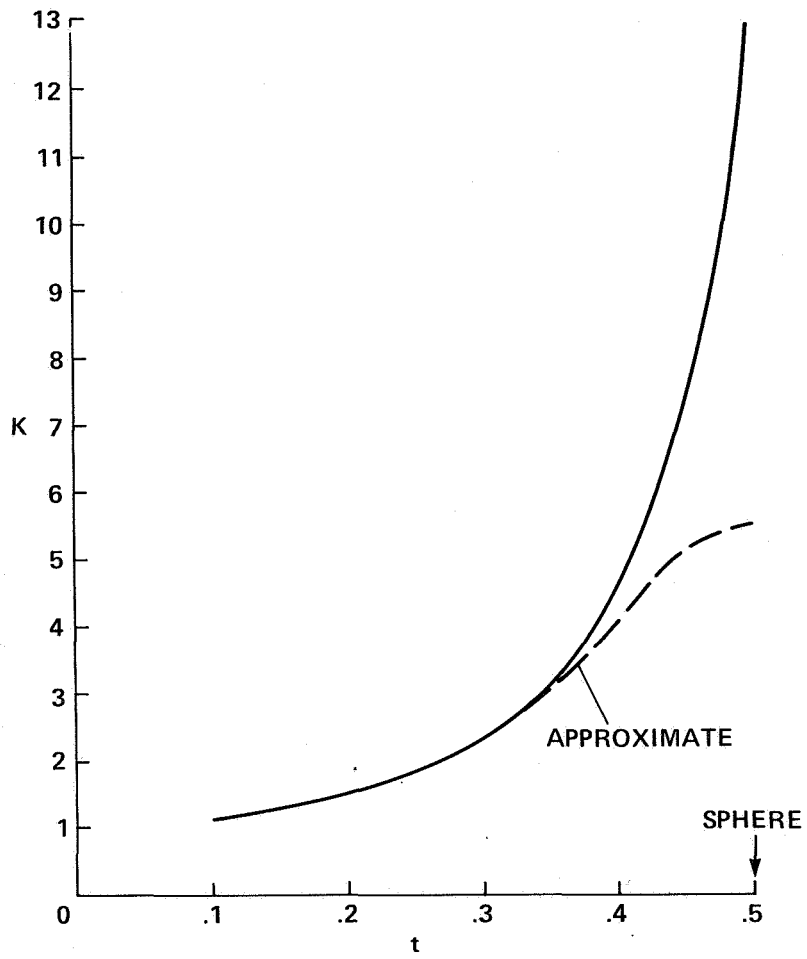


Figure 3.- K versus maximum thickness for ellipsoids.

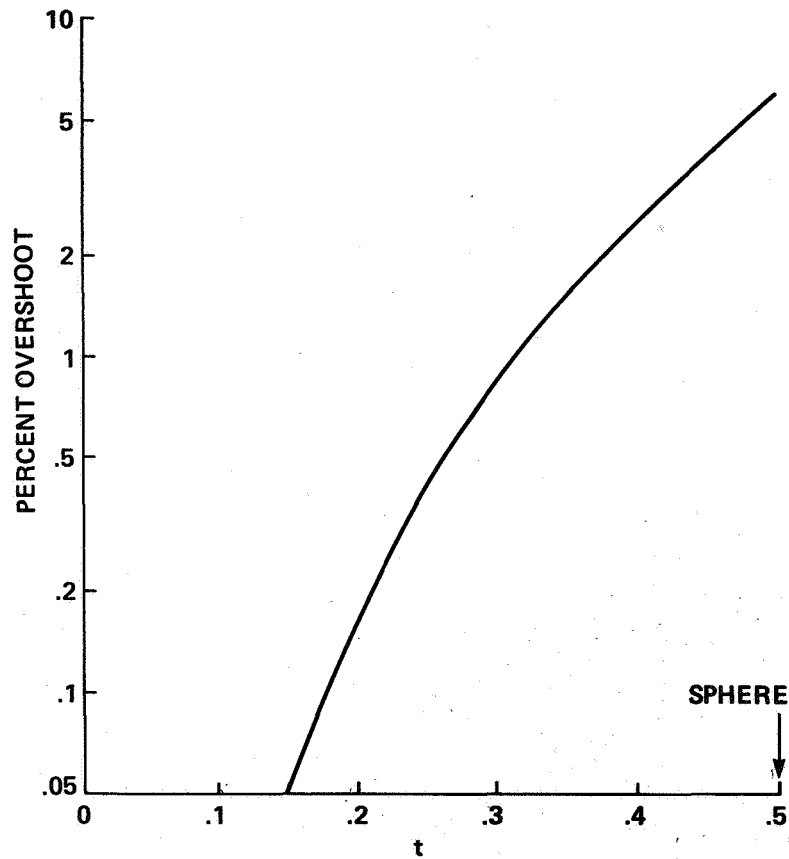


Figure 4.- Amount of overshoot of stagnation point as a percent of body length using modified slender body theory for ellipsoids.

MAIN PROGRAM

INITIALIZE

N

U_0

t

x

r_1

ψ_0

CALL STREAM (x, r_1 , ψ_1)

5 $r_2 = r_1 - \Delta r$

CALL STREAM (x, r_2 , ψ_2)

IF ($\psi_1 < \psi_0 < \psi_2$) GO TO 10

$r_1 = r_2$

$\psi_1 = \psi_2$

GO TO 5

10 $rr = 0$

15 $r = (r_1 + r_2)/2$

CALL STREAM (x, r, ψ)

IF ($|rr - r| \leq \epsilon$) GO TO 100

IF ($\psi < \psi_0$) $r_1 = r$

IF ($\psi > \psi_0$) $r_2 = r$

$rr = r$

GO TO 15

100 PRINT x, r, ψ

CALL VEL (x, r, U_x , U_r)

PRINT U_x , U_r

STOP

END

(a) Summary of main program.

Figure 5.- Procedure for calculating streamlines and velocities.

SUBROUTINE STREAM (x, r, ψ)

$$H = \frac{BB - AA}{N}$$

$$\xi = 0$$

DO 100 I = 1, N

$$\xi = \xi + H$$

$$\xi^* = \frac{\xi - RCN/2}{1 - RCA}$$

SUBROUTINE BODY SHAPE (ξ^* , q)

$$r_o = r_o(\xi^*)$$

$$r_o' = r_o'(\xi^*)$$

$$q = r_o * r_o'$$

RETURN

$$100 \psi_N = \psi(x, r, \xi, q(\xi^*))$$

$$\psi = \sum \psi_N$$

RETURN

(b) Summary of stream function and body shape subroutines.

Figure 5.- Continued.

MAIN PROGRAM

```
•
•
•
SUBROUTINE STREAM (x, r, ψ)
•
•
•

$$\xi^* = \frac{\xi - RCN}{2}$$


$$1 - RCA$$

SUBROUTINE BODY SHAPE (ξ*)
COMPUTE XE
COMPUTE f (ξ1, ξ2, KN already known at this stage)
ξ* = XE * ξ*
ro = ro(ξ*) / XE
r'o = r'o(ξ*)
ξ* = ξ* / XE
q = KN * r'o + f * (ξ* - 1) * (1 - KN * ξ*) * (r'o(1))2
RETURN
CALCULATE ψ
RETURN
•
•
•
END
```

(c) Procedure for inclusion of an extended tail.

Figure 5.- Concluded.

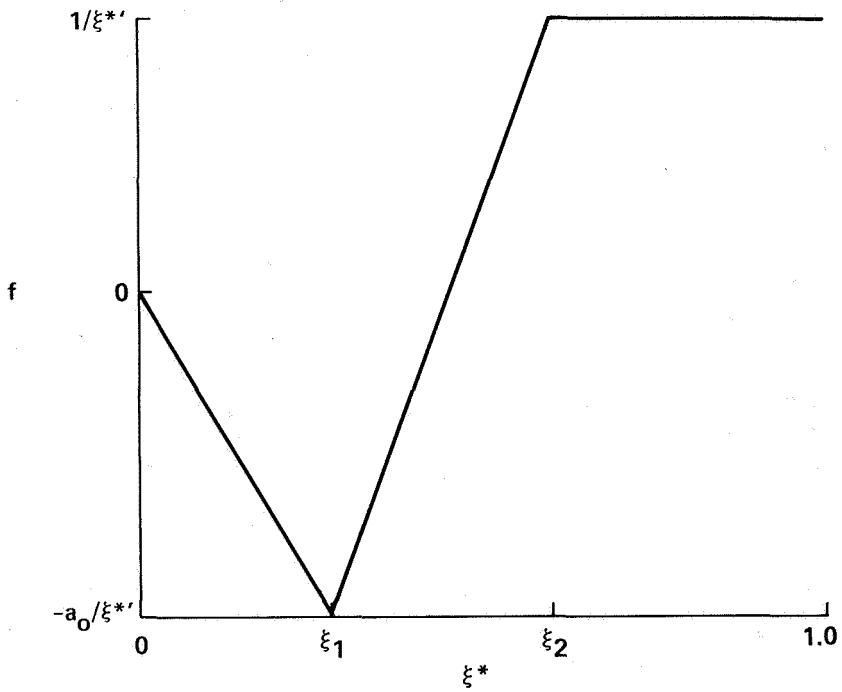


Figure 6.- Function f for tail correction.

- (X, Y, Z): COORDINATE SYSTEM WITH ORIGIN AT BODY NOSE
- (X_S, Y_S, Z_S): COORDINATE SYSTEM WITH ORIGIN AT HUB
- (X_F, Y_F, Z_F): COORDINATE SYSTEM WITH ORIGIN AT CG

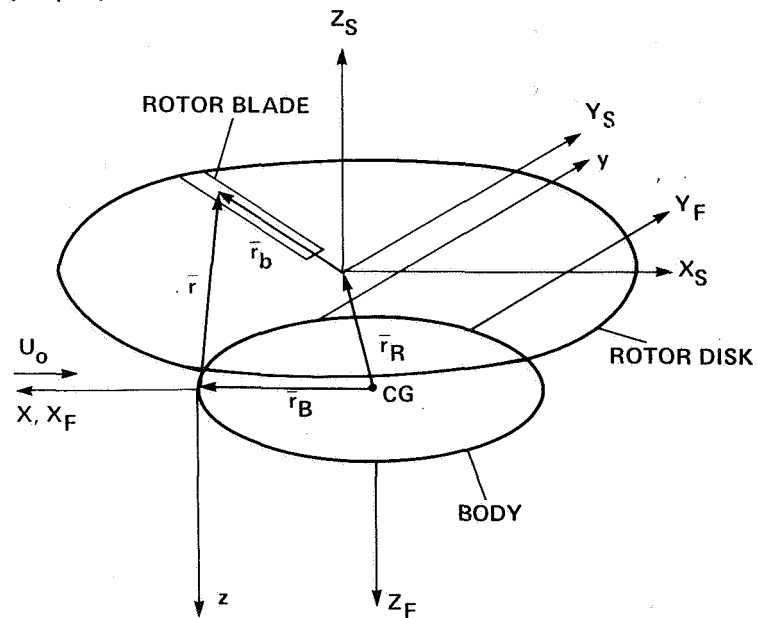


Figure 7.- Blade position on rotor disk relative to body origin.

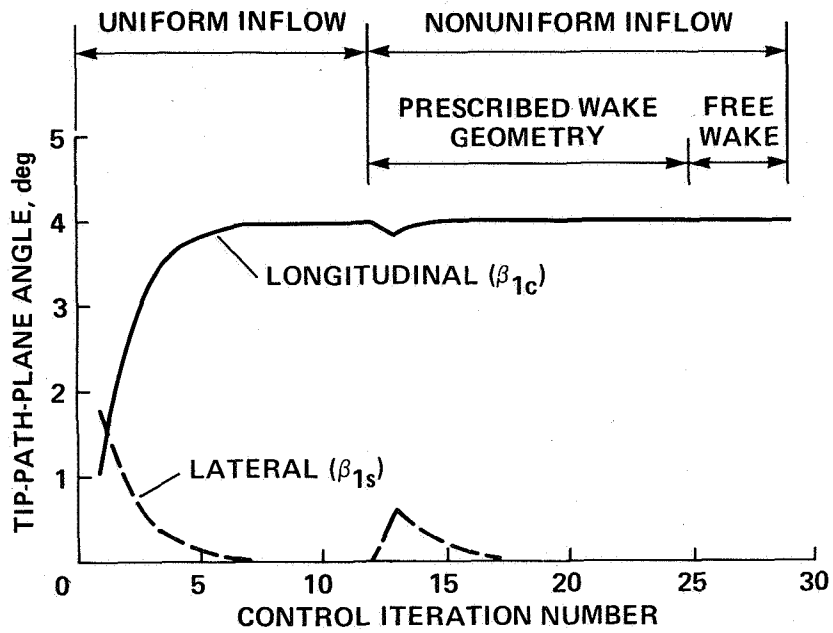


Figure 8.- Convergence of rotor blade position during typical trim iteration.

TRIM

TIMER

IF TRIM RESTART, GO TO RESTART ENTRY POINT

IF OPINTV = 1, CALL BODYI

UNIFORM INFLOW

IF ITERU≠0

IF OPINTV = 2, CALL BODYI

TRIMI

NONUNIFORM INFLOW, PRESCRIBED WAKE GEOMETRY
FOR IT = 1 TO ITERR

WAKEC1

WAKEC2

IF OPINTV = 2, CALL BODYI

TRIMI

NONUNIFORM INFLOW, FREE WAKE GEOMETRY
FOR IT = 1 TO ITERF

WAKEC1

WAKEC2

IF OPINTV = 2, CALL BODYI

TRIMI

•
•
•

(a) BODYI subroutine calls in TRIM.

Figure 9.- CAMRAD for program modifications.

RAMF

```
TIMER
IF OPINTV = 3, CALL BODYI
  •
  •
  •
FOR COUNTC = 1 TO ITERC (CIRCULATION ITERATION)
  IF OPINTV = 4, CALL BODYI
    •
    •
    •
FOR COUNTM = 1 TO ITERM (MOTION ITERATION)
  IF OPINTV = 5, CALL BODYI
    •
    •
    •
  TEST MOTION CONVERGENCE
  TEST CIRCULATION CONVERGENCE
BODYF
TIMER
```

(b) BODYI subroutine calls in RAMF.

Figure 9.- Continued.

PARAMETER	DESCRIPTION
FSBODY BLBODY WLBODY	(x, y, z) COORDINATES OF BODY NOSE RELATIVE TO THE HUB POSITION, NORMALIZED BY R
LENGTH	BODY LENGTH, l/R
THICK	BODY THICKNESS RATIO, $2t/l$ (FOR OPSHAP = 1-6 ONLY)
OPSHAP	INTEGER SPECIFYING BODY SHAPE: 1 – ELLIPSOID (EXACT SOLUTION) 2 – ELLIPSOID (MSBT) 3 – ELLIPSOID (SBT) 4 – NACA 00xx (MSBT WITH TAIL CORRECTION) 5 – NACA 00xx (MSBT) 6 – NACA 00xx (SBT) 7 – ROTOR TEST APPARATUS (MSBT WITH TAIL CORRECTION) 8 – EASTER EGG (MSBT WITH TAIL CORRECTION) -1 – READ VELOCITY FILE (RELATIVE TO BODY AXES, SCALED WITH V) -2 – READ VELOCITY FILE (RELATIVE TO SHAFT AXES, SCALED WITH ΩR)
NMSBT	NUMBER OF NUMERICAL INTEGRATION STEPS USED TO INTEGRATE EQUATION FOR BODY-INDUCED VELOCITY
OPINTV	INTEGER SPECIFYING WHEN BODY-INDUCED VELOCITIES ARE UPDATED: 0 – NOT CALCULATED AT ALL (NO BODY) 1 – ONCE PER CASE 2 – ONCE PER WAKE ITERATION 3 – ONCE PER CONTROL ITERATION 4 – ONCE PER CIRCULATION ITERATION 5 – ONCE PER MOTION ITERATION

(c) New input parameters in namelist NLBODY and new common block INTAER (blade position calculation also uses OPWKBP parameter from namelist NLWAKE).

Figure 9.- Continued.

MODIFIED SUBROUTINES

SUBROUTINE	MODIFICATIONS
INPTB	INCLUSION OF NEW PARAMETERS IN NAMELIST NLBODY
PRNTB	NEW INPUT PARAMETERS PRINTED
TRIM	CALLS BODYI
RAMF	CALLS BODYI
LOADR1	POLAR PLOT INCREMENTS
TIMER	NEW TIME SUMMARIES

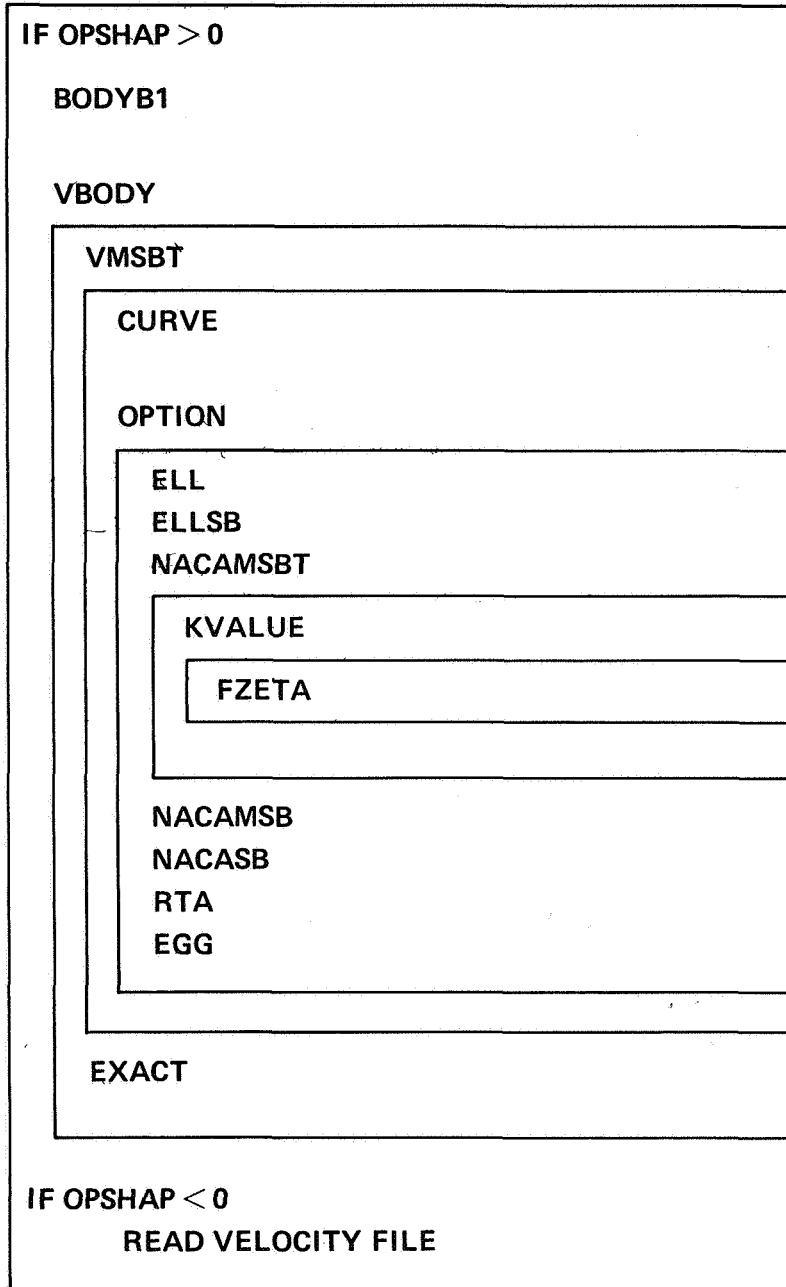
NEW SUBROUTINES

SUBROUTINE	DESCRIPTION
BODYI	CALCULATES BODY-INDUCED VELOCITIES OVER ROTOR DISK
BODYB1	CALCULATES BLADE POSITION (IN SHAFT AXES) AT AERODYNAMIC STATIONS; DERIVED FROM SUBROUTINE WAKEB1
VBODY	CALCULATES BODY-INDUCED VELOCITY
EXACT	CALCULATES FLOW ABOUT ELLIPSOID – EXACT SOLUTION
VMSBT	INTEGRATES VELOCITY EQUATION
CURVE	CALCULATES BODY NOSE/TAIL RADIUS OF CURVATURE
OPTION	SELECTS BODY SHAPE
ELL	ELLIPSOID – USES MSBT
ELLSB	ELLIPSOID – USED SBT
NACAMSBT	NACA 00xx–USES MSBT WITH TAIL CORRECTION
KVALUE	CALCULATES VALUE OF KN FOR NACA 00xx
FZETA	CALCULATES PARTS OF INTEGRAND FOR INTEGRATION IN KVALUE
NACAMSB	NACA 00xx–USES MSBT
NACASB	NACA 00xx–USES SBT
RTA	ROTOR TEST APPARATUS – USES MSBT WITH TAIL CORRECTION
EGG	EASTER EGG – USES MSBT WITH TAIL CORRECTION

(d) List of new and modified subroutines.

Figure 9.- Continued.

BODYI



(e) Skeleton of BODYI subroutine (called by TRIM and RAMF).

Figure 9.- Concluded.

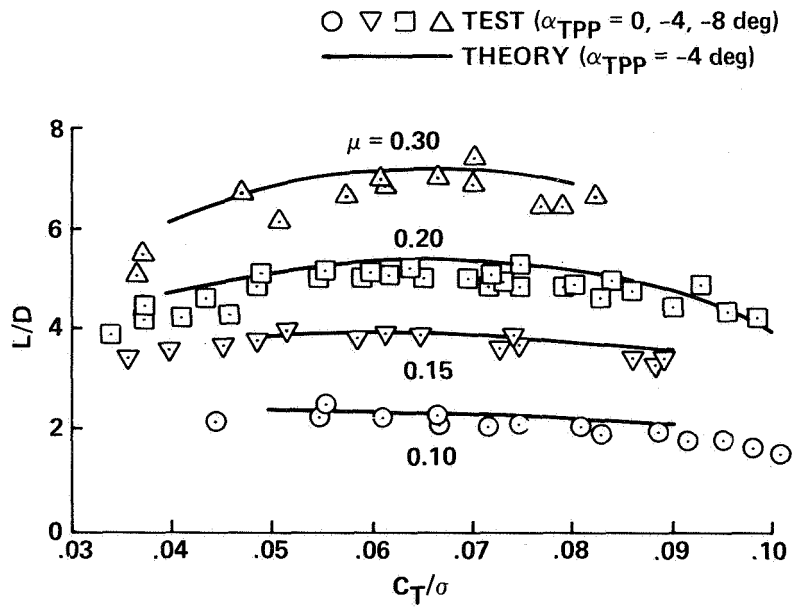


Figure 10.- Isolated rotor performance for rotor A.

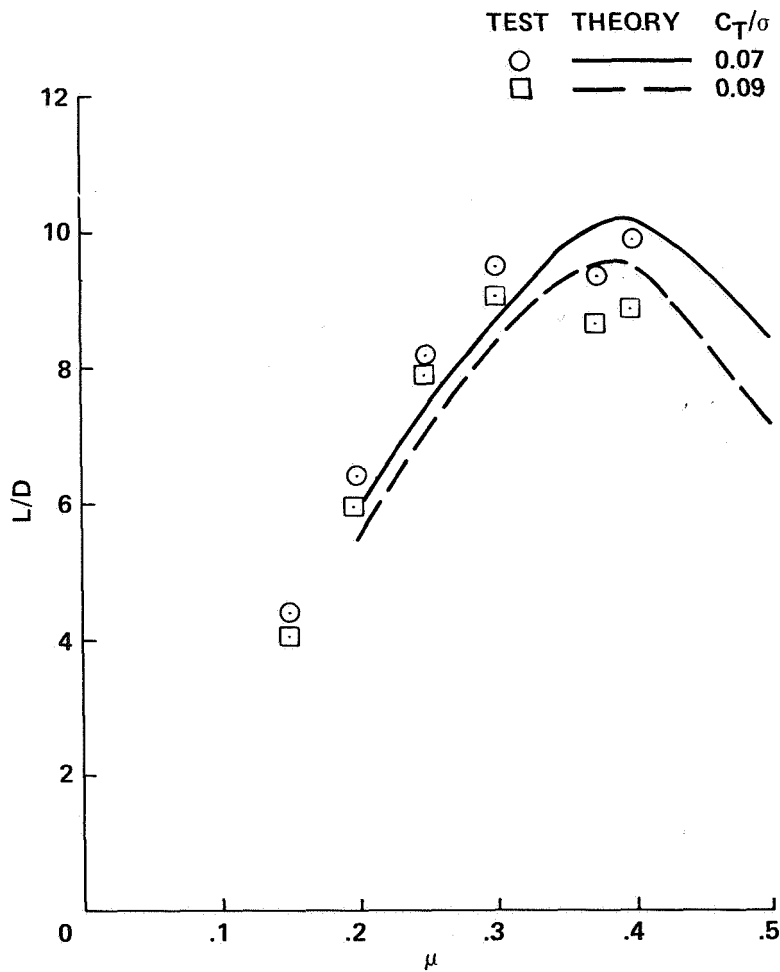


Figure 11.- Performance for rotor B with RTA ($\alpha_{TPP} = 0$).

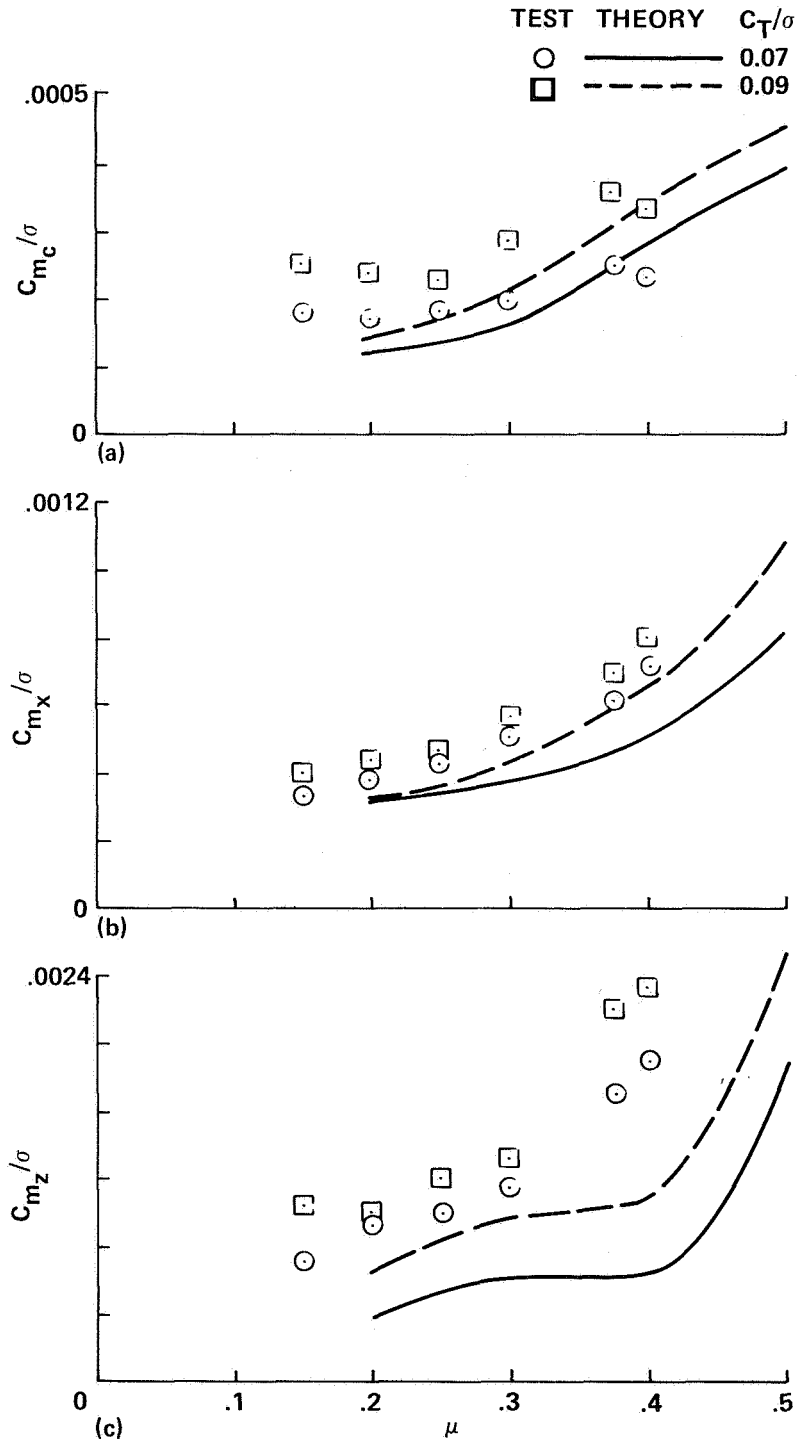


Figure 12.- Oscillatory blade loads for rotor B with RTA ($\alpha_{TPP} = 0$). (a) Control moment; (b) flapping bending moment at 0.7R; (c) edgewise bending moment at 0.6R.

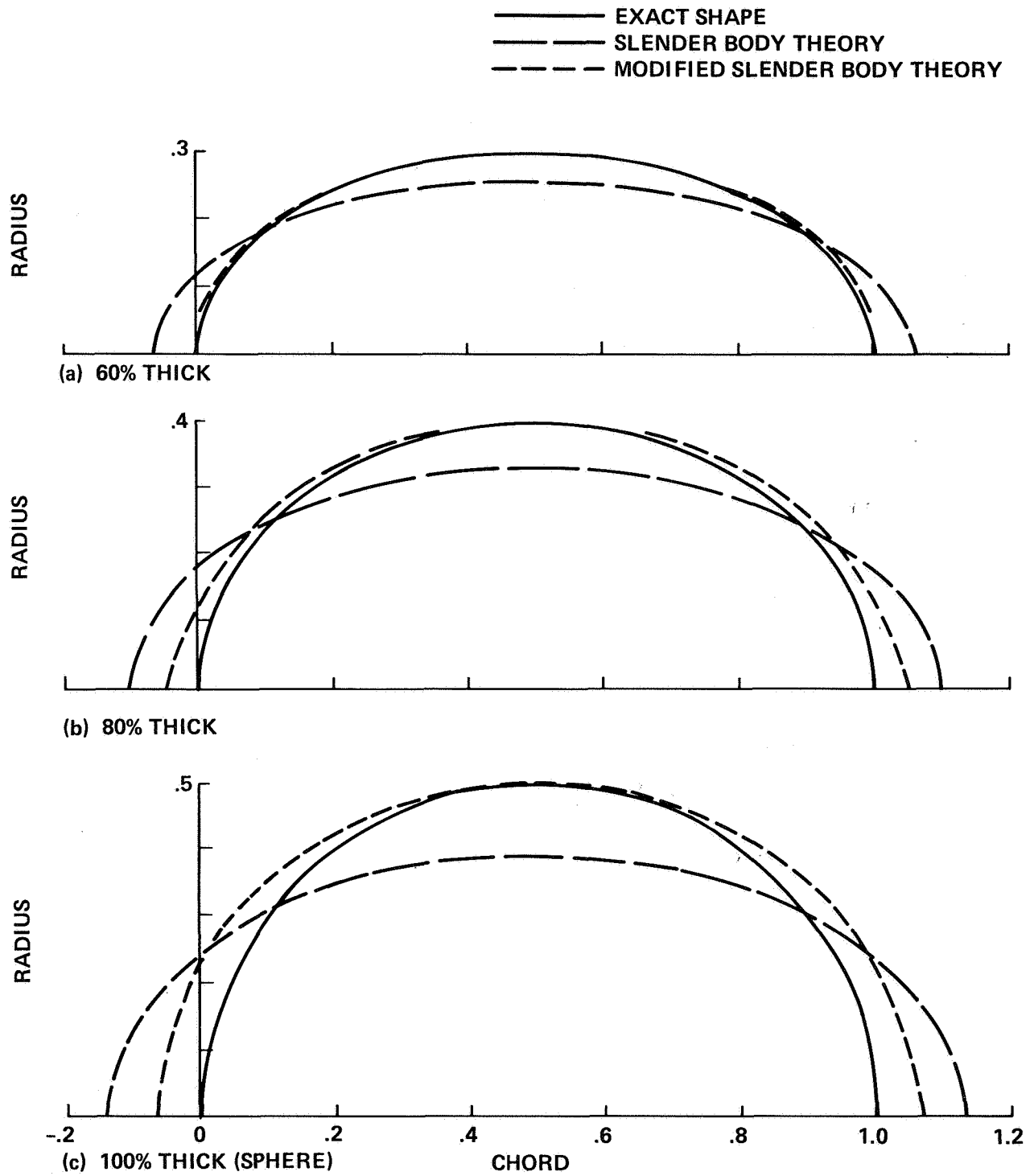
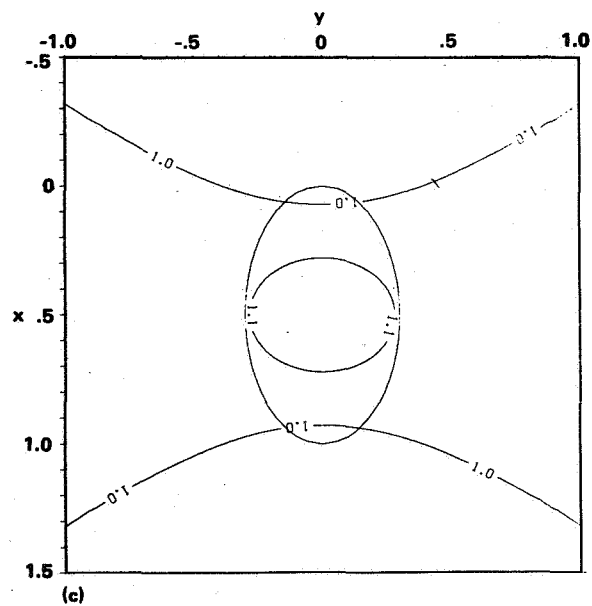
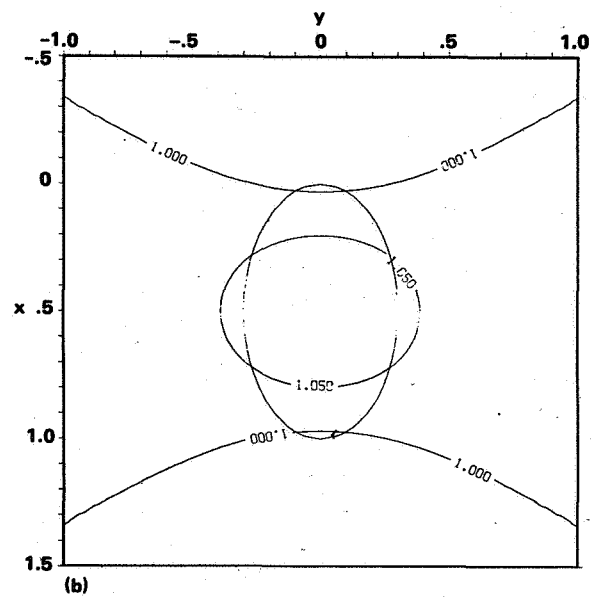
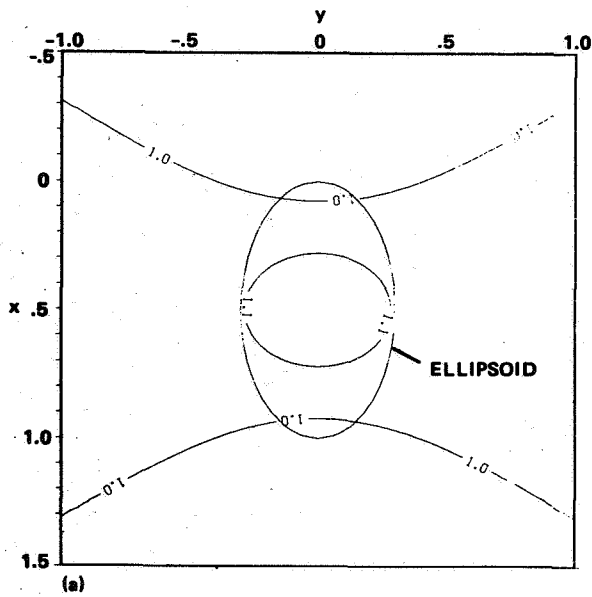


Figure 13.- Body streamlines for ellipsoids, comparing exact, slender body, and modified slender body theories. (a) 60%-thick ellipsoid; (b) 80%-thick ellipsoid; (c) 100%-thick ellipsoid.




**FORWARD
SPEED**

Figure 14.- Plot of velocity magnitude divided by free stream velocity in plane above body - 60% ellipsoid. (a) Exact theory; (b) slender body theory; (c) modified slender body theory.

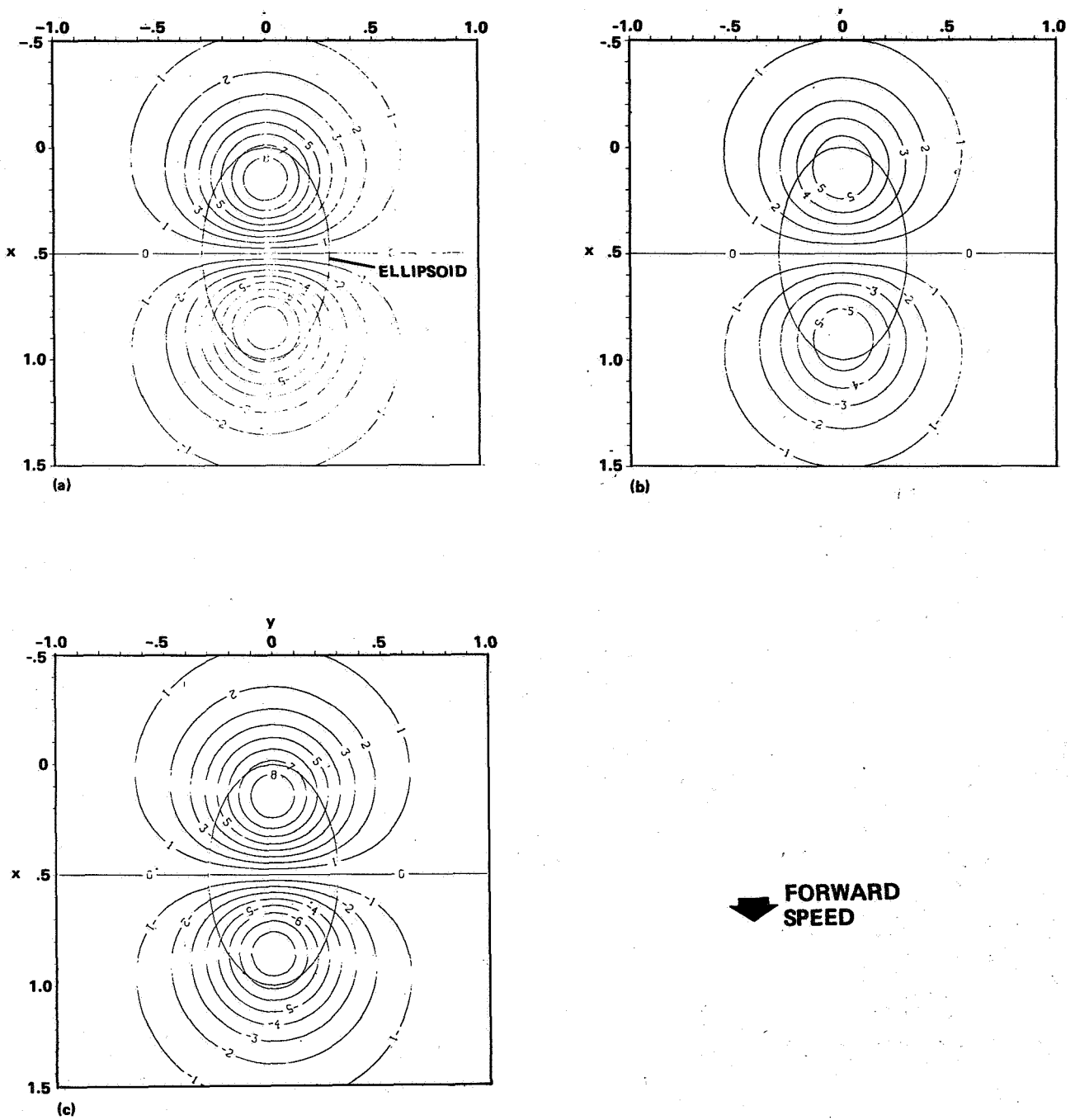
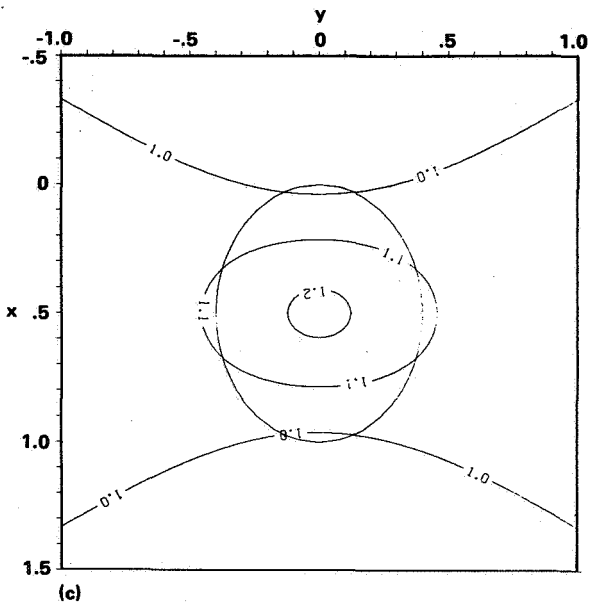
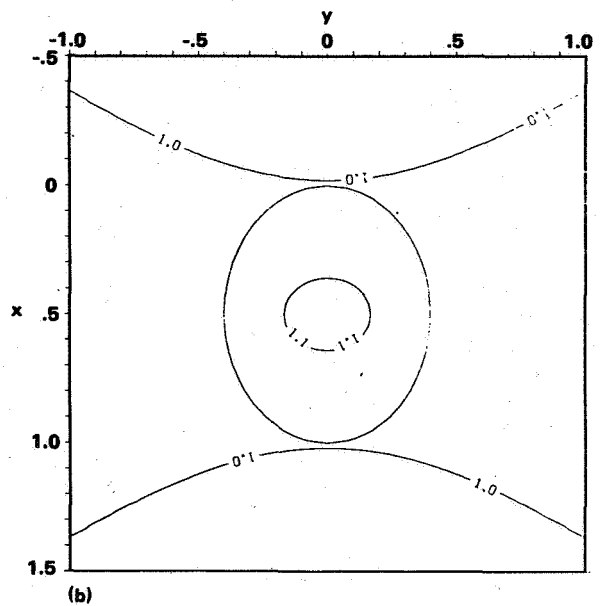
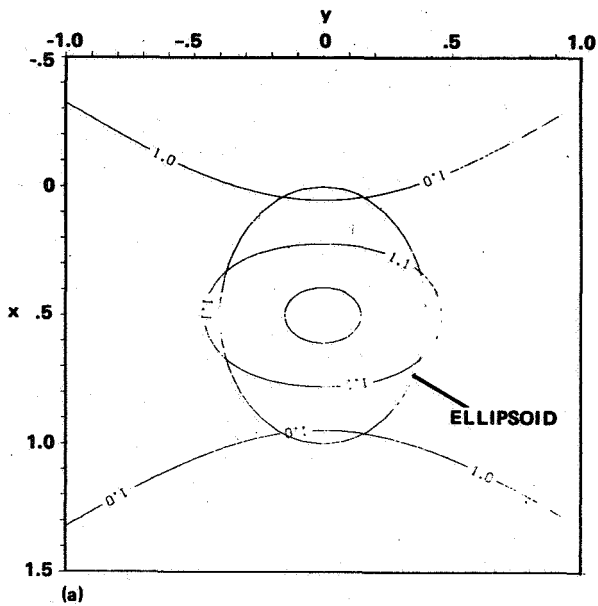
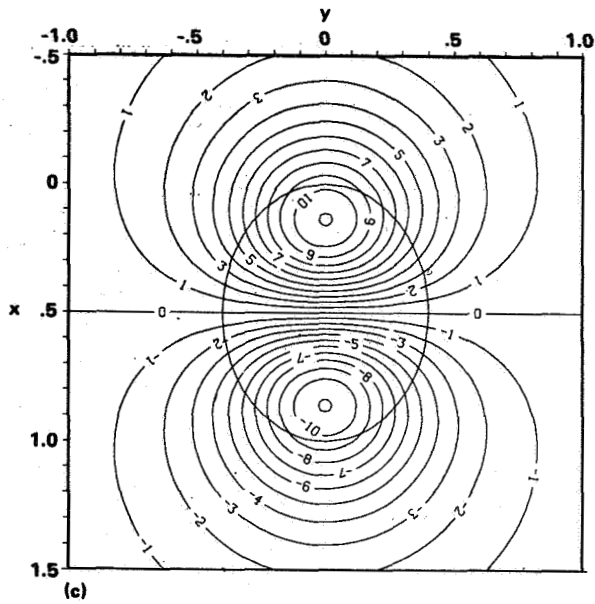
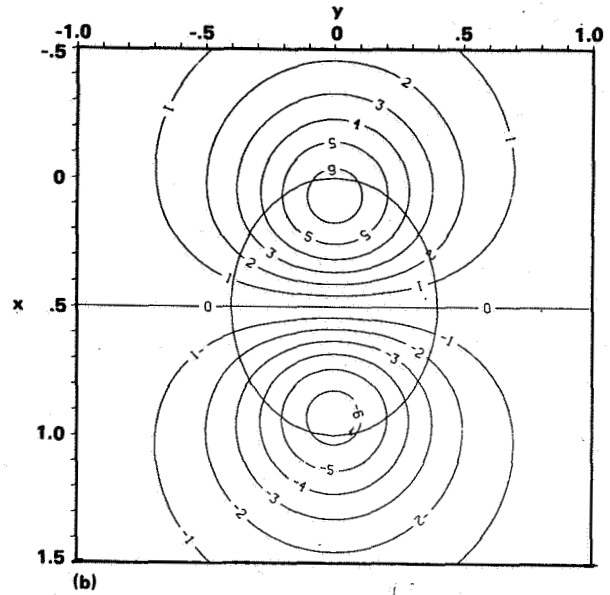
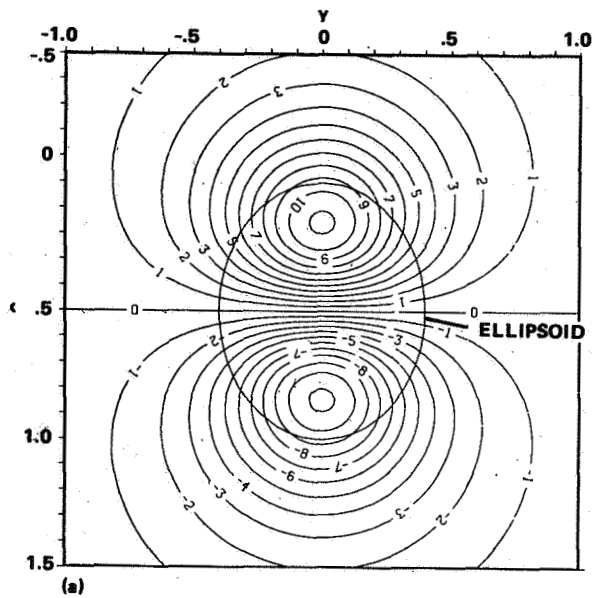


Figure 15.- Plot of angle of attack (deg) in plane above body — 60%-thick ellipsoid
 (a) Exact theory; (b) slender body theory; (c) modified slender body theory.



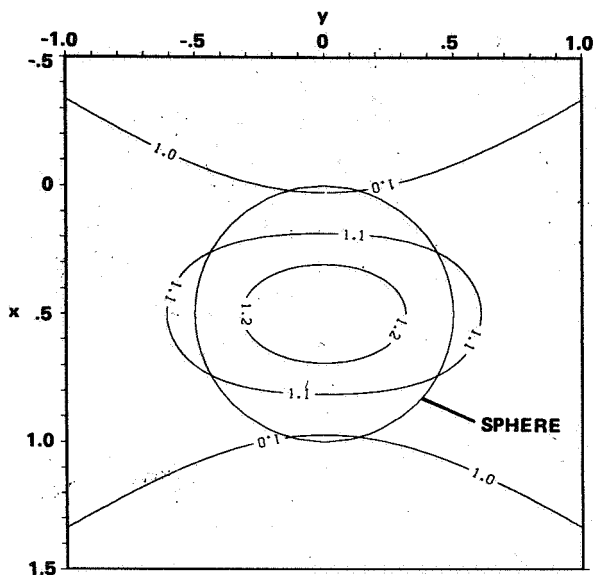

FORWARD SPEED

Figure 16.- Plot of velocity magnitude divided by free stream velocity in plane above body - 80%-thick ellipsoid. (a) Exact theory; (b) slender body theory; (c) modified slender body theory.

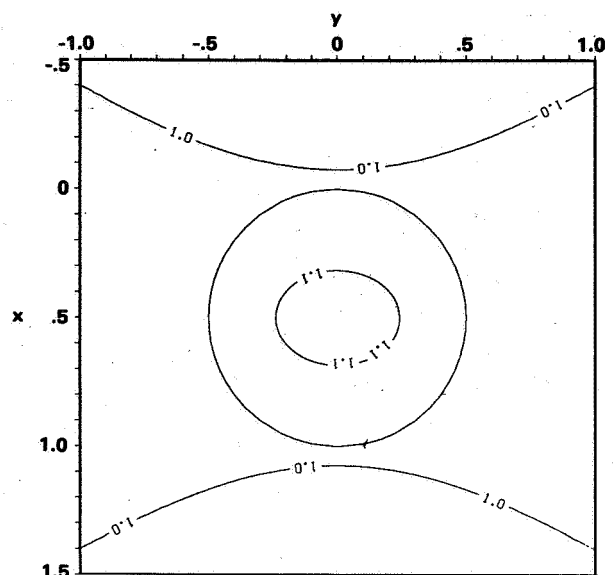



**FORWARD
SPEED**

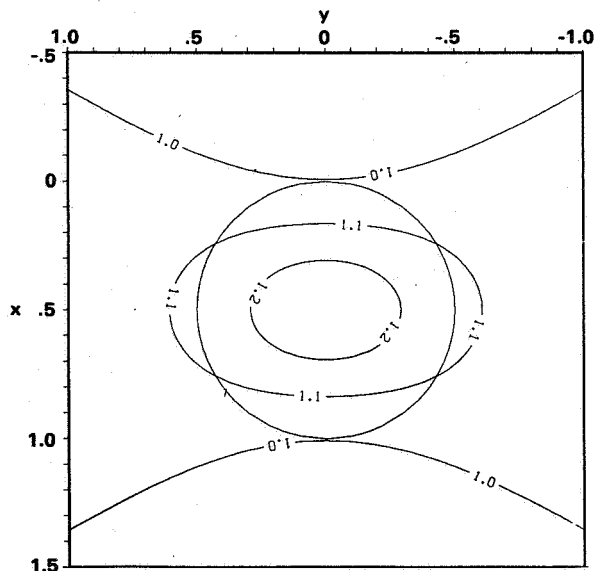
Figure 17.- Plot of angle of attack (deg) in plane above body - 80%-thick ellipsoid.
 (a) Exact theory; (b) slender body theory; (c) modified slender body theory.



(a)



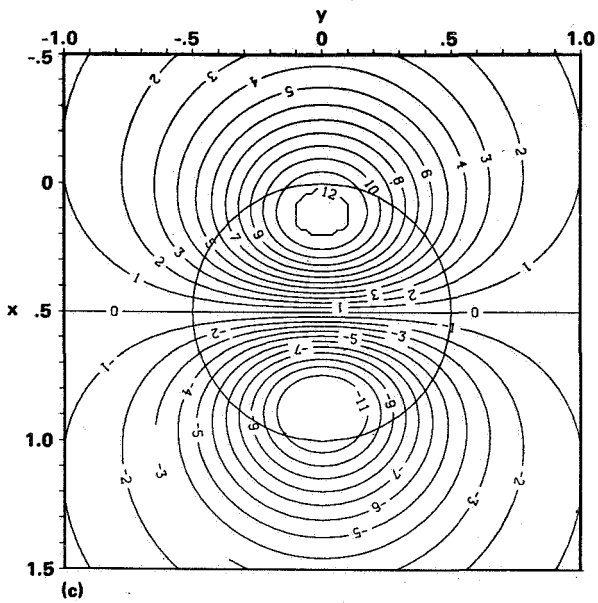
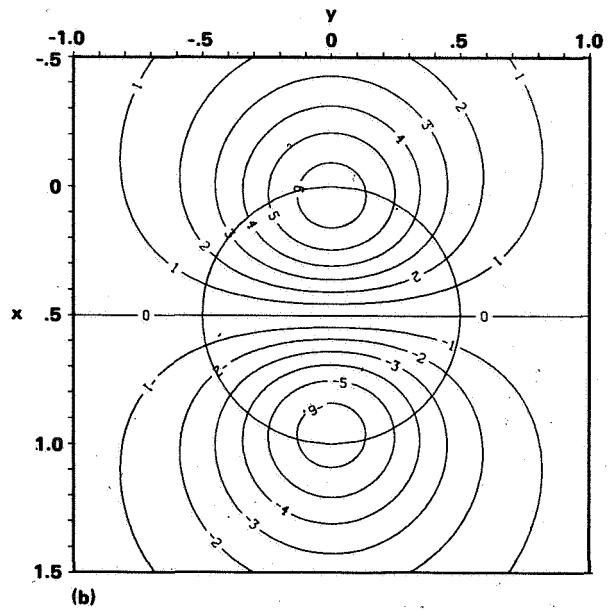
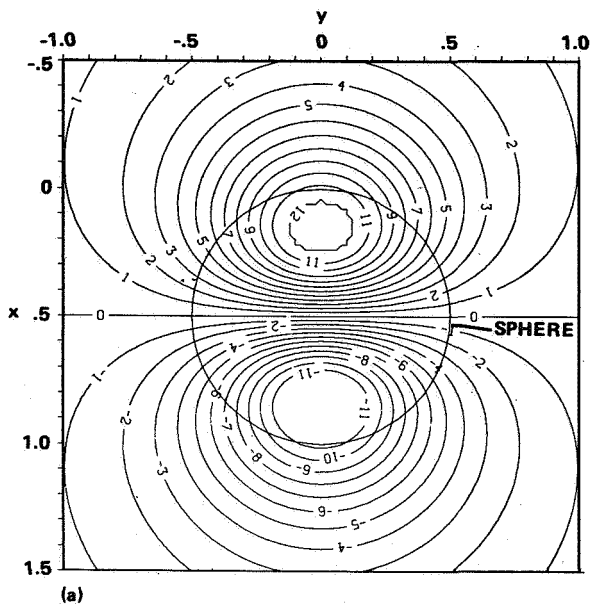
(b)



(c)

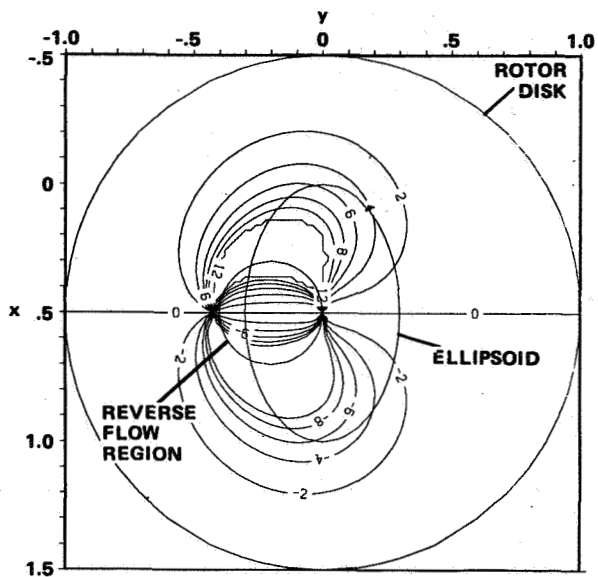

**FORWARD
SPEED**

Figure 18.- Plot of velocity magnitude divided by free stream velocity in plane above body - 100%-thick ellipsoid (sphere). (a) Exact theory; (b) slender body theory; (c) modified slender body theory.

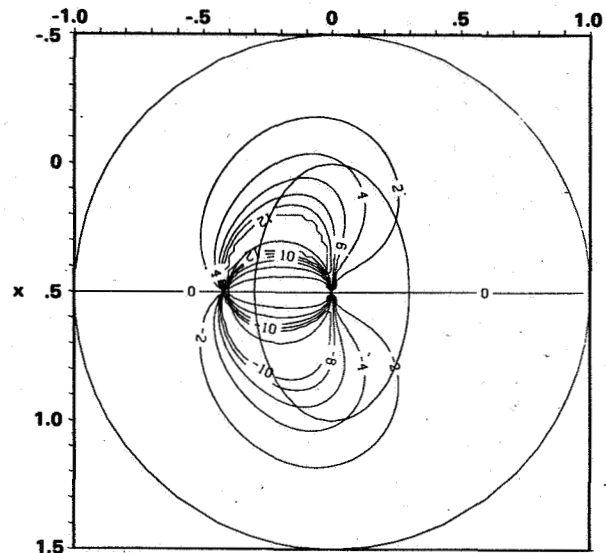



FORWARD SPEED

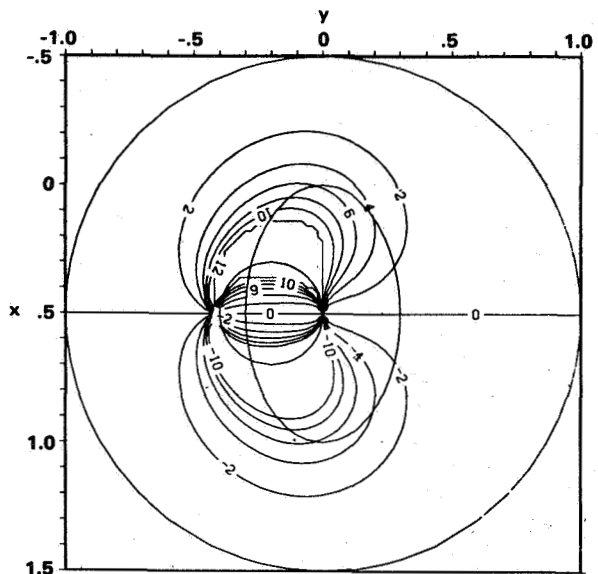
Figure 19.- Plot of angle of attack (deg) in plane above body — 100%-thick ellipsoid (sphere). (a) Exact theory; (b) slender body theory; (c) modified slender body theory.



(a)



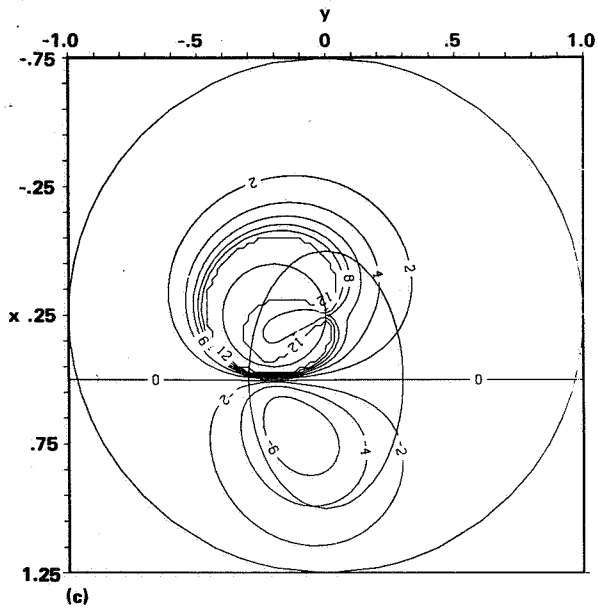
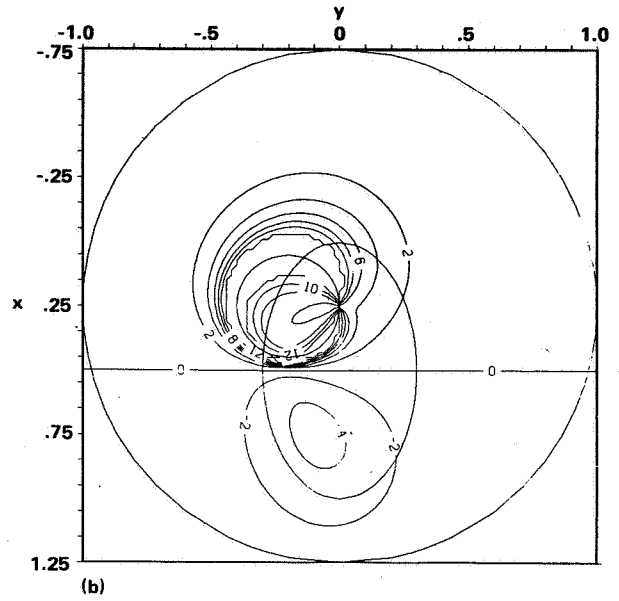
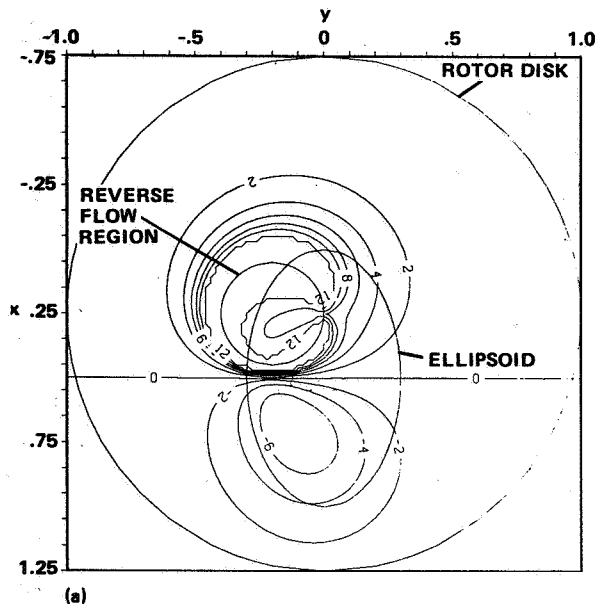
(b)



(c)

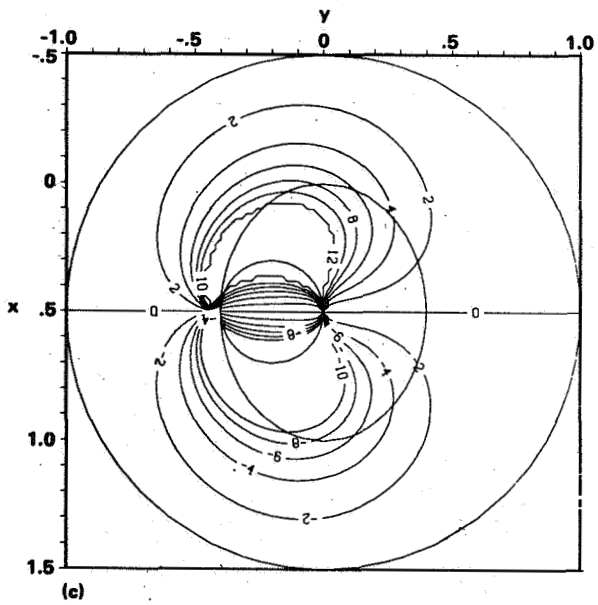
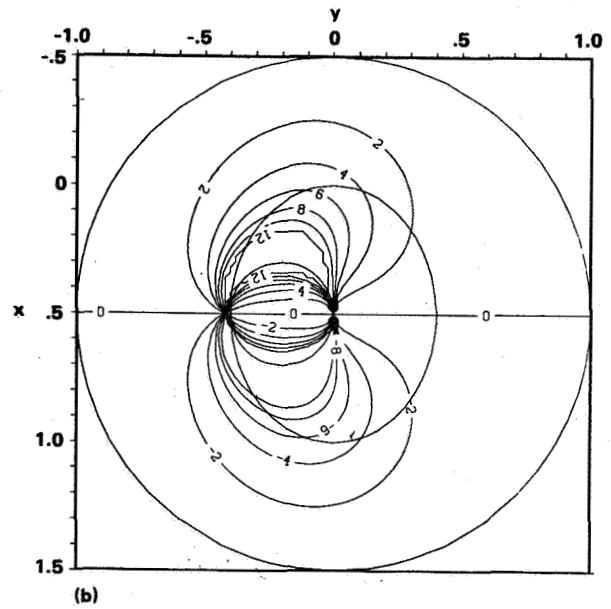
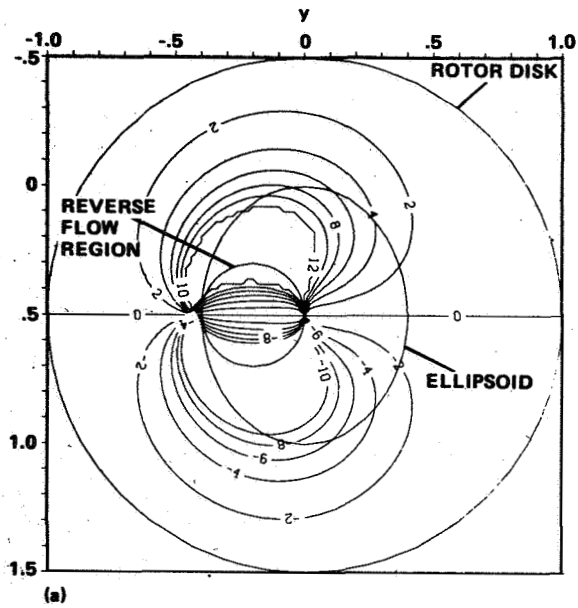

FORWARD SPEED

Figure 20.- Plot of rotor blade angle of attack change (deg) due to a 60%-thick ellipsoid in plane of rotor disk - hub position above body mid-chord, $\mu = 0.4$. (a) Exact theory; (b) slender body theory; (c) modified slender body theory.



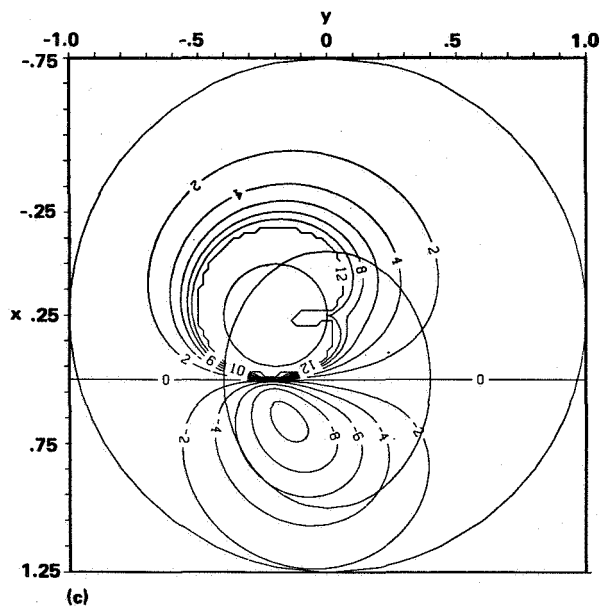
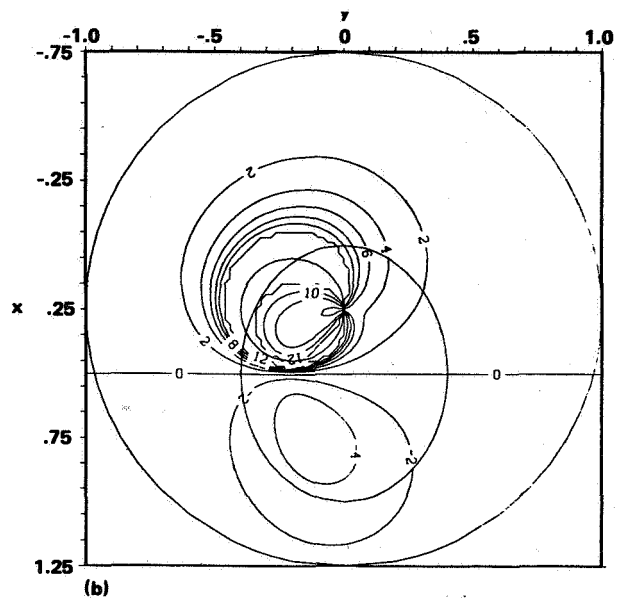
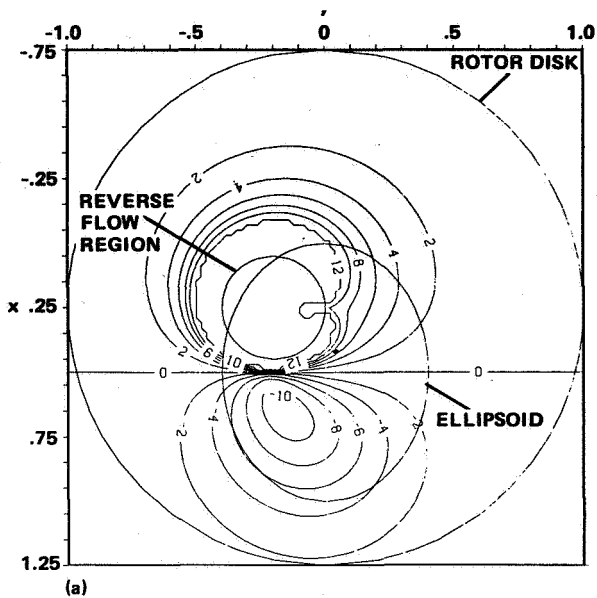

FORWARD SPEED

Figure 21.- Plot of rotor blade angle of attack change (deg) due to a 60%-thick ellipsoid in plane of rotor disk — hub position above body quarter-chord, $\mu = 0.4$.
 (a) Exact theory; (b) slender body theory; (c) modified slender body theory.



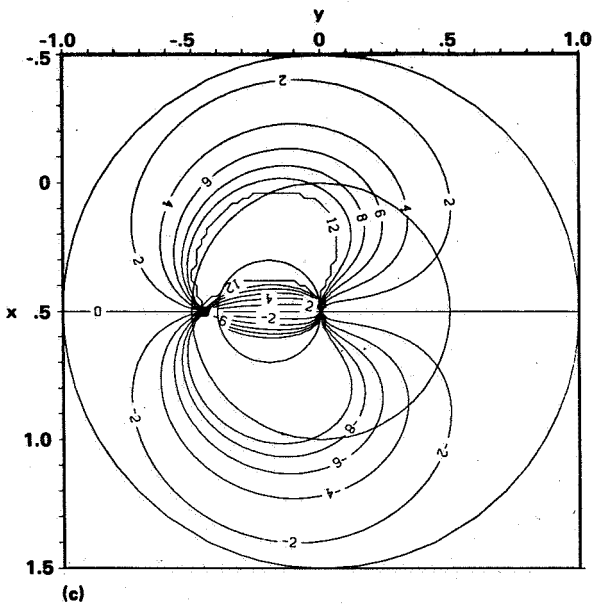
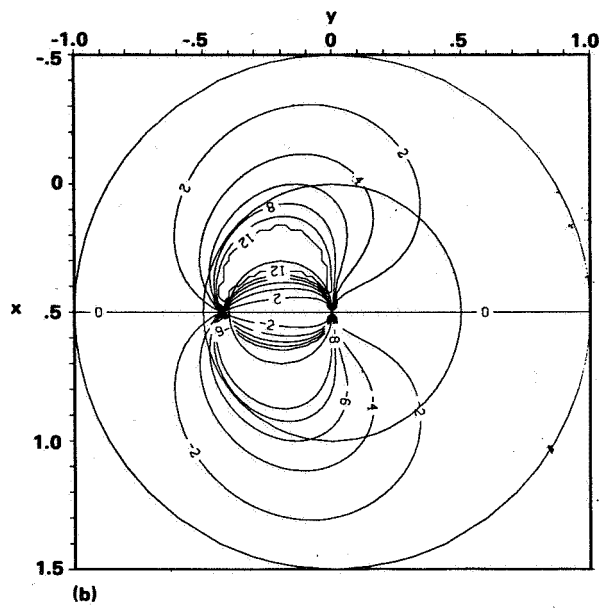
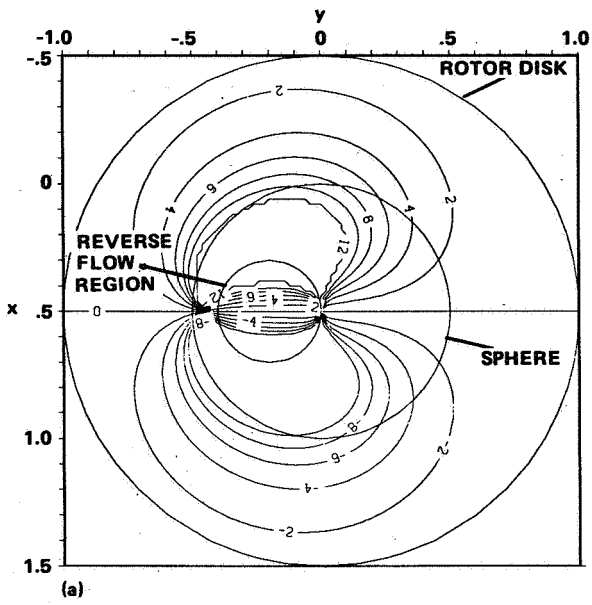
FORWARD SPEED

Figure 22.- Plot of rotor blade angle of attack change (deg) due to an 80%-thick ellipsoid in plane of rotor disk - hub position above body mid-chord, $\mu = 0.4$.
 (a) Exact theory; (b) slender body theory; (c) modified slender body theory.



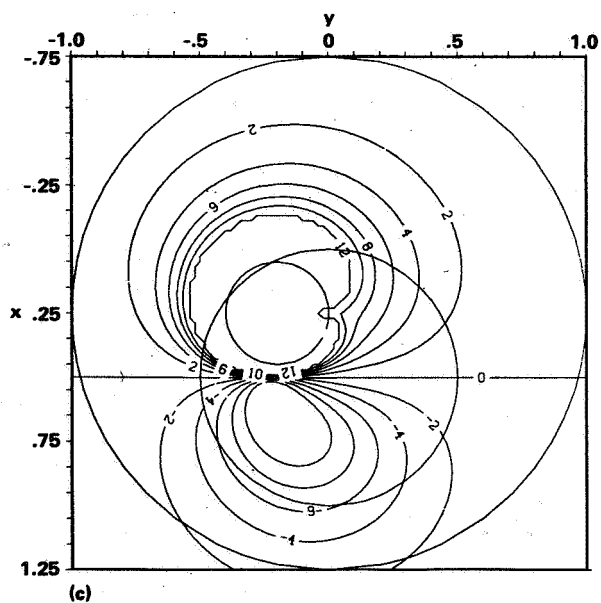
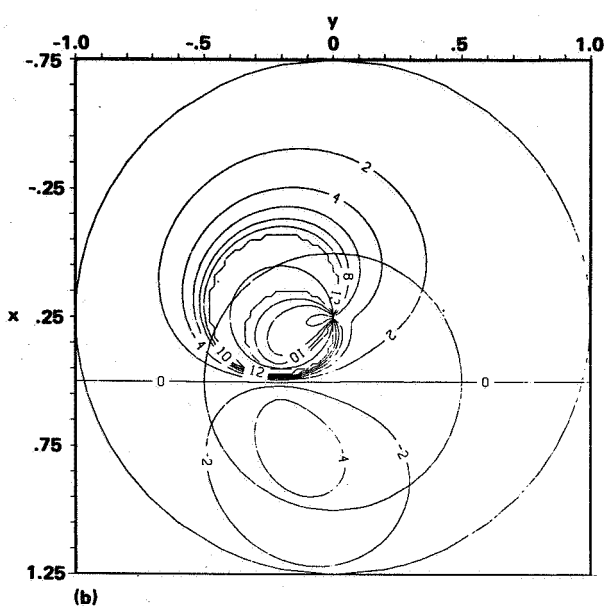
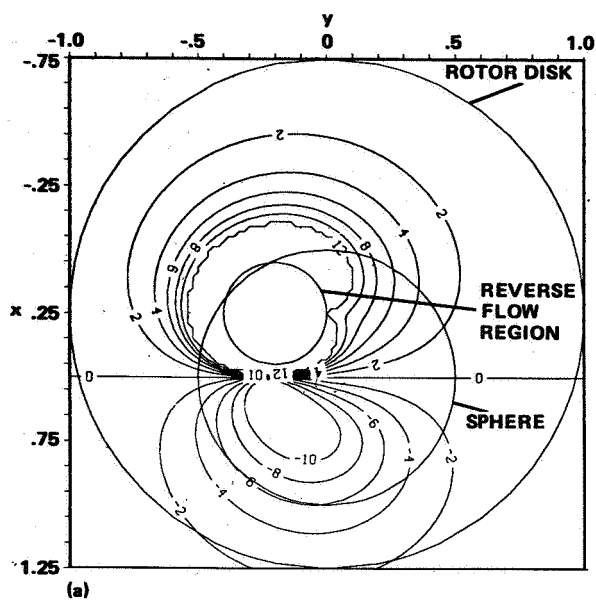

FORWARD SPEED

Figure 23.- Plot of rotor blade angle of attack change (deg) due to an 80%-thick ellipsoid in plane of rotor disk - hub position above body quarter-chord, $\mu = 0.4$.
 (a) Exact theory; (b) slender body theory; (c) modified slender body theory.



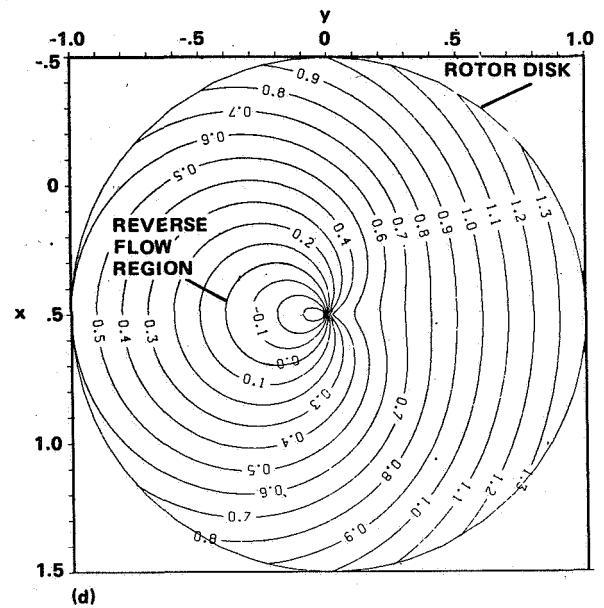
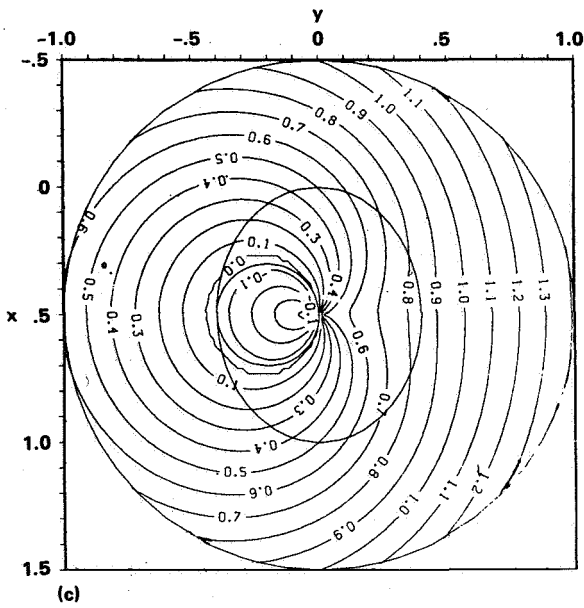
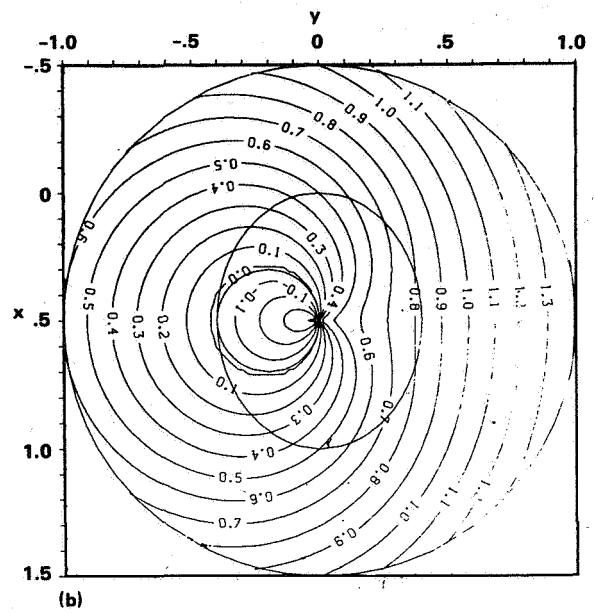
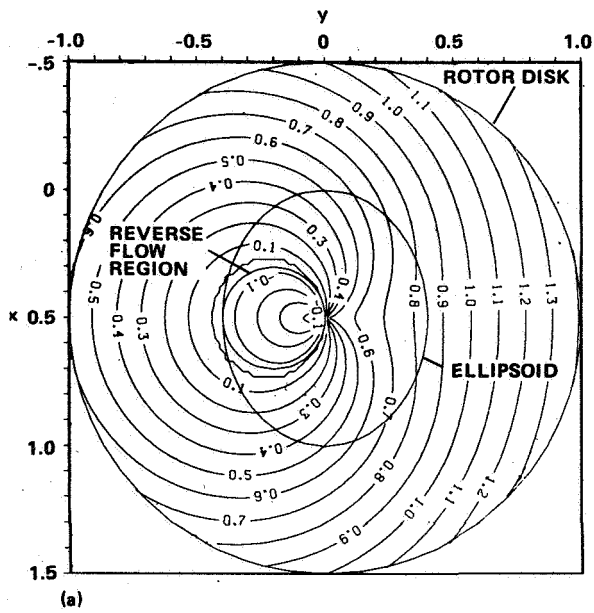

FORWARD SPEED

Figure 24.- Plot of rotor blade angle of attack change (deg) due to a 100%-thick ellipsoid in plane of rotor disk — hub position above body mid-chord, $\mu = 0.4$.
 (a) Exact theory; (b) slender body theory; (c) modified slender body theory.



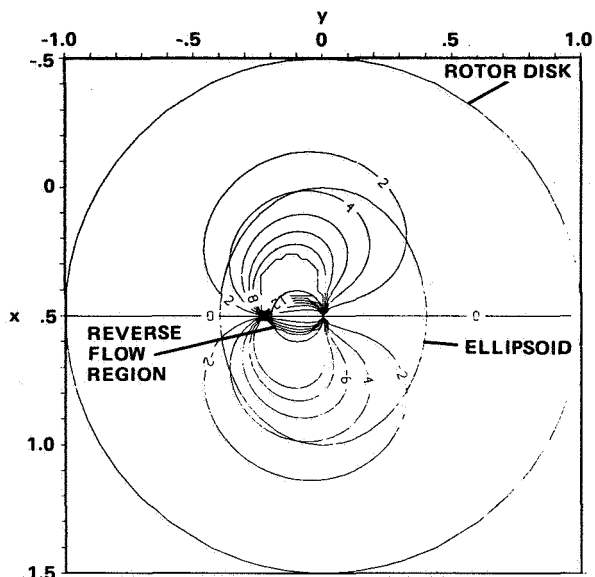

FORWARD SPEED

Figure 25.- Plot of rotor blade angle of attack change (deg) due to a 100%-thick ellipsoid in plane of rotor disk - hub position above body quarter-chord, $\mu = 0.4$.
 (a) Exact theory; (b) slender body theory; (c) modified slender body theory.

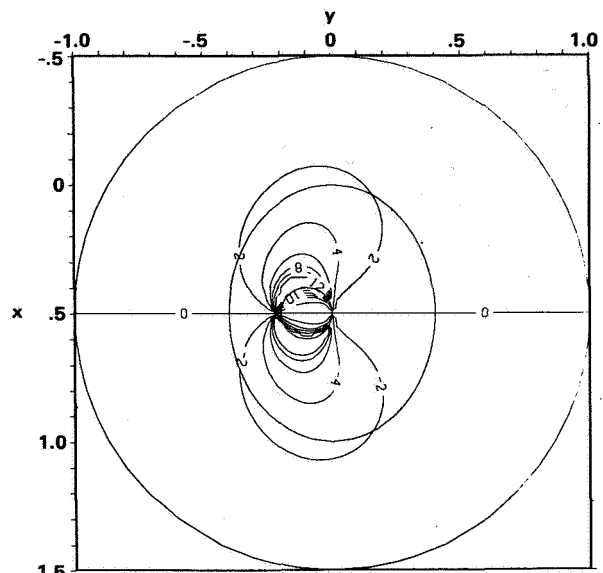


FORWARD SPEED

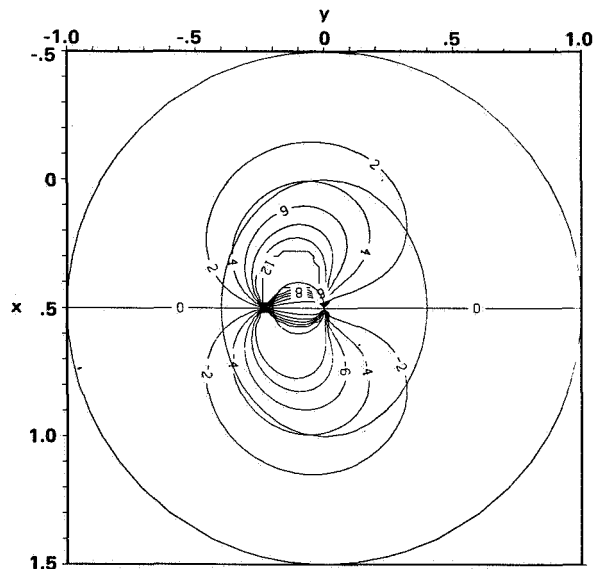
Figure 26.- Plot of rotor blade velocity magnitude (divided by tip speed) due to an 80%-thick ellipsoid - hub position above body mid-chord, $\mu = 0.4$. (a) Exact theory; (b) slender body theory; (c) modified slender body theory; (c) isolated rotor.



(a)



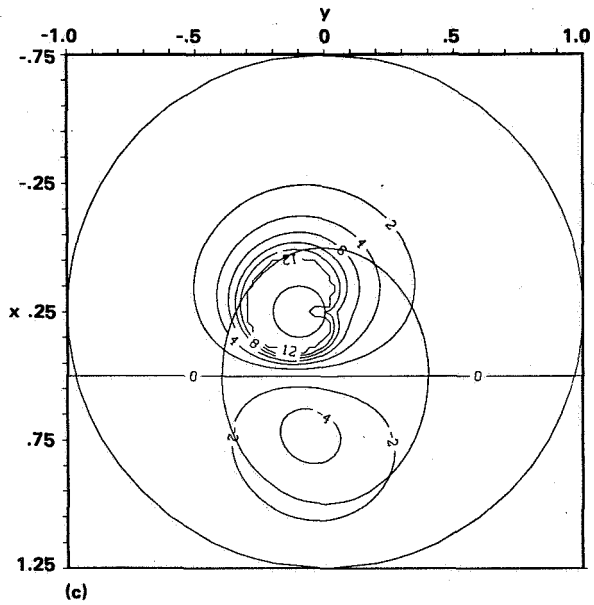
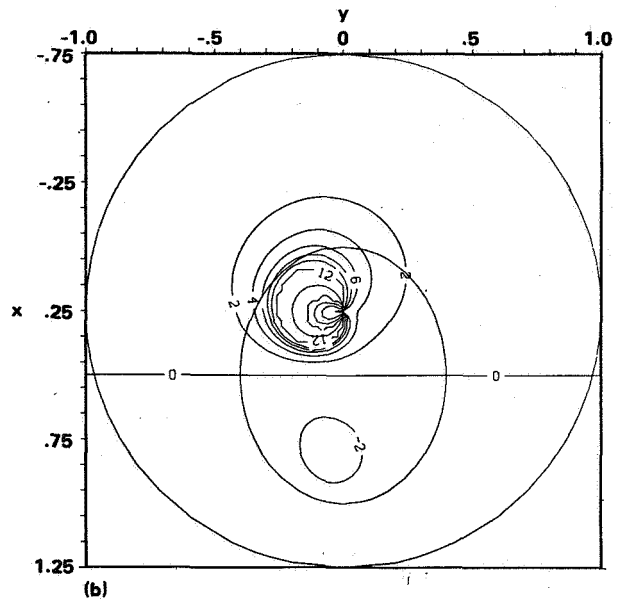
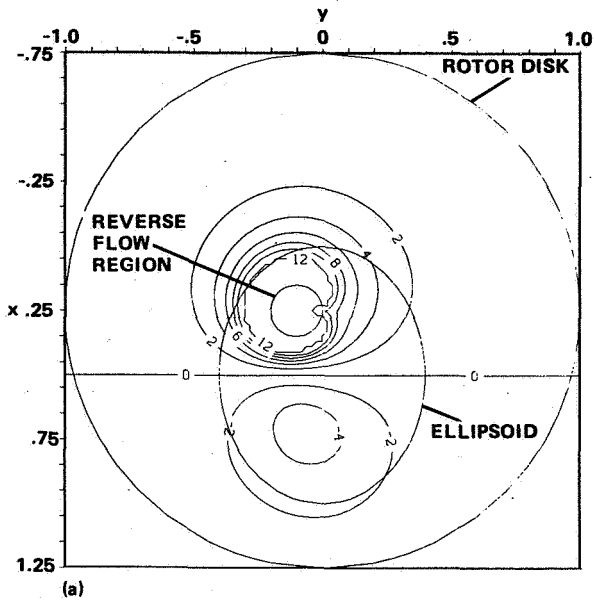
(b)



(c)


FORWARD SPEED

Figure 27.- Plot of rotor blade angle of attack change (deg) due to an 80%-thick ellipsoid in plane of rotor disk — hub position above body mid-chord, $\mu = 0.2$.
 (a) Exact theory; (b) slender body theory; (c) modified slender body theory.




FORWARD SPEED

Figure 28.- Plot of rotor blade angle of attack change (deg) due to an 80%-thick ellipsoid in plane of rotor disk - hub position above body quarter-chord, $\mu = 0.2$.
 (a) Exact theory; (b) slender body theory; (c) modified slender body theory.

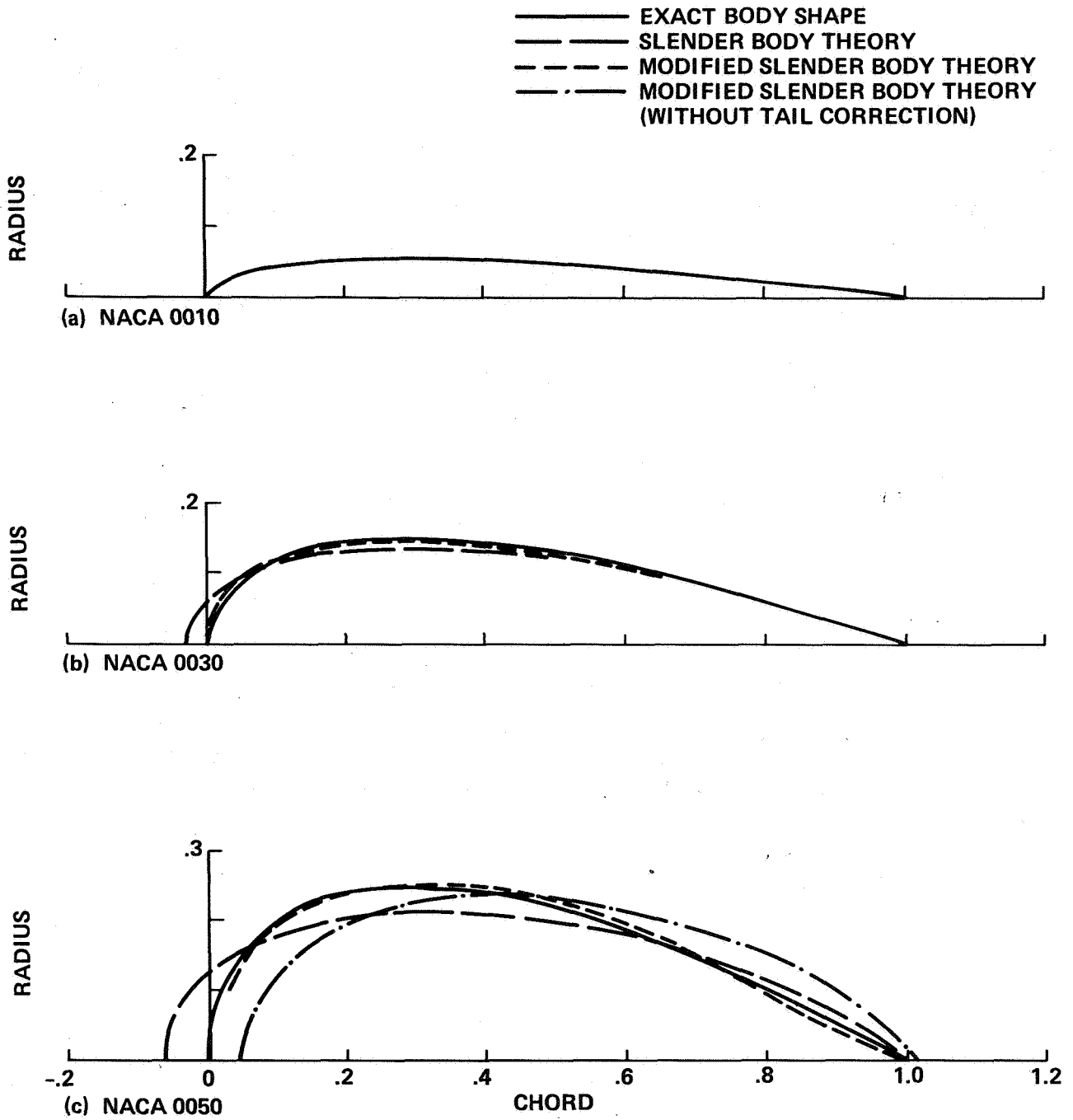
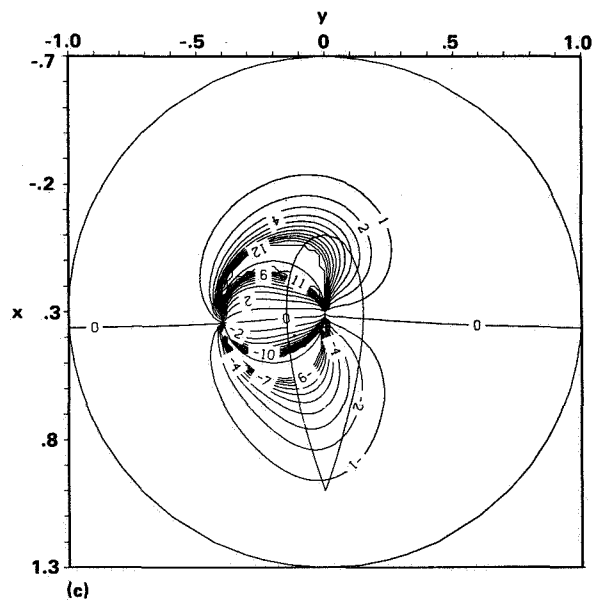
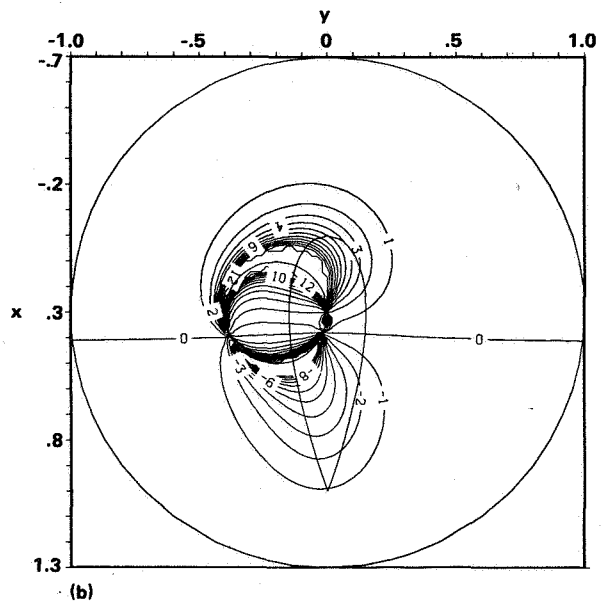
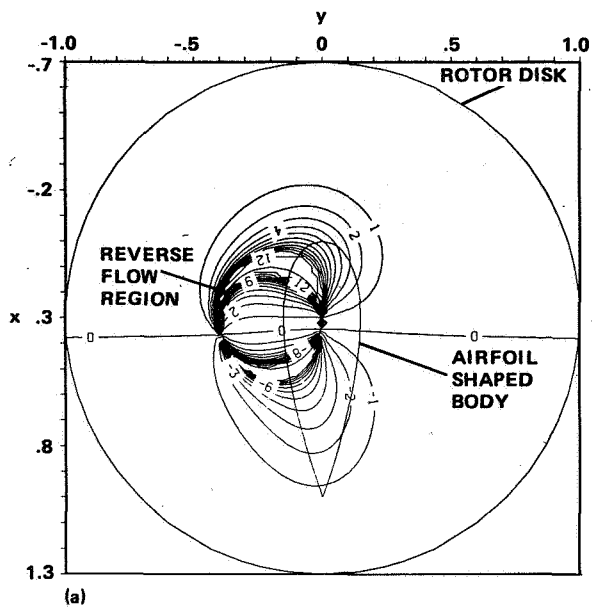
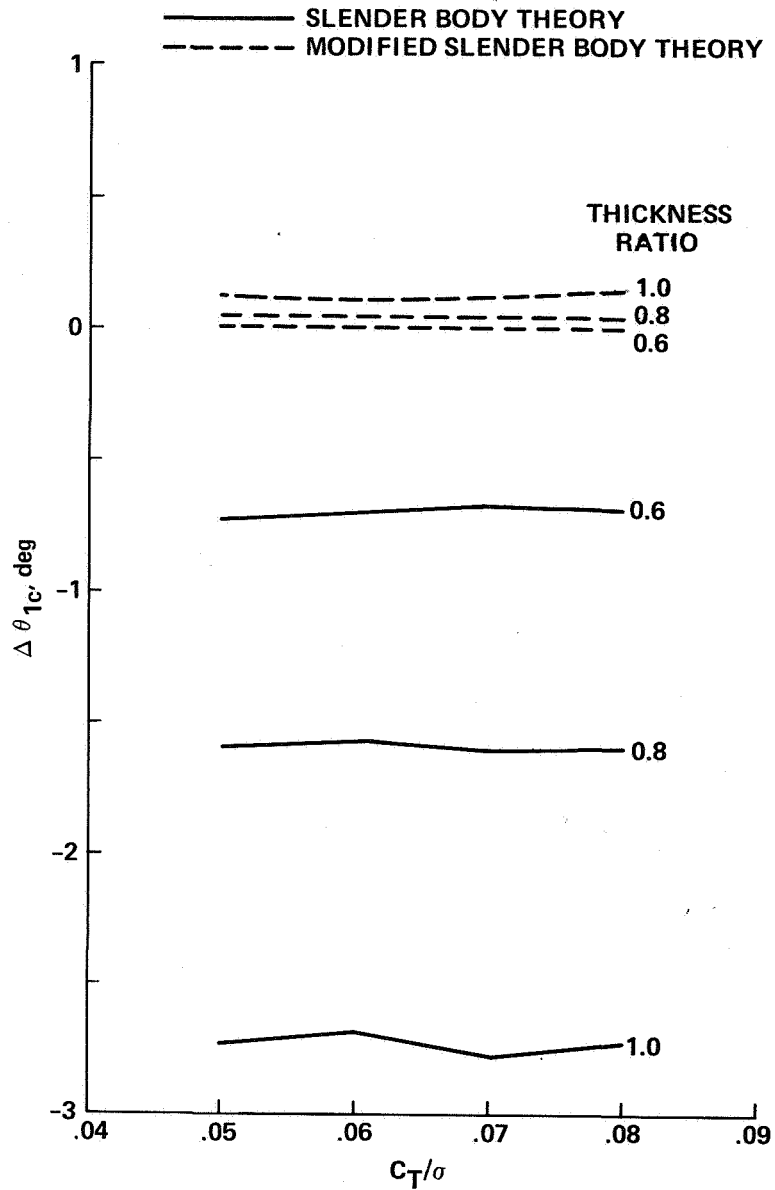


Figure 29.- Body streamlines for axisymmetric bodies with NACA 4-digit airfoil thickness distribution. (a) NACA 0010; (b) NACA 0030; (c) NACA 0050.



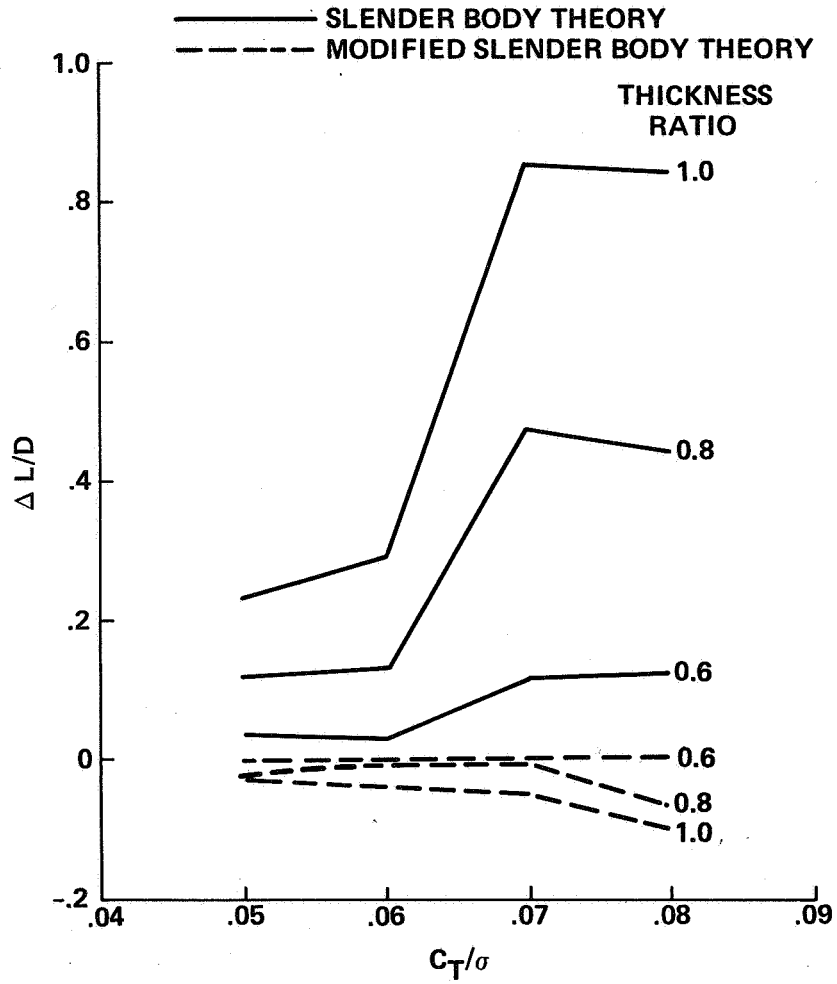

FORWARD SPEED

Figure 30.- Plot of rotor blade angle of attack change (deg) due to a 30%-thick airfoil shaped body in plane of rotor disk, $\mu = 0.4$. (a) Slender body theory; (b) modified slender body theory; (c) modified slender body theory with tail correction.



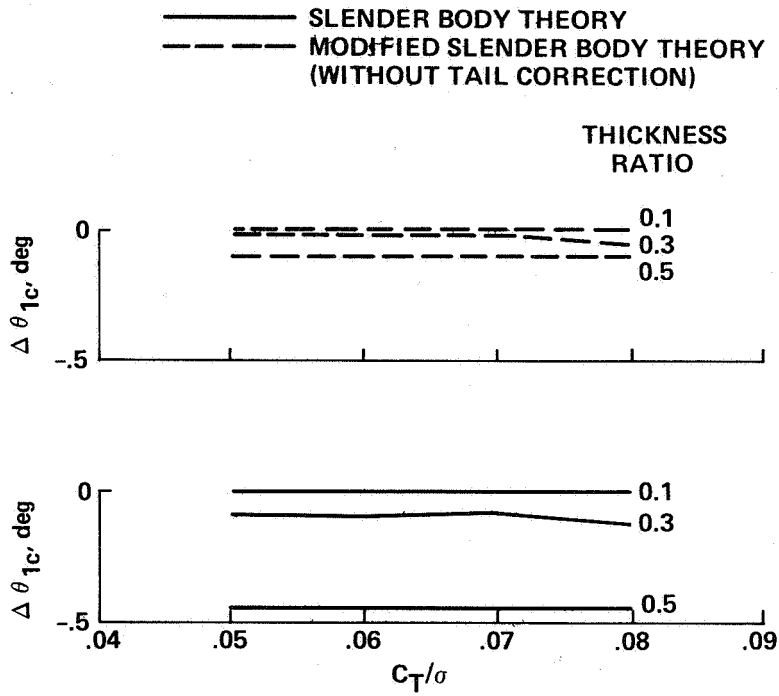
(a) Lateral cyclic control angle (deg).

Figure 31.- Error in lateral cyclic control angle (deg) and lift-to-drag ratio for rotor A in combination with ellipsoids of various thicknesses (case 1).



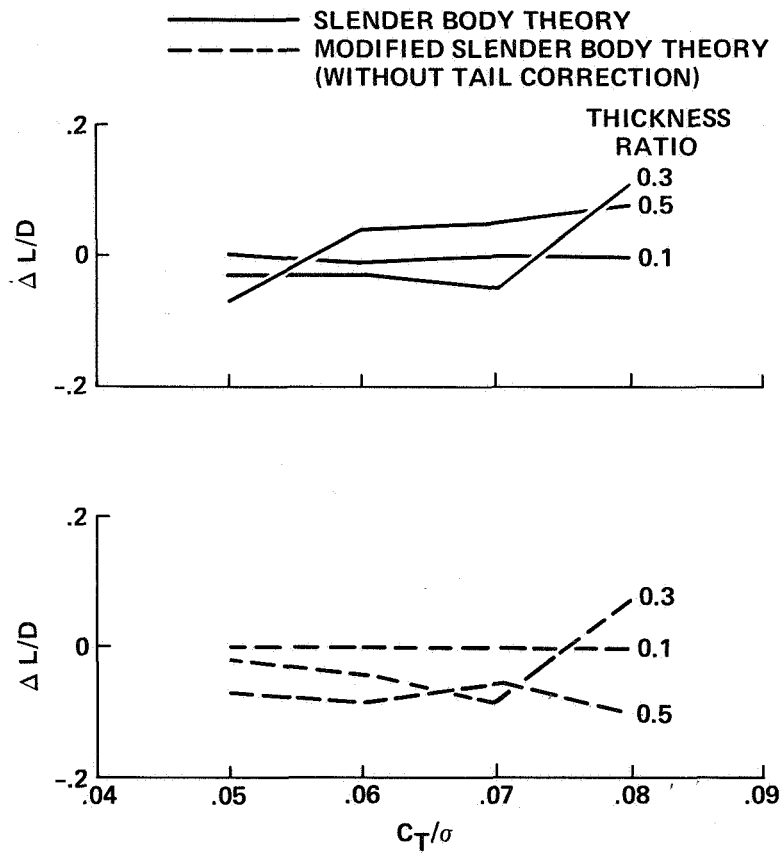
(b) Lift-to-drag ratio.

Figure 31.- Concluded.



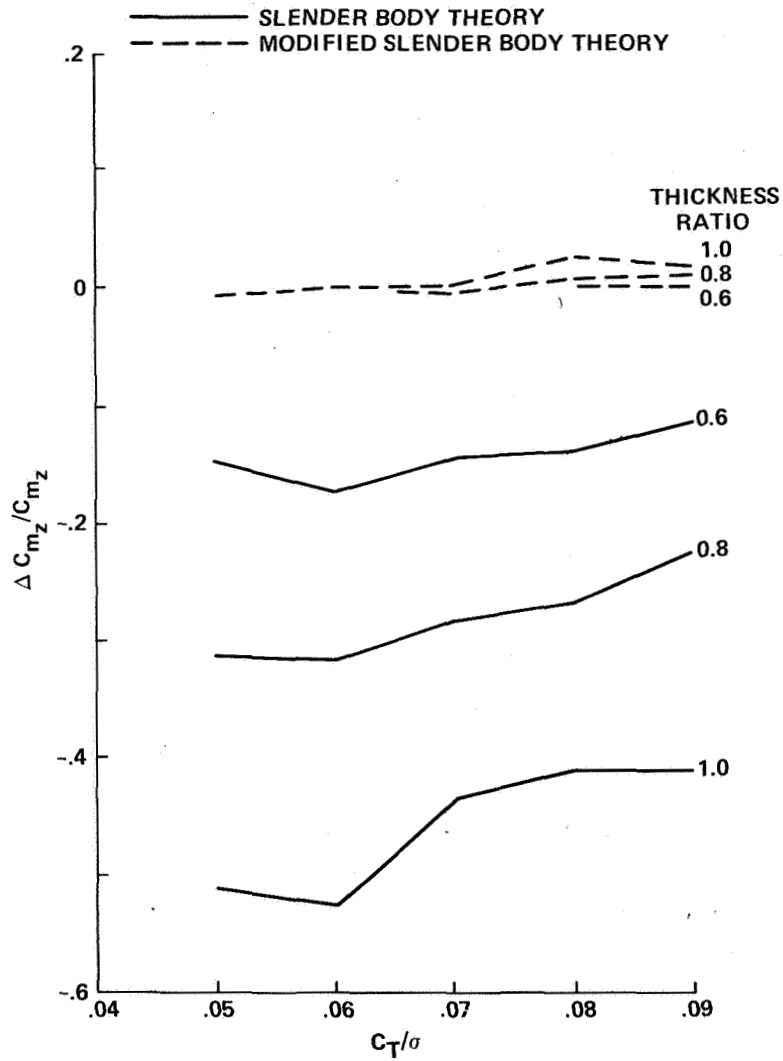
(a) Lateral cyclic control angle (deg).

Figure 32.- Error in lateral cyclic control angle (deg) and lift-to-drag ratio for rotor A in combination with airfoil shaped bodies of various thicknesses (case 1).



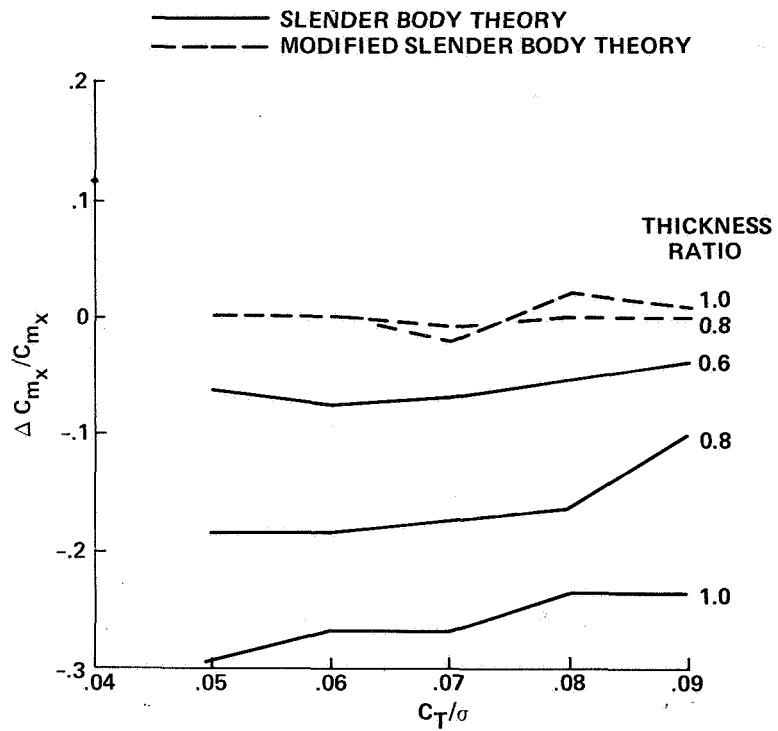
(b) Lift-to-drag ratio.

Figure 32.- Concluded.



(a) Oscillatory edgewise bending loads.

Figure 33.- Error in oscillatory bending loads at 0.6R for rotor B in combination with ellipsoids of various thicknesses (case 1).



(b) Oscillatory flapwise bending loads.

Figure 33.- Concluded.

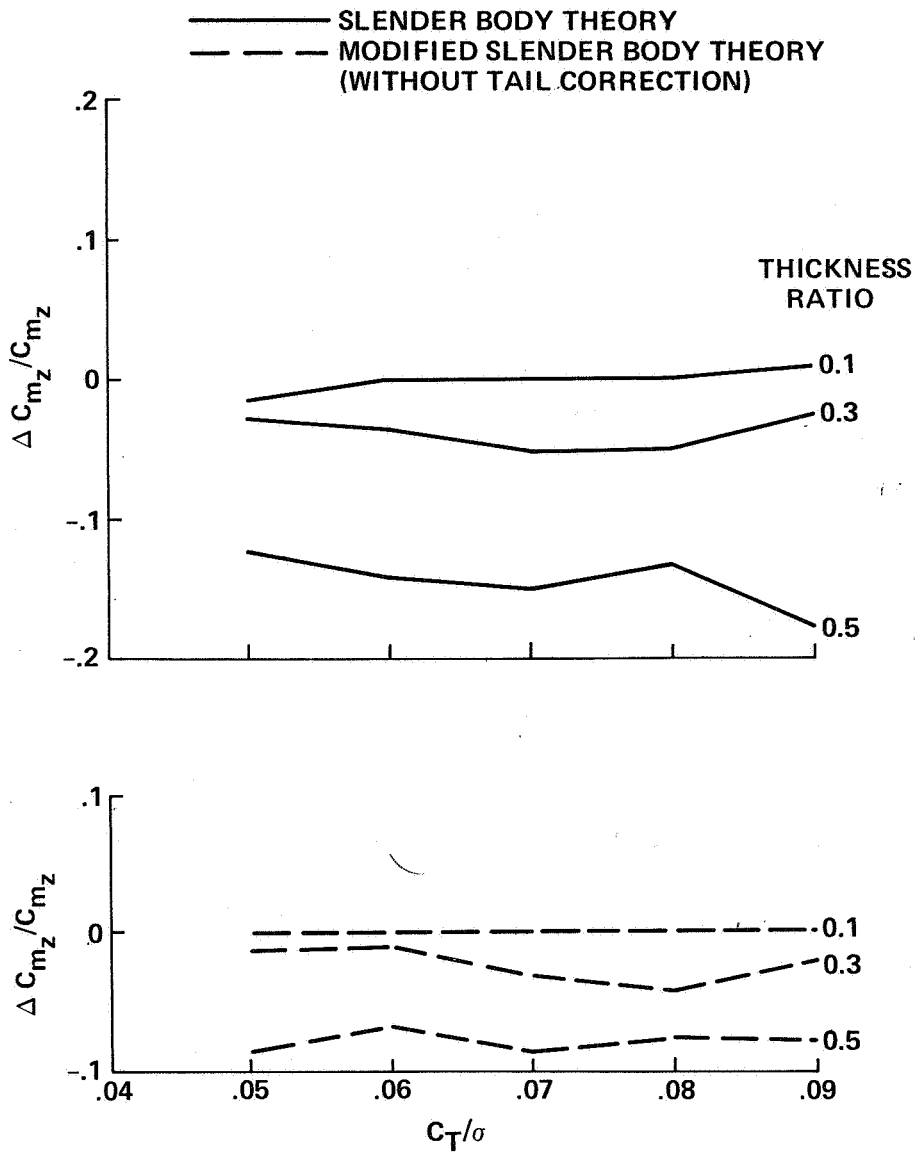
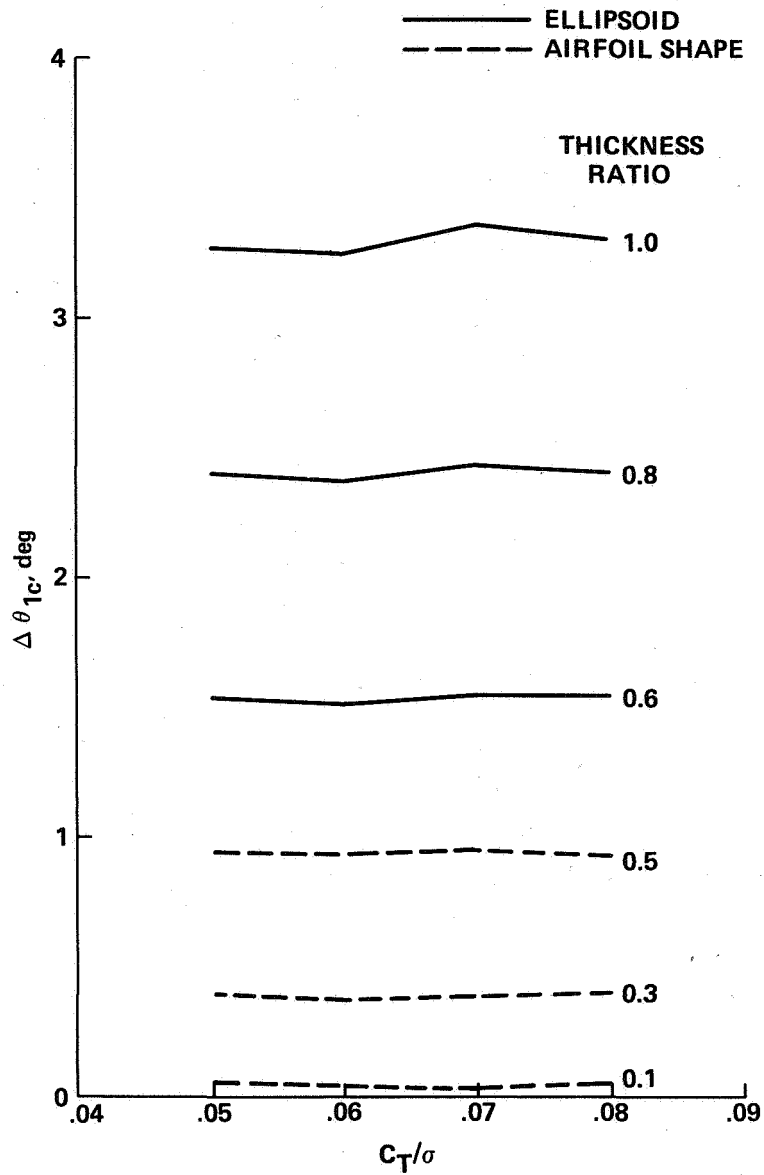
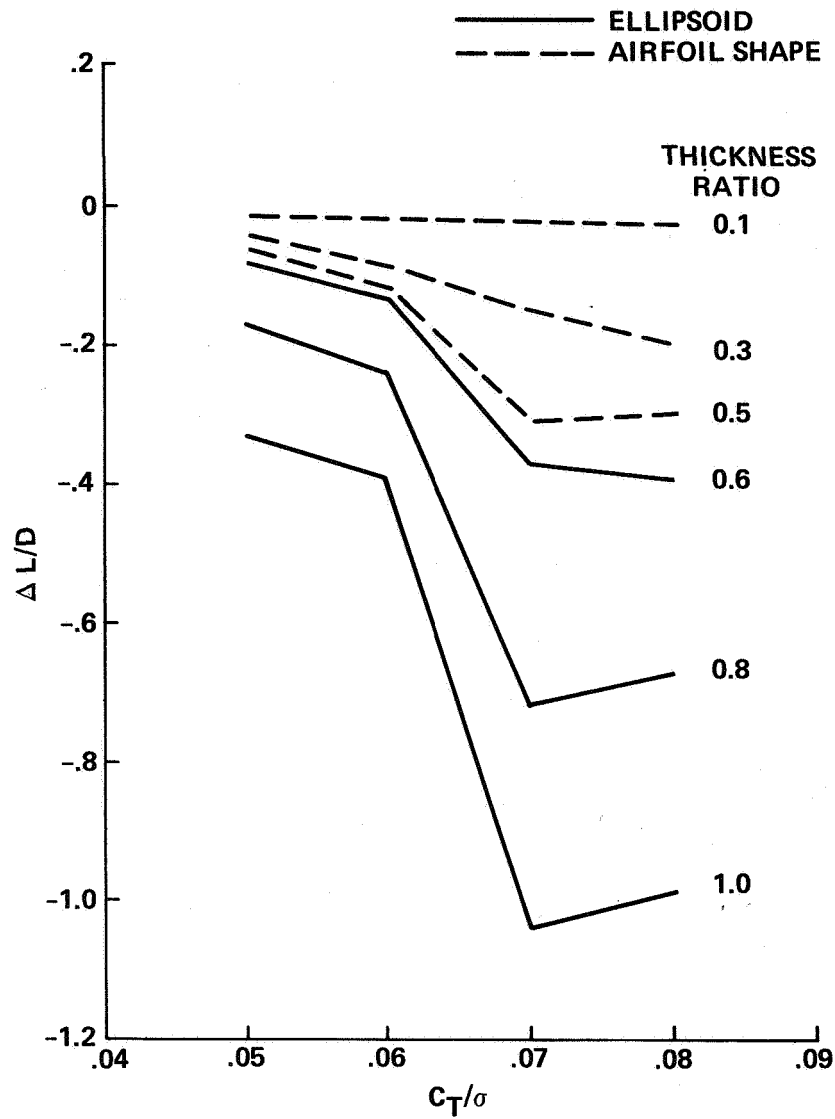


Figure 34.- Error in oscillatory bending loads at 0.6R for rotor B in combination with airfoil shaped bodies of various thicknesses (case 1).



(a) Lateral cyclic control angle (deg).

Figure 35.- Change in lateral cyclic control angle (deg) and lift-to-drag ratio for rotor A due to bodies of various thicknesses (case 1).



(b) Lift-to-drag ratio.

Figure 35.- Concluded.

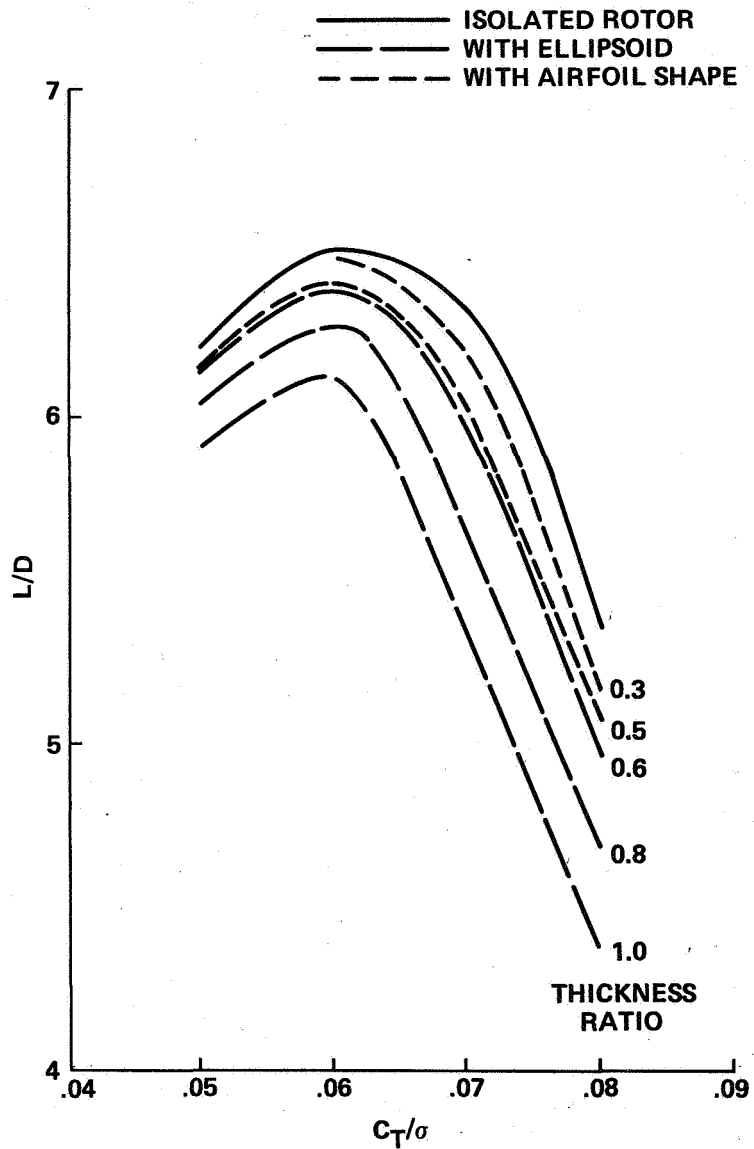
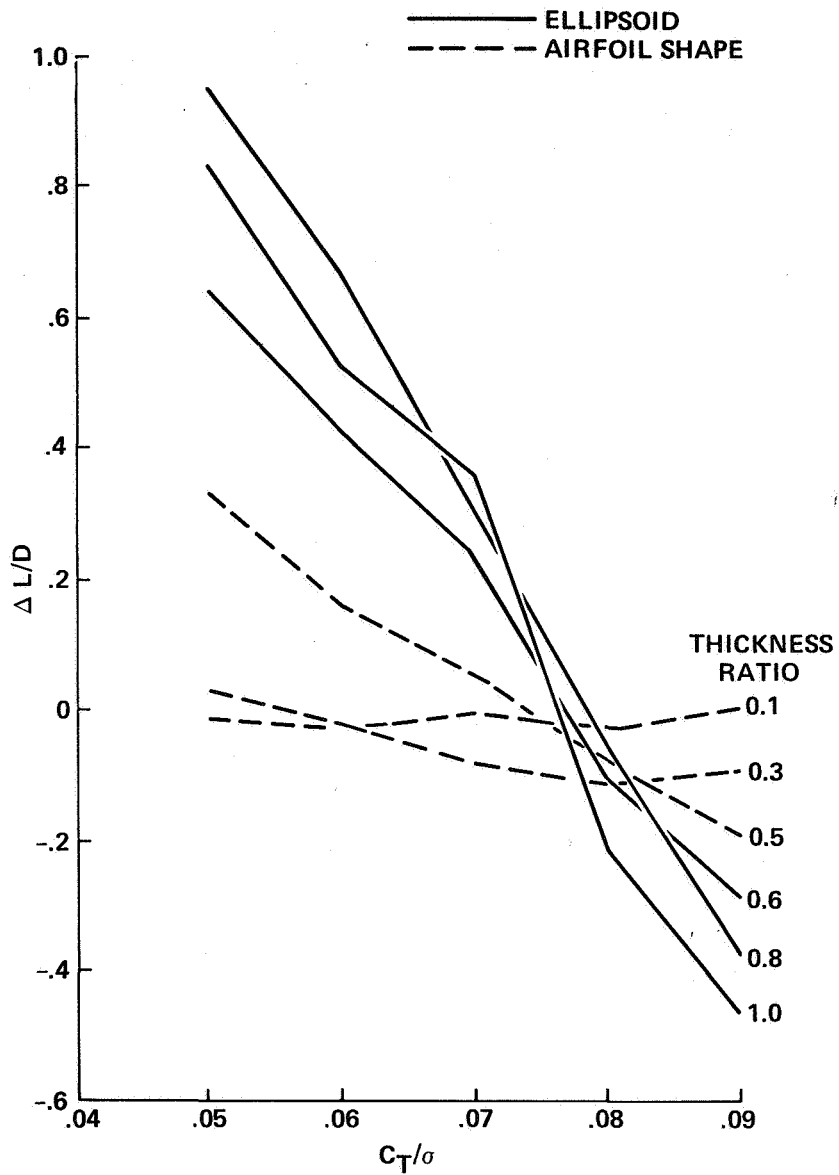
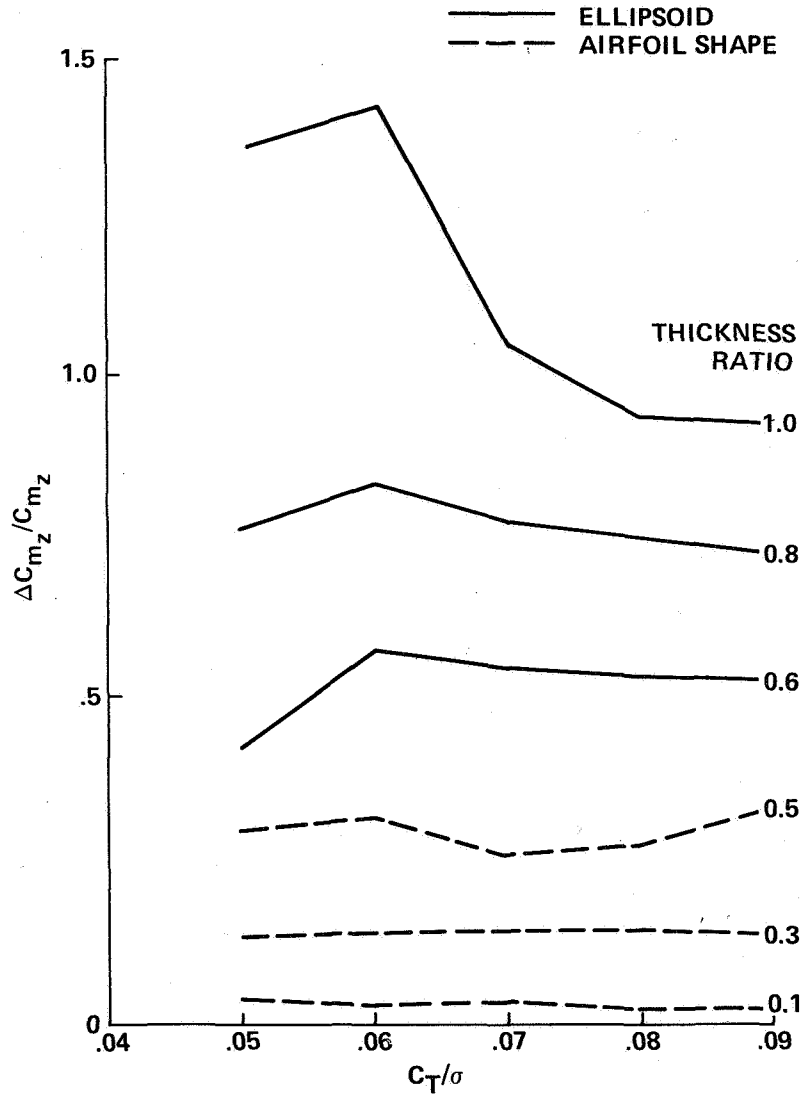


Figure 36.- Lift-to-drag ratio for rotor A in combination with bodies of various thicknesses (case 1).



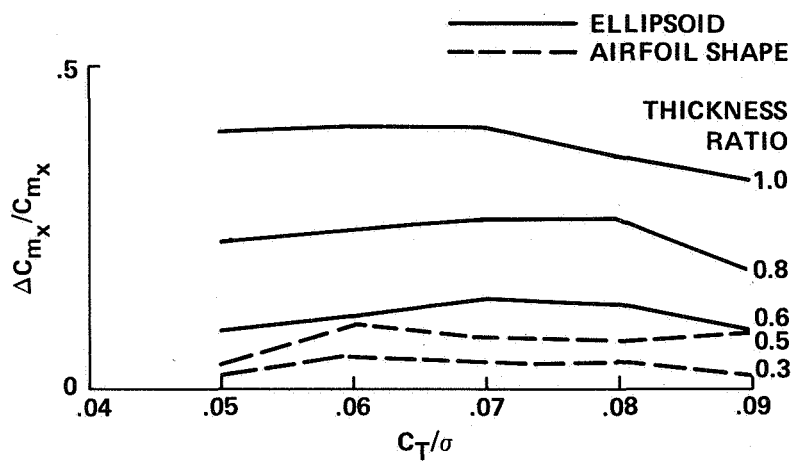
(a) Lift-to-drag ratio.

Figure 37.- Change in lift-to-drag ratio and oscillatory bending loads for rotor B due to bodies of various thicknesses (case 1).



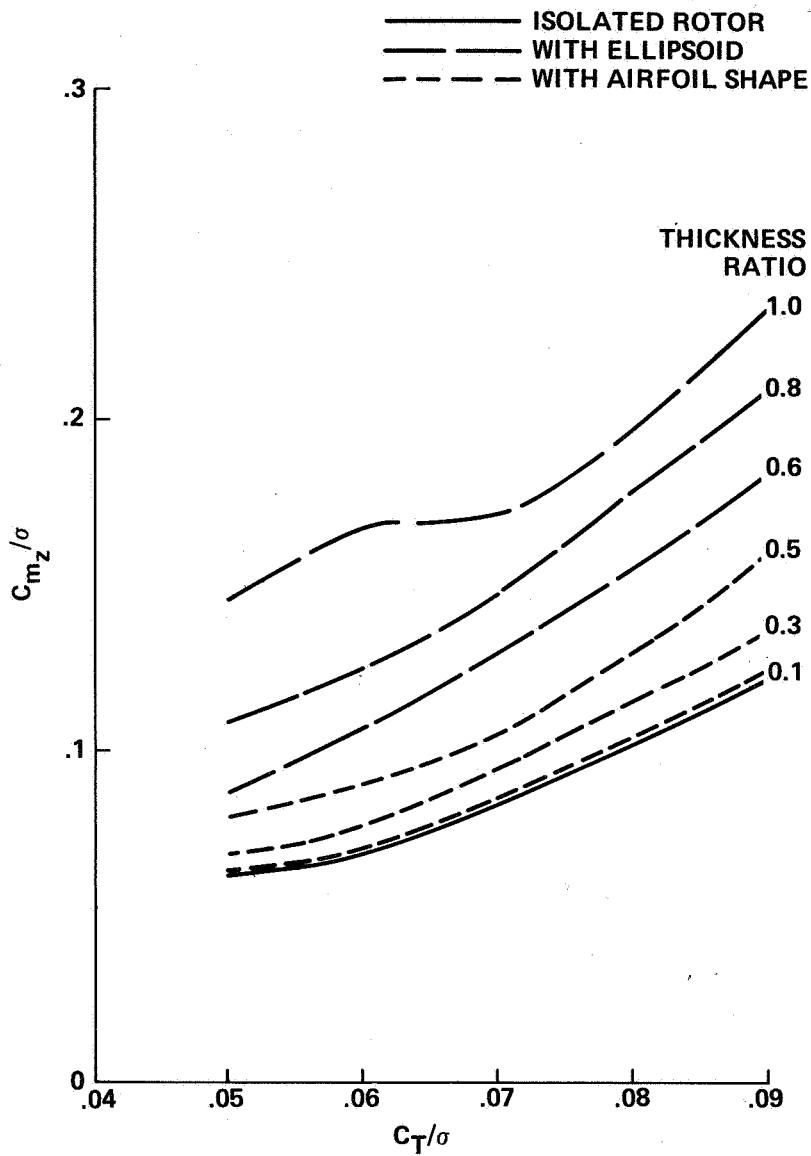
(b) Oscillatory edgewise bending loads (at 0.6R).

Figure 37.- Continued.



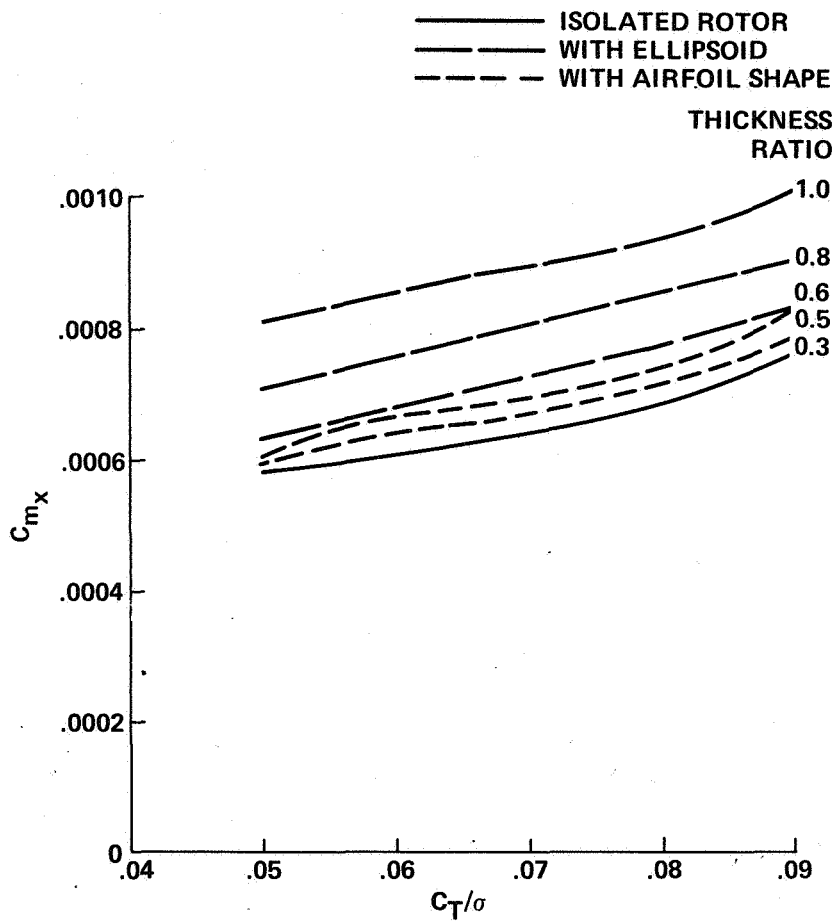
(c) Oscillatory flapwise bending loads (at 0.6R).

Figure 37.- Concluded.



(a) Oscillatory edgewise bending loads.

Figure 38.- Oscillatory bending loads at 0.6R for rotor B in combination with bodies of various thicknesses (case 1).



(b) Oscillatory flapwise bending loads.

Figure 38.- Concluded.

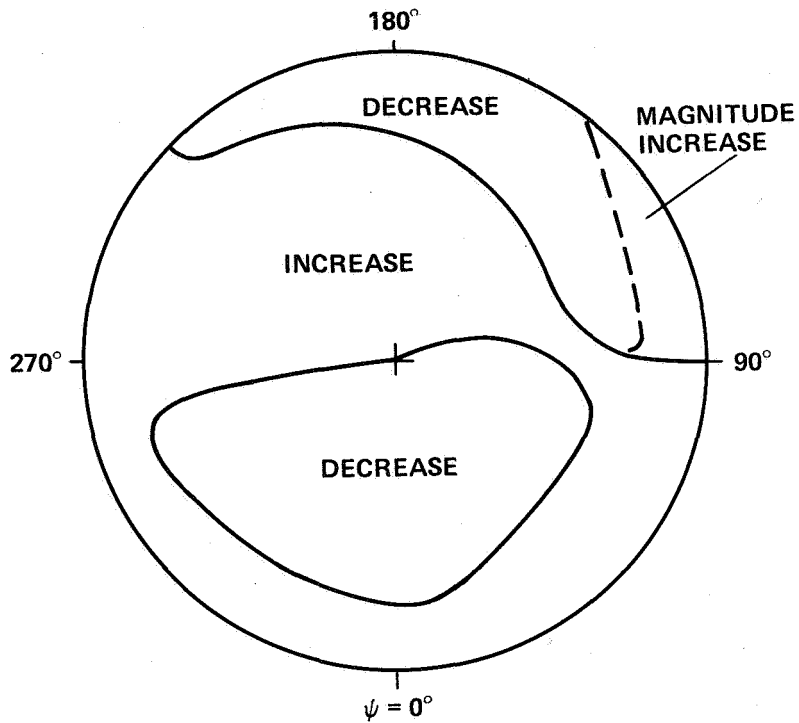
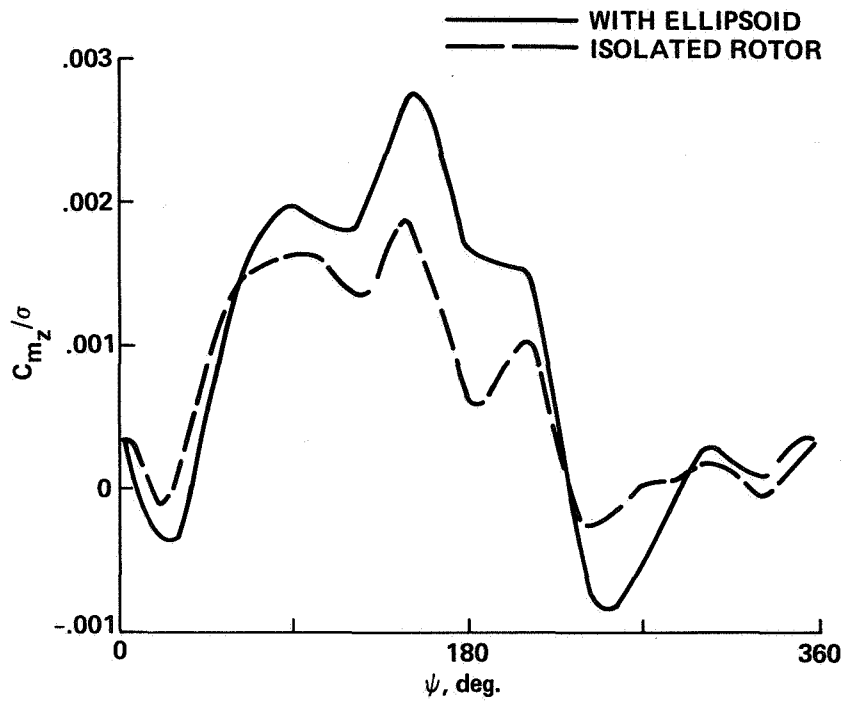
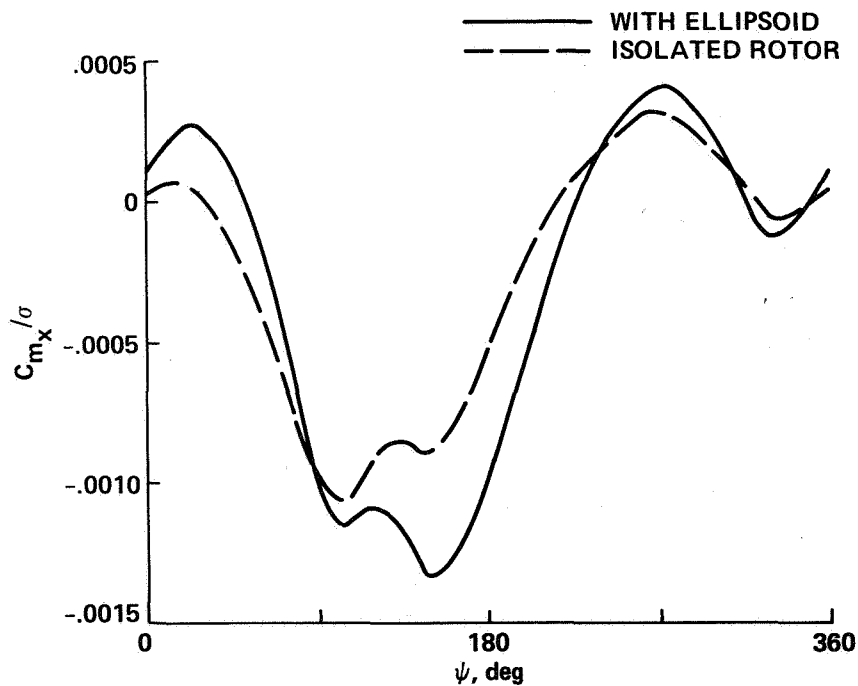


Figure 39.- Angle of attack change (deg) for rotor A at $C_T/\sigma = 0.08$ due to an 80%-thick ellipsoid (case 1).



(a) Edgewise bending moment.



(b) Flapwise bending moment.

Figure 40.- Time-histories of bending moments at 0.6R for rotor B at $C_T/\sigma = 0.08$ with an 80%-thick ellipsoid (case 1).

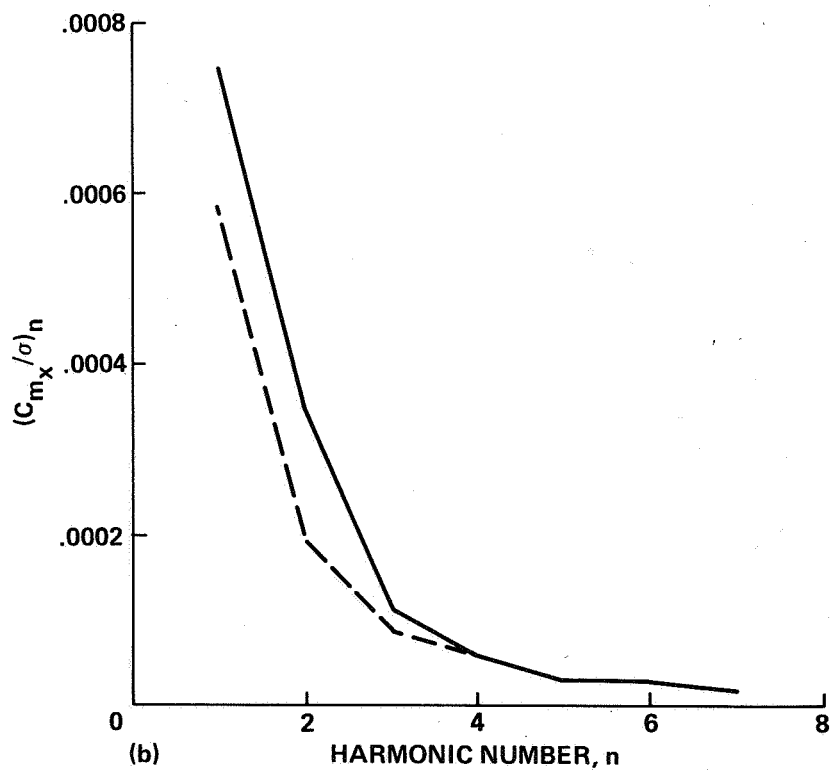
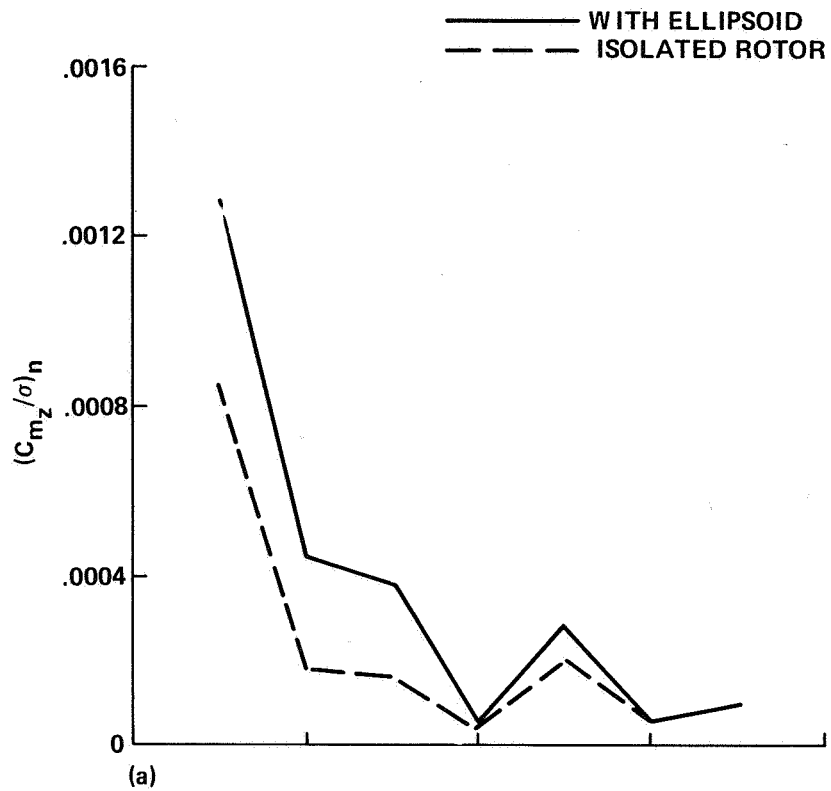


Figure 41.- Moduli of the harmonics of the bending moments at 0.6R for rotor B with an 80%-thick ellipsoid (case 1). (a) Edgewise bending moment; (b) flapwise bending moment.

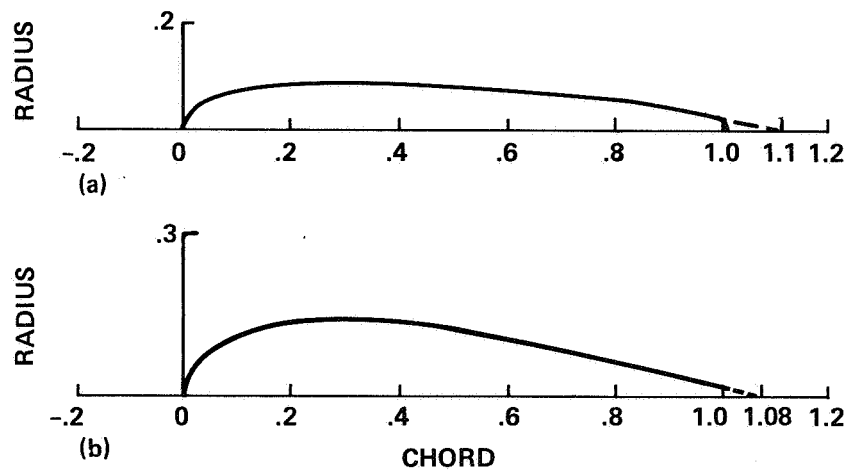


Figure 42.- Body streamlines of test modules (dashed lines are tail extensions).
 (a) Rotor Test Apparatus (RTA); (b) Easter Egg (EE).

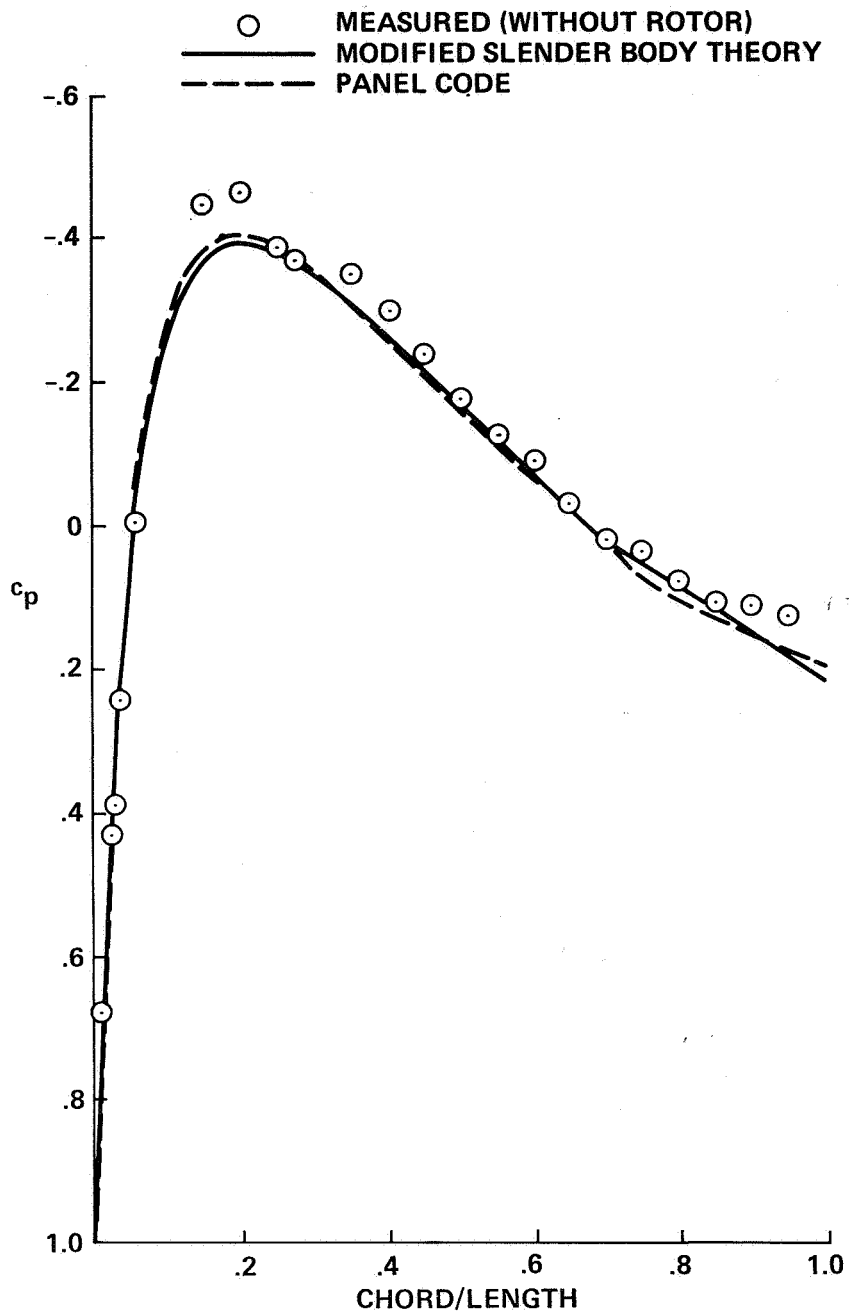


Figure 43.- Pressure distribution on an isolated Easter Egg at zero angle of attack, compared with measured data (ref. 8) and with panel code calculations (ref. 8).

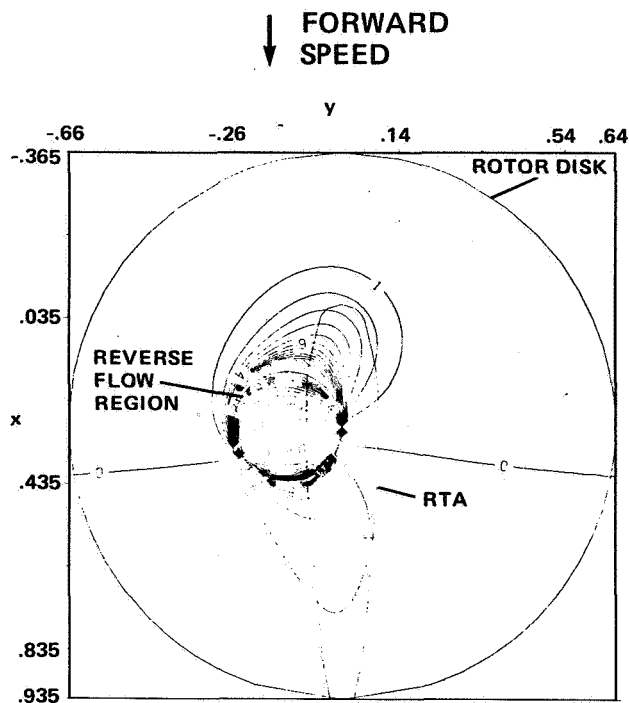


Figure 44.- Plot of rotor blade angle-of-attack change (deg) due to the RTA in the plane of the rotor disk (case 2).

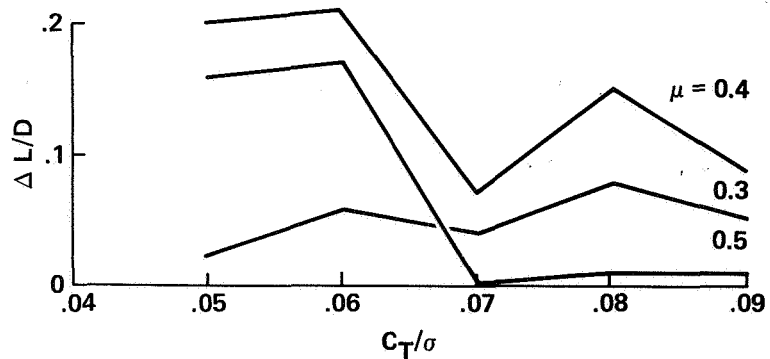


Figure 45.- Improvement in lift-to-drag ratio for rotor B due to the RTA (case 2).

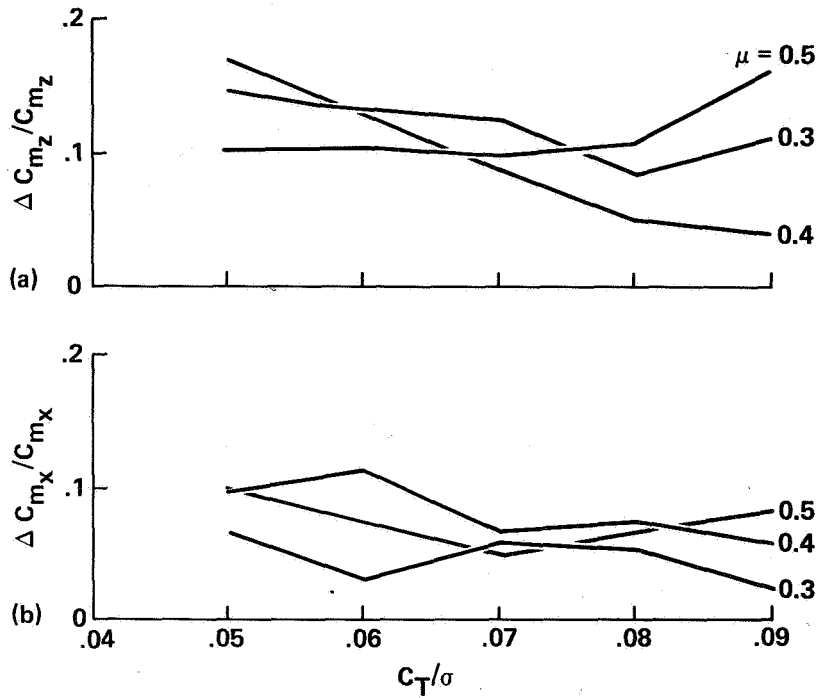


Figure 46.- Increase in oscillatory bending moments for rotor B due to the RTA (case 2). (a) Oscillatory edgewise bending moment at $0.6R$; (b) oscillatory flapwise bending moment at $0.7R$.

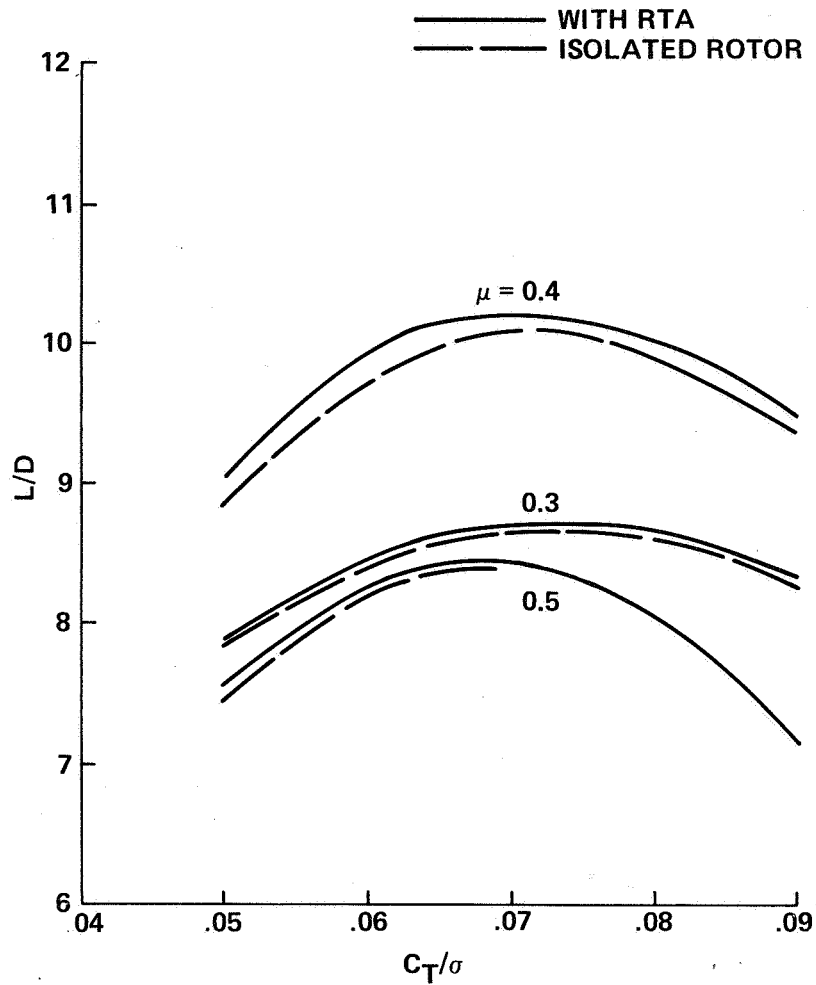
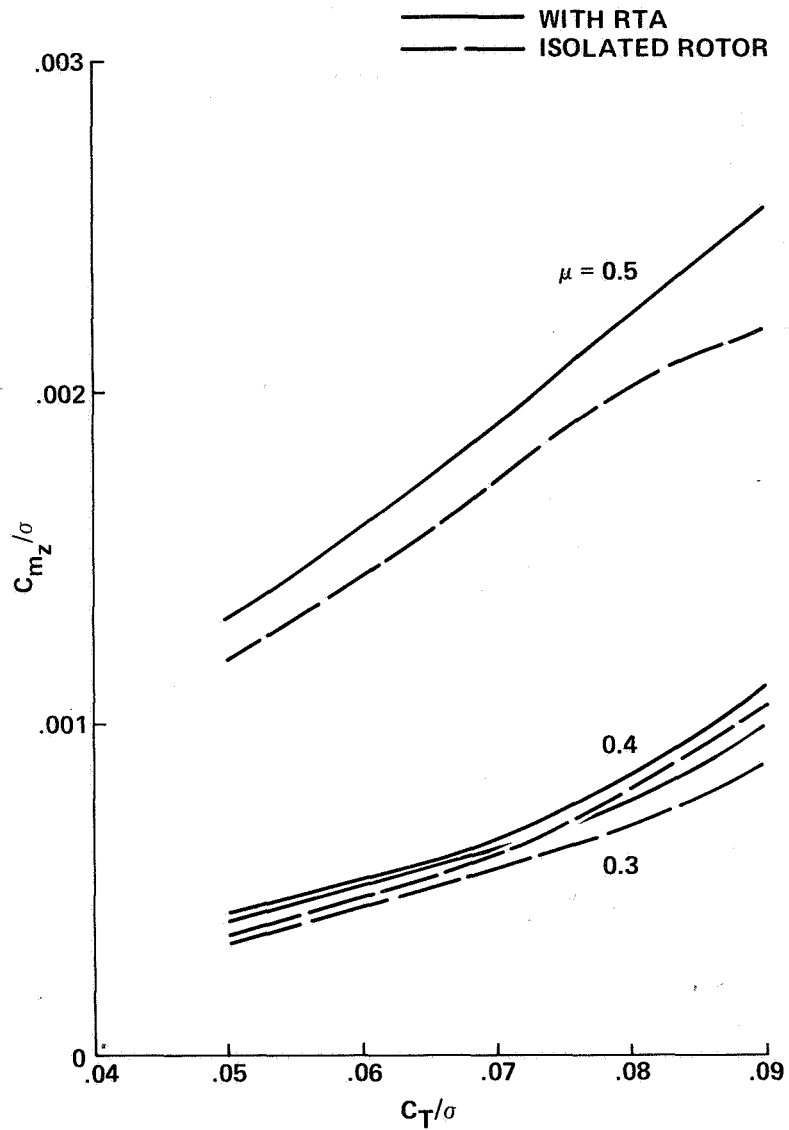
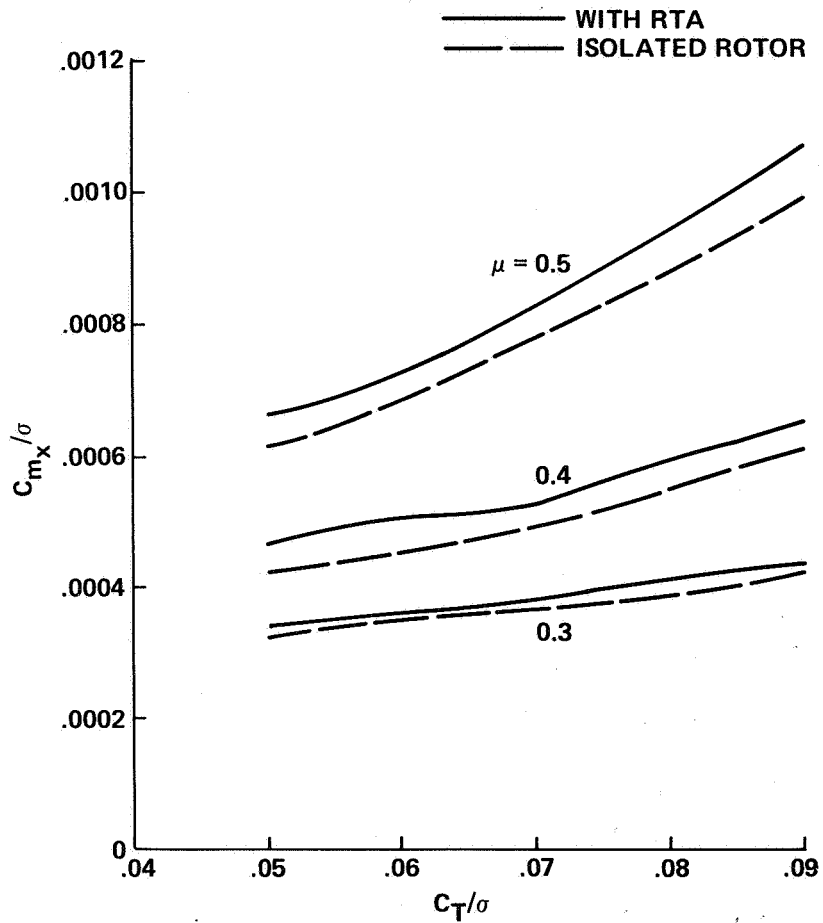


Figure 47.- Lift-to-drag ratio for rotor B and RTA configuration for several advance ratios (case 2).



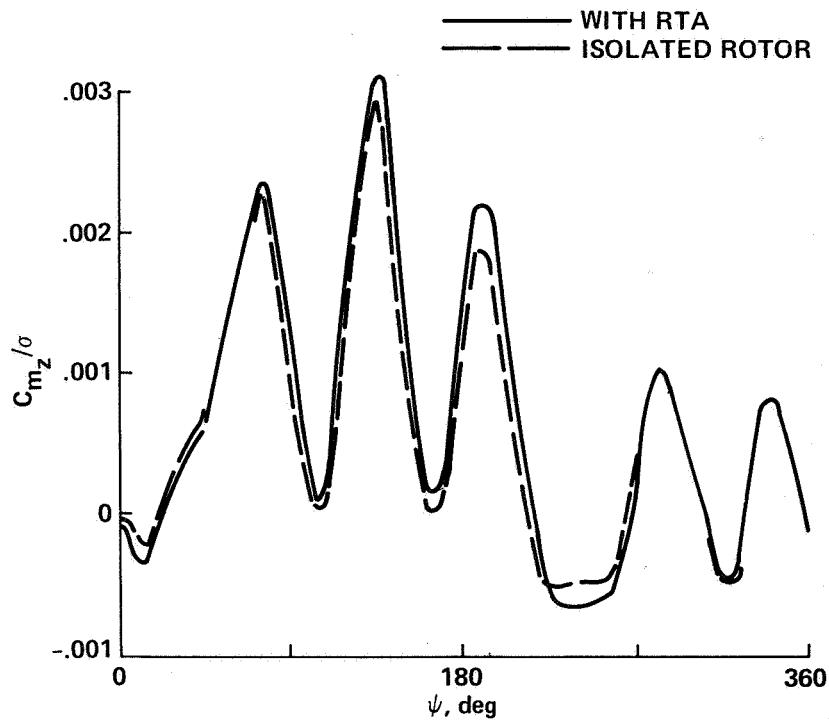
(a) Oscillatory edgewise bending moment at 0.6R.

Figure 48.- Oscillatory bending moments for rotor B and RTA configuration for several advance ratios (case 2).

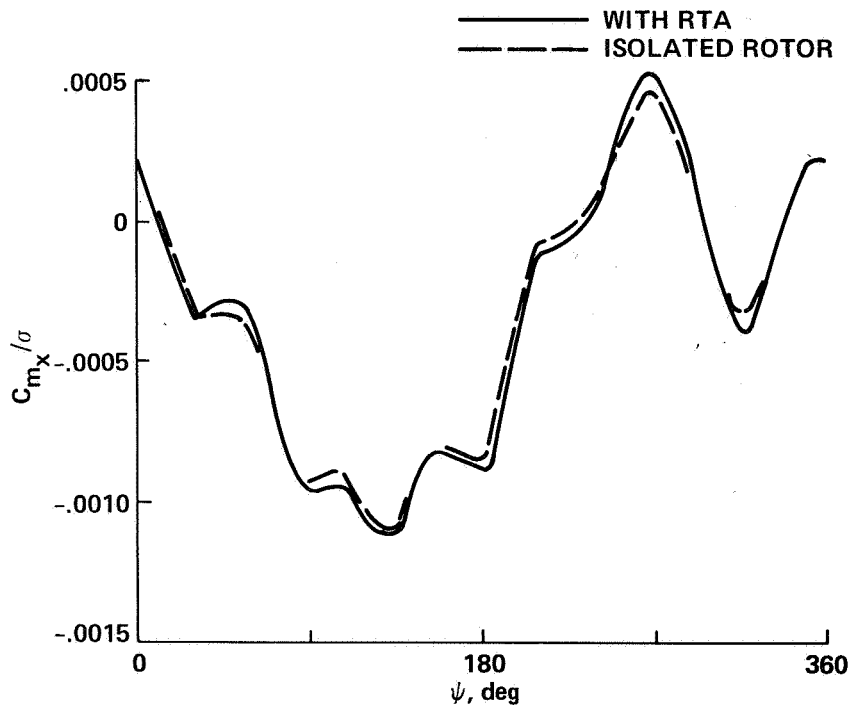


(b) Oscillatory flapwise bending moment at 0.7R.

Figure 48.- Concluded.



(a) Edgewise bending moment at 0.6R.



(b) Flapwise bending moment at 0.7R.

Figure 49.- Time-histories of bending moments for rotor B and RTA configuration at $\mu = 0.5$ and $C_T/\sigma = 0.07$ (case 2).

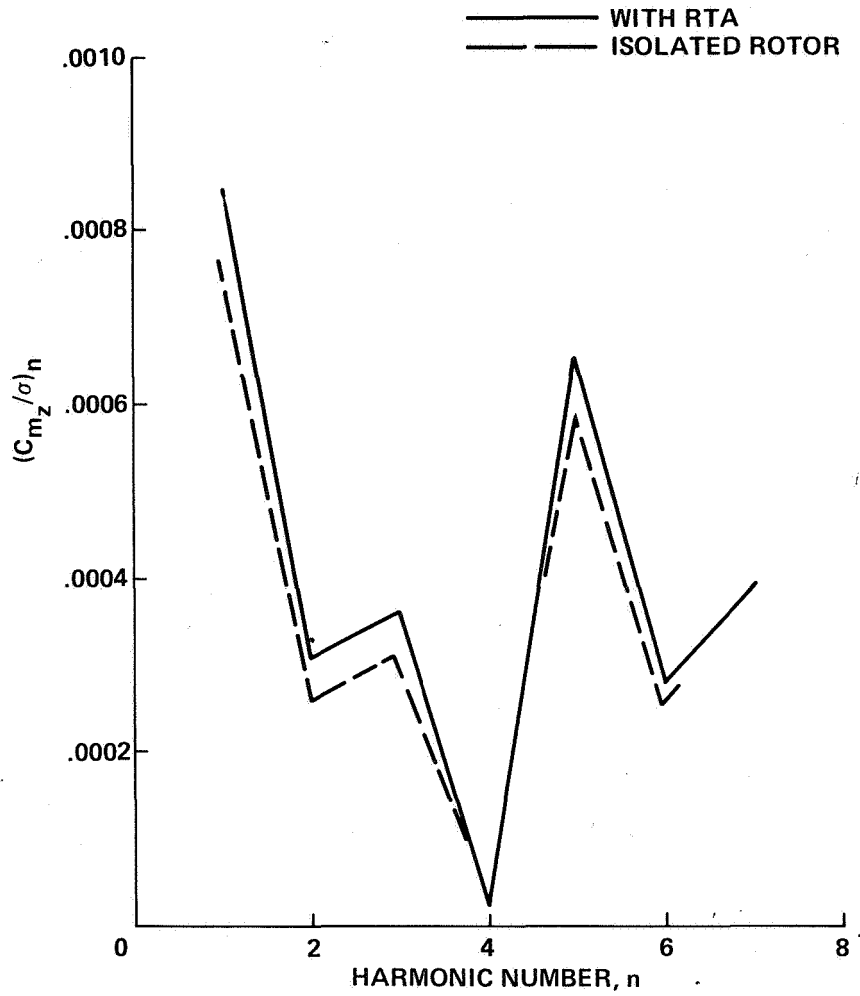


Figure 50.- Moduli of the harmonics of the edgewise bending moment (0.6R) for rotor B and RTA configuration at $\mu = 0.5$ and $C_T/\sigma = 0.07$ (case 2).

↓ FORWARD
SPEED

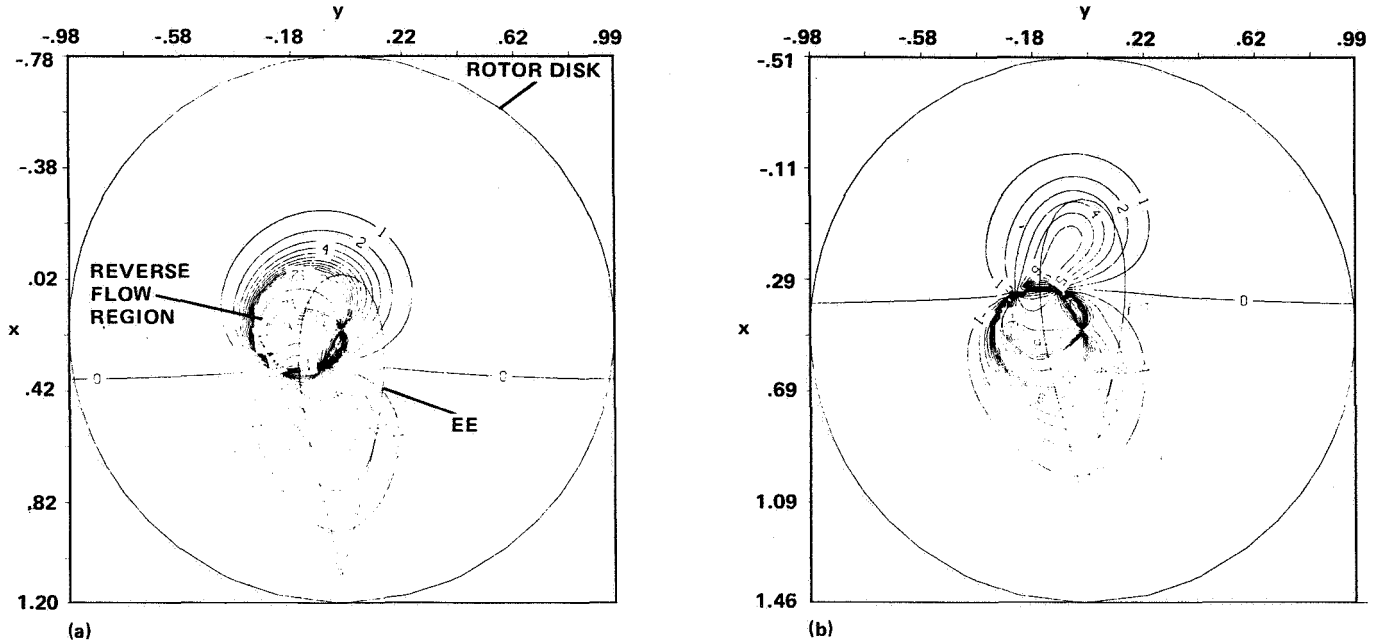


Figure 51.- Plot of rotor blade angle of attack change (deg) due to the EE in plane of the rotor disk (case 3). (a) $(x/l)_{hub} = 0.199$; (b) $(x/l)_{hub} = 0.471$.

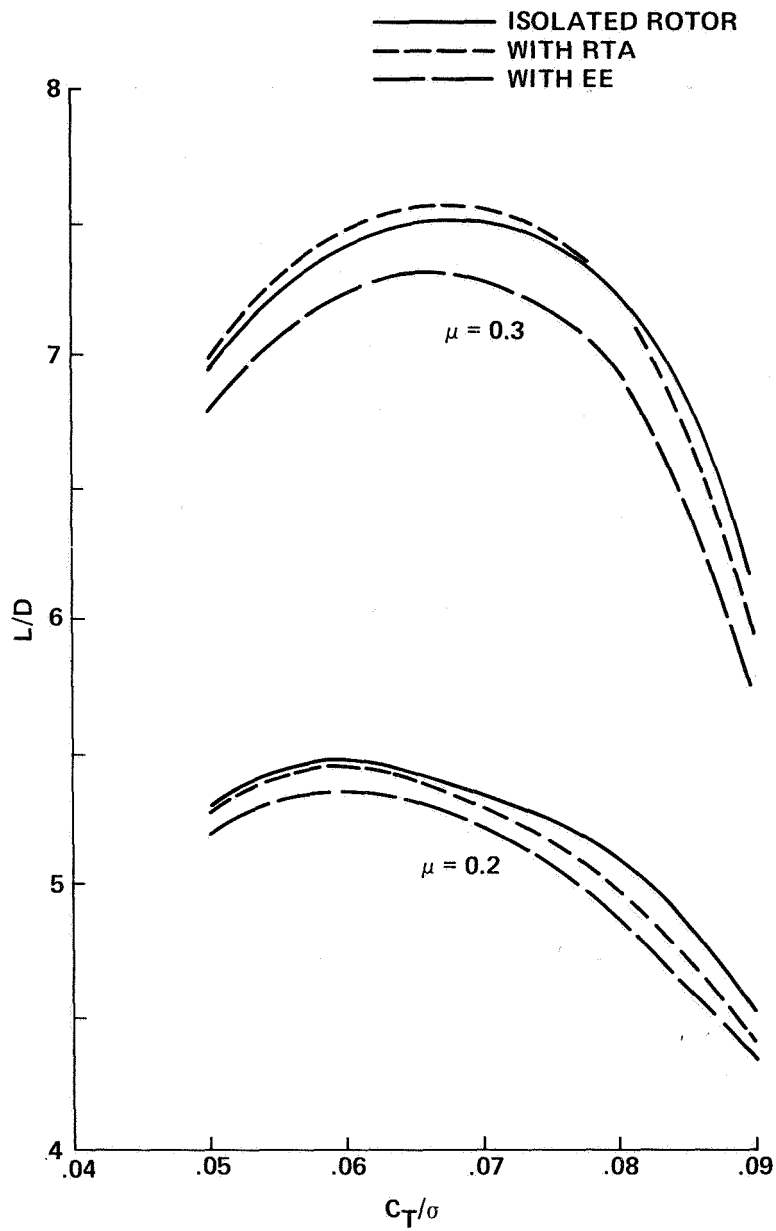


Figure 52.- Lift-to-drag ratio of rotor A in combination with the RTA and EE for several advance ratios (case 3).

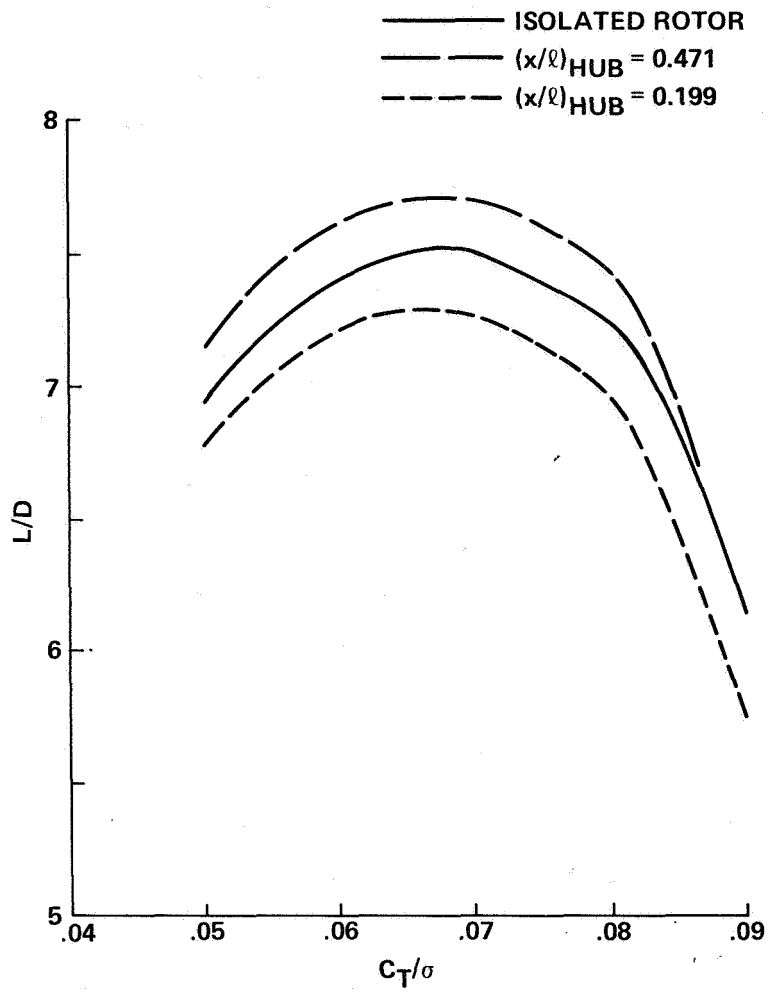


Figure 53.- Effect of changing longitudinal hub position on the lift-to-drag ratio for rotor A and EE configuration (case 3).

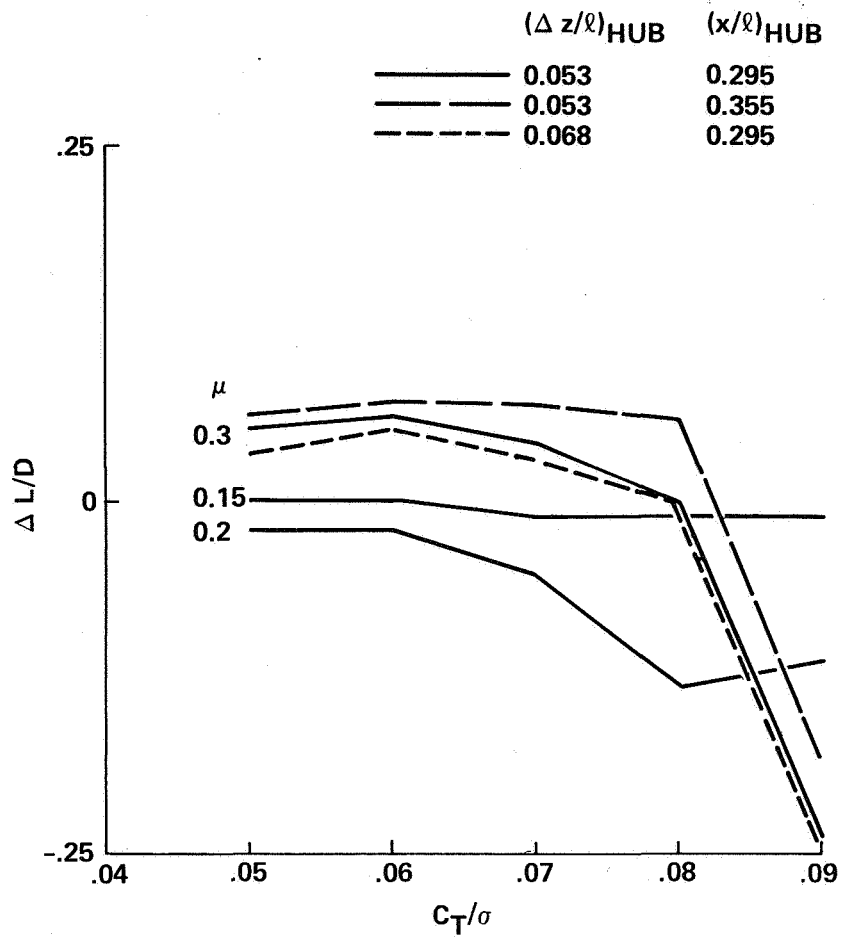
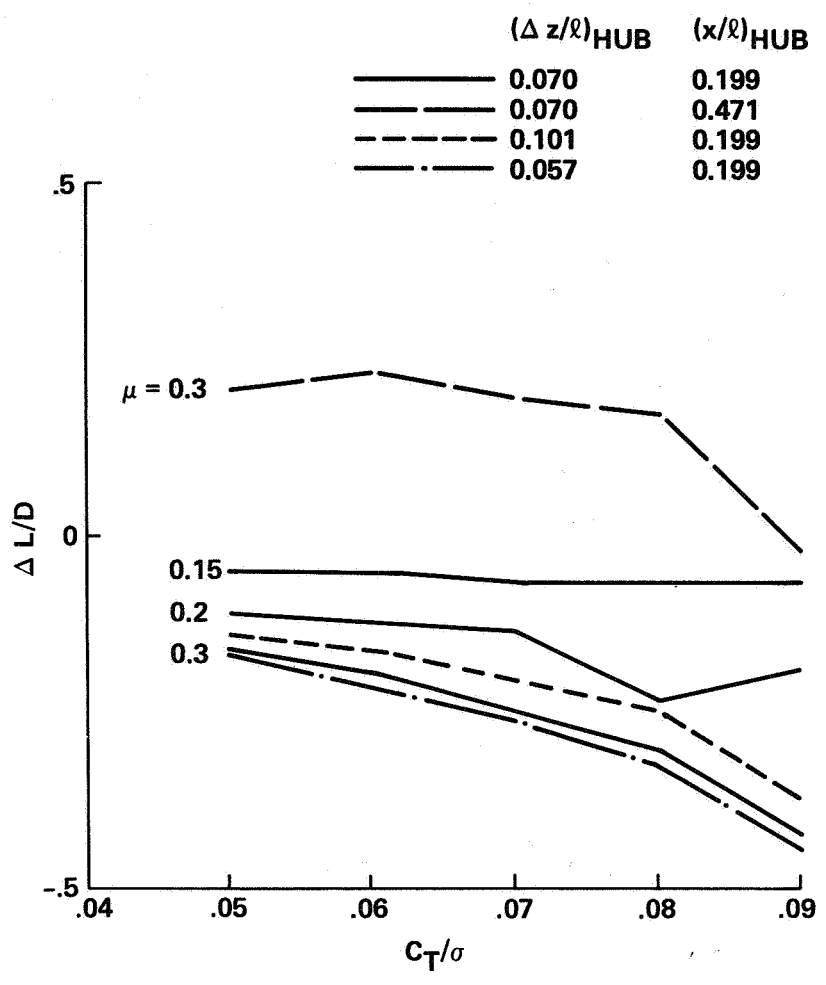


Figure 54.- Effect of changing advance ratio, longitudinal hub position, and rotor-body vertical separation on the change in lift-to-drag ratio of rotor A due to the test modules (case 3).



(b) EE.

Figure 54.- Concluded.

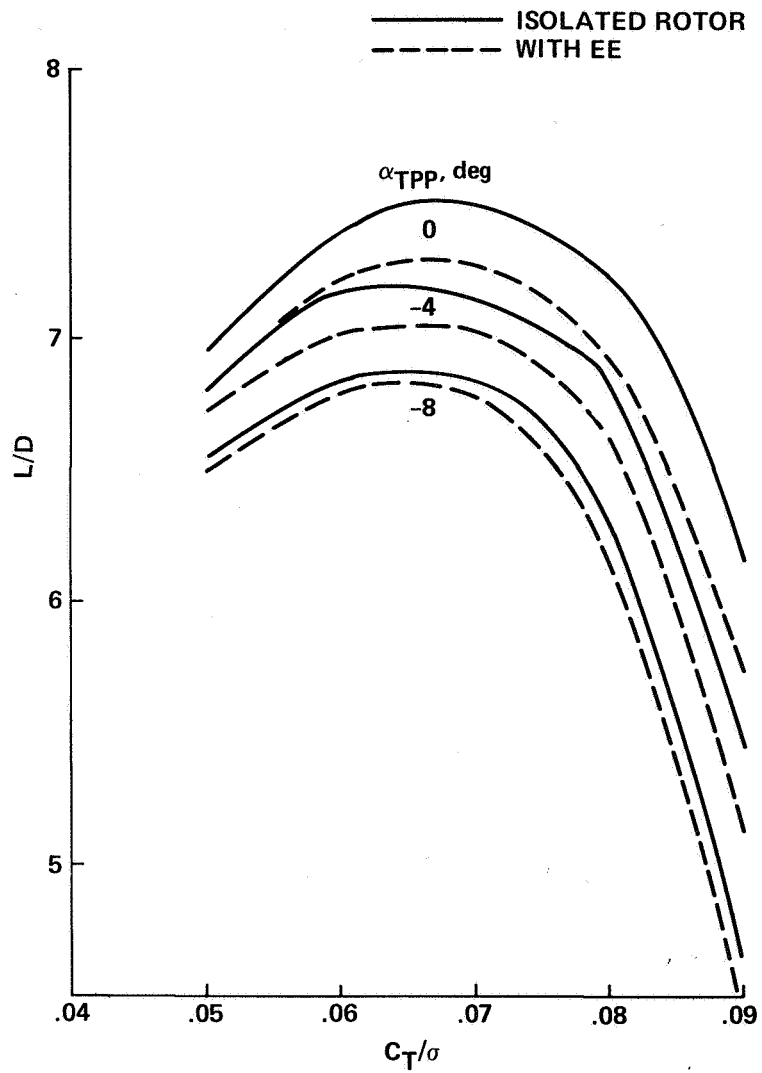
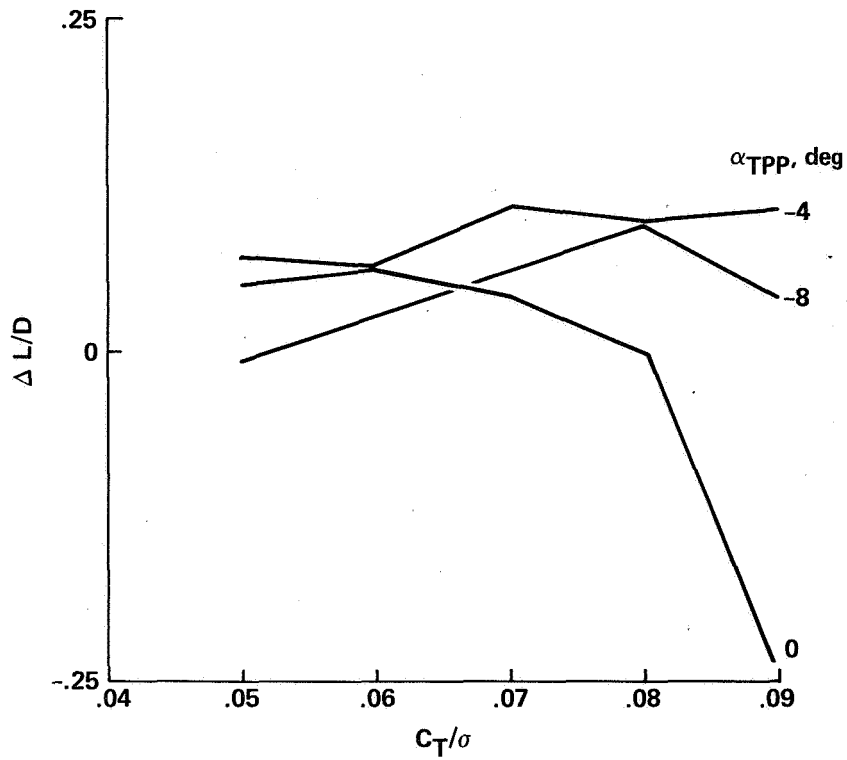
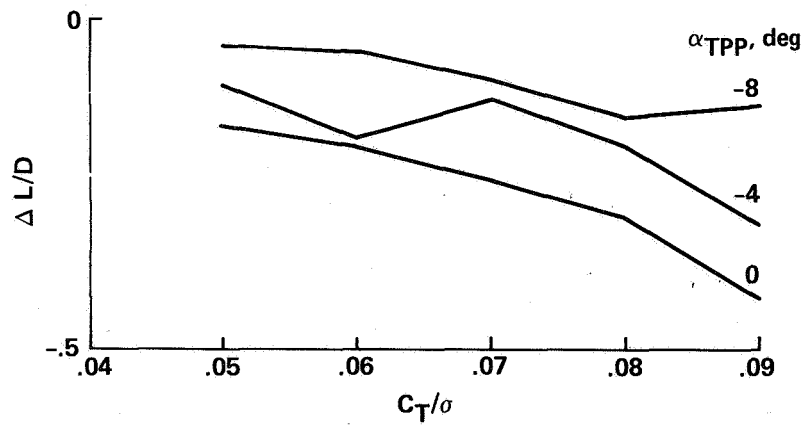


Figure 55.- Lift-to-drag ratio of rotor A and EE configuration for various tip-path-plane angles (case 3).



(a) RTA.



(b) EE.

Figure 56.- Change in lift-to-drag ratio for rotor A due to the test modules for several tip-path-plane angles (case 3).

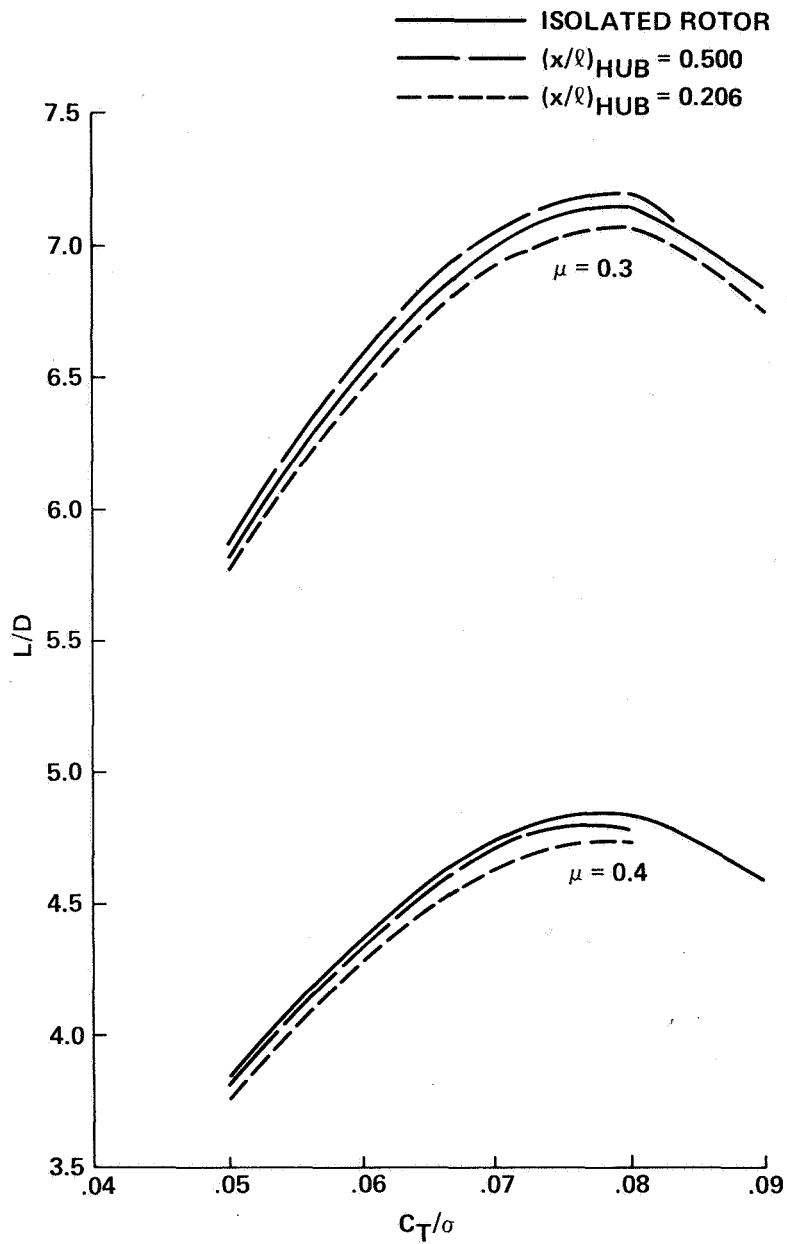


Figure 57.- Effect of hub position on the lift-to-drag ratio for rotor C and EE configuration (case 4).

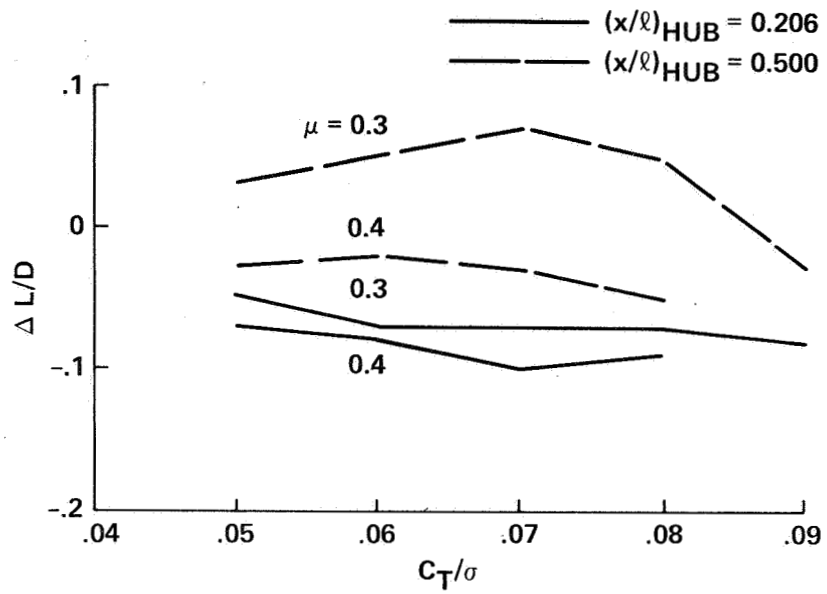


Figure 58.- Effect of hub position on the change in lift-to-drag ratio for rotor C due to the EE for two advance ratios (case 4).

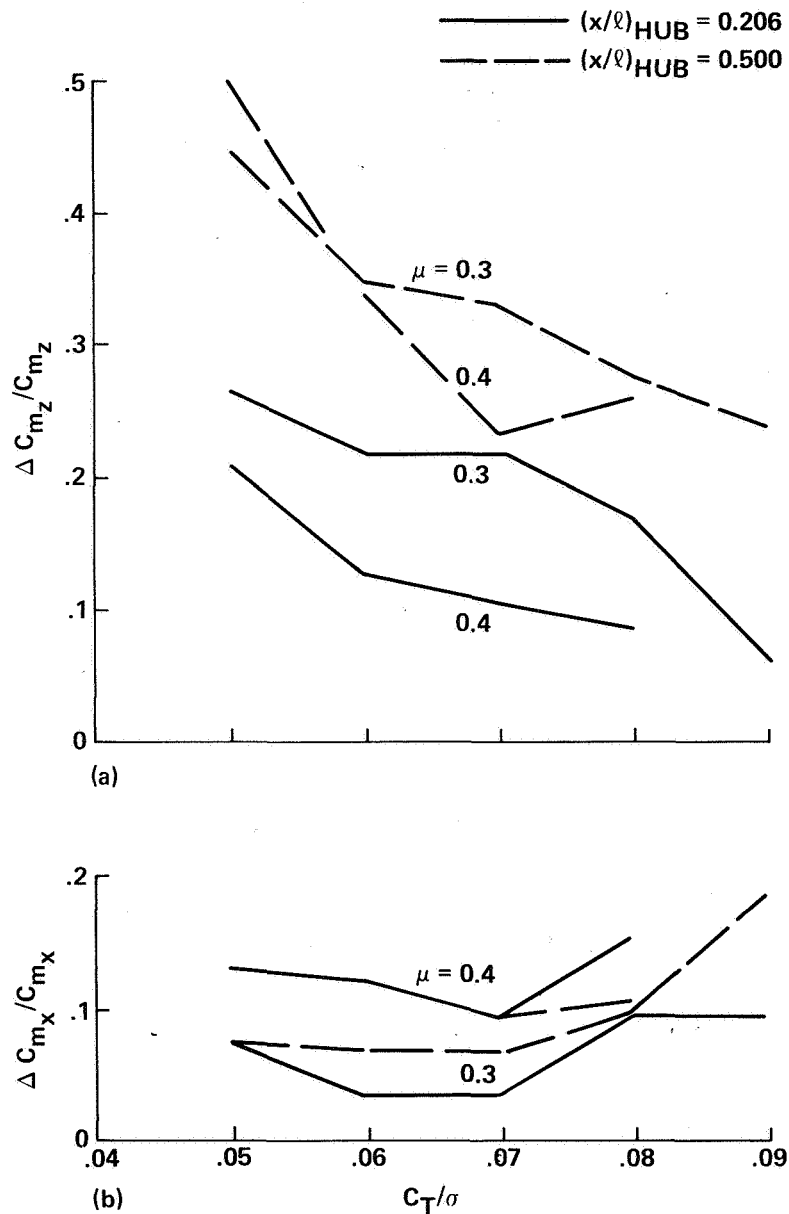
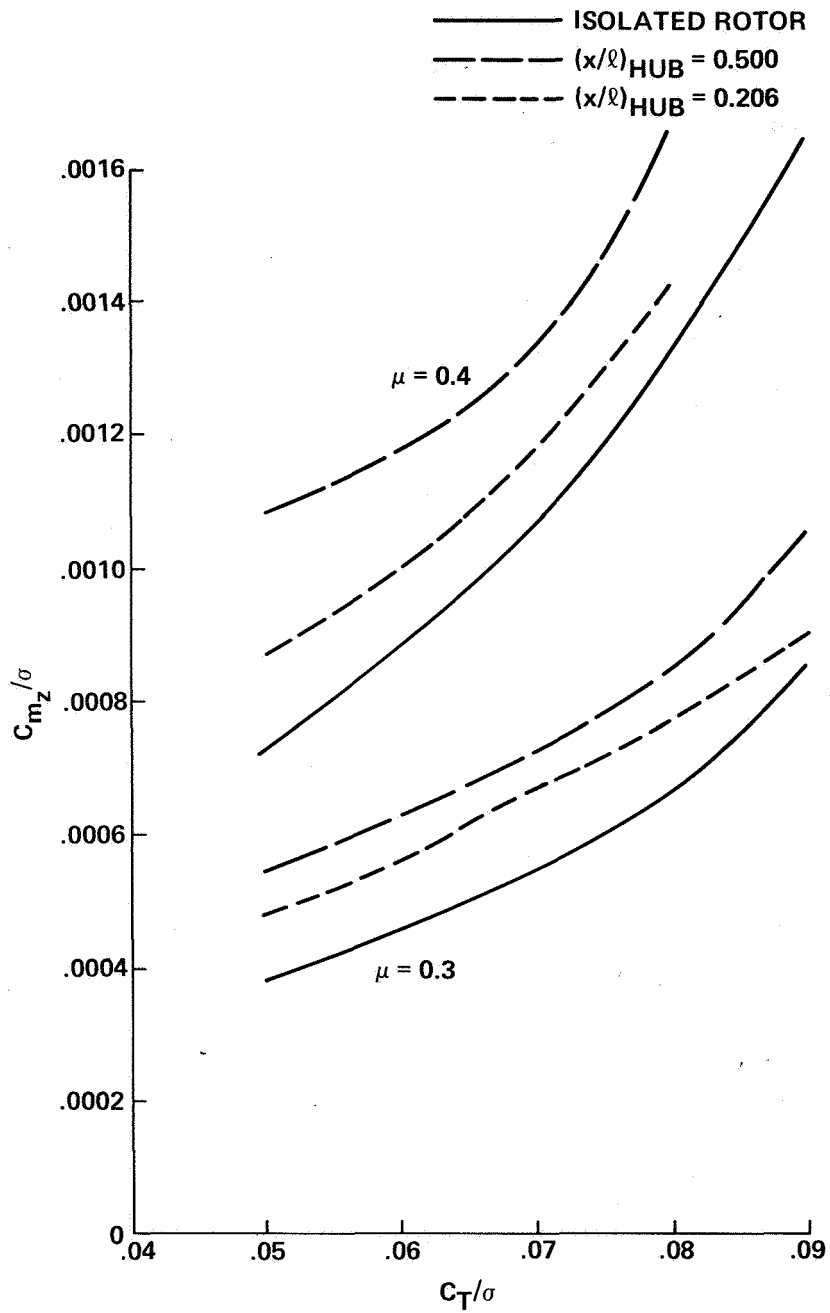
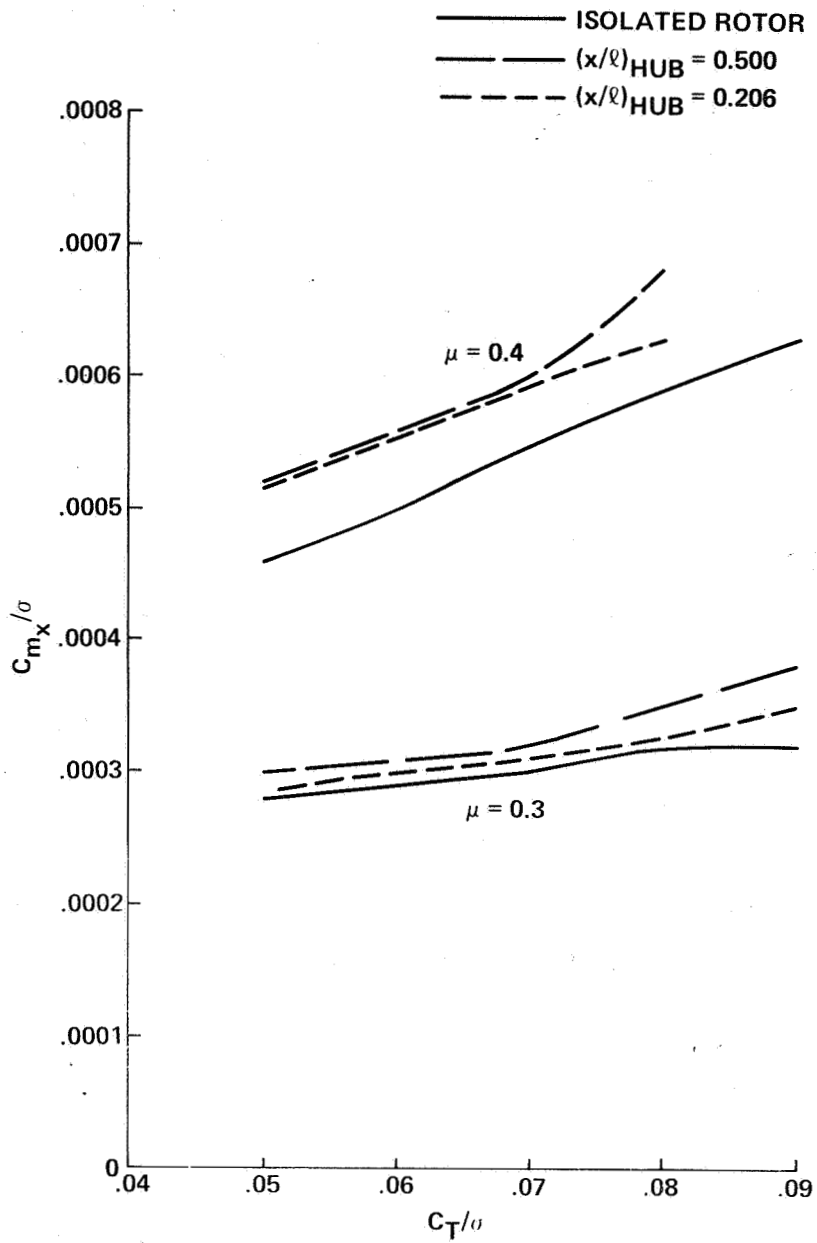


Figure 59.- Effect of hub position on the increase in oscillatory bending moments at 0.5R for rotor C due to the EE for two advance ratios (case 4). (a) Oscillatory edgewise bending moment; (b) oscillatory flapwise bending moment.



(a) Oscillatory edgewise bending moment.

Figure 60.- Effect of hub position on the oscillatory bending moments at 0.5R for rotor C and EE configuration for two advance ratios (case 4).



(b) Oscillatory flapwise bending moment.

Figure 60.- Concluded.

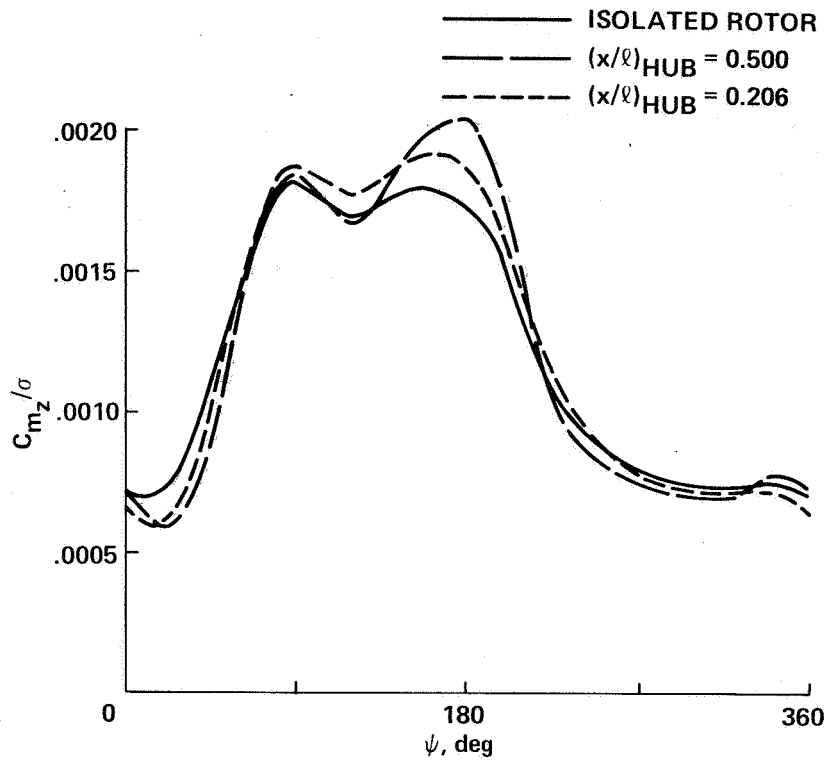
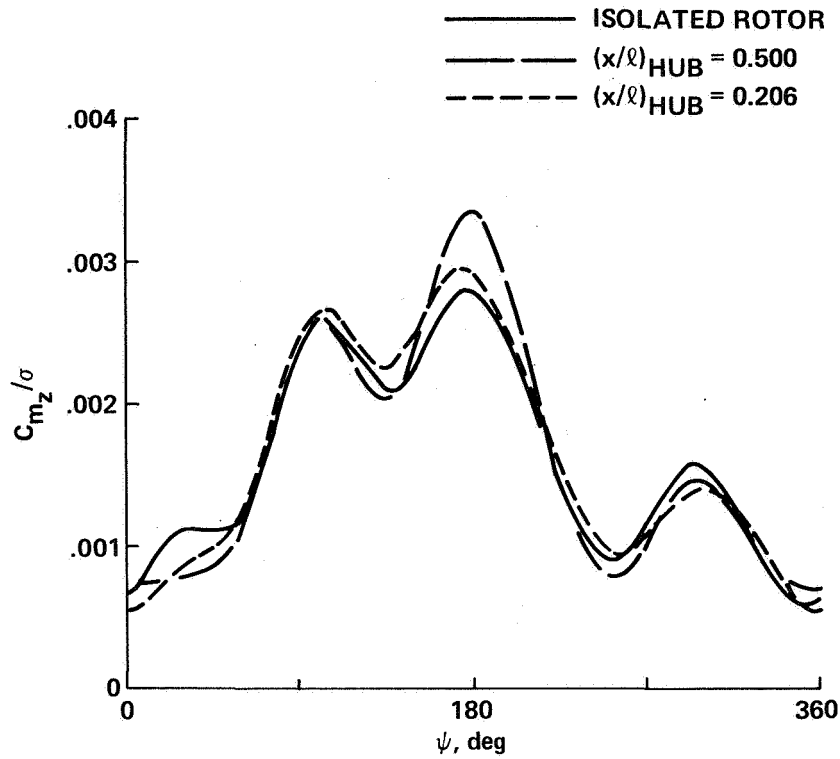
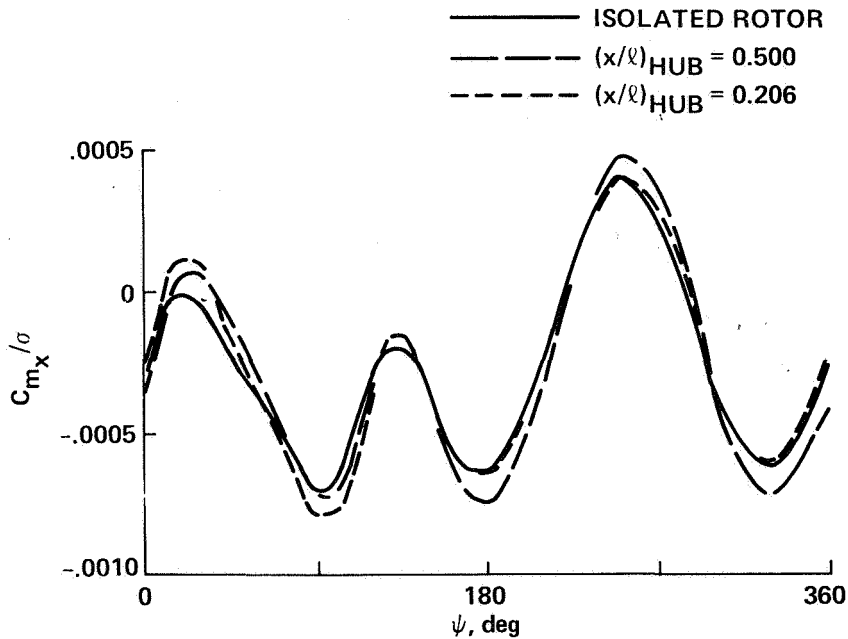


Figure 61.- Effect of hub position on the time-history of the edgewise bending moment at 0.5R for rotor C and EE configuration at $\mu = 0.3$ and $C_T/\sigma = 0.07$ (case 4).



(a) Edgewise bending moment.



(b) Flapwise bending moment.

Figure 62.- Effect of hub position on the time-histories of the bending moments at 0.5R for rotor C and EE configuration at $\mu = 0.4$ and $C_T/\sigma = 0.07$ (case 4).

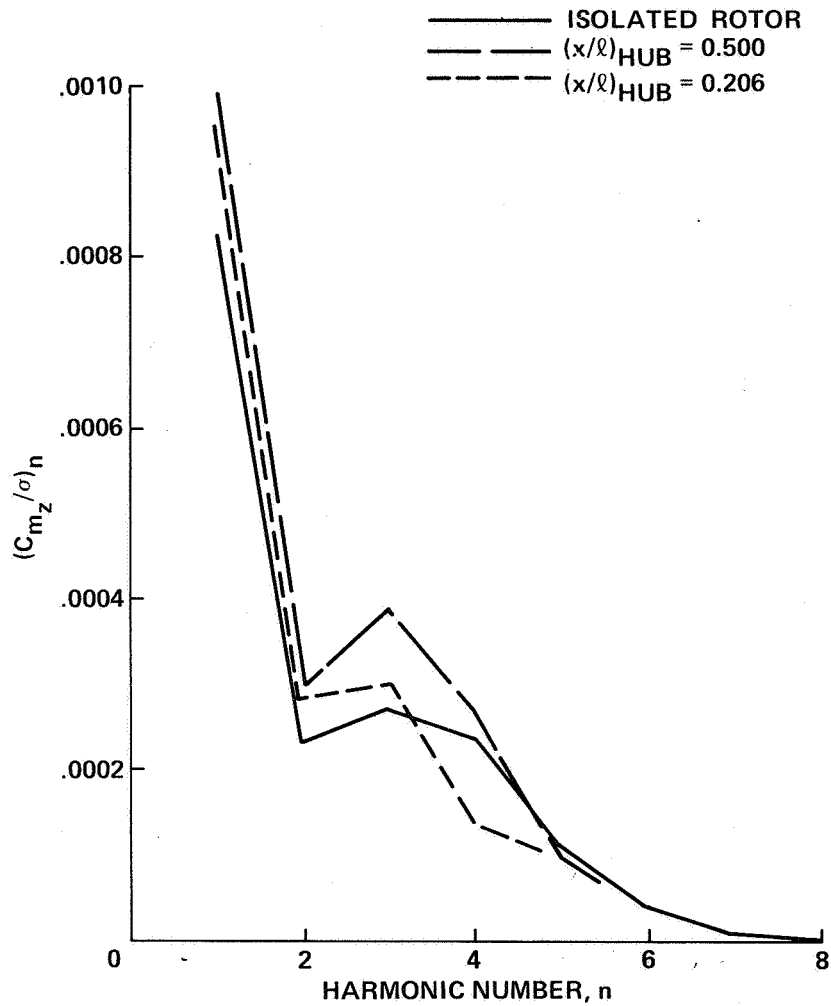


Figure 63.- Effect of hub position on the moduli of the harmonics of the edgewise bending moment at 0.5R for rotor C and EE configuration at $\mu = 0.4$ and $C_T/\sigma = 0.07$ (case 4).

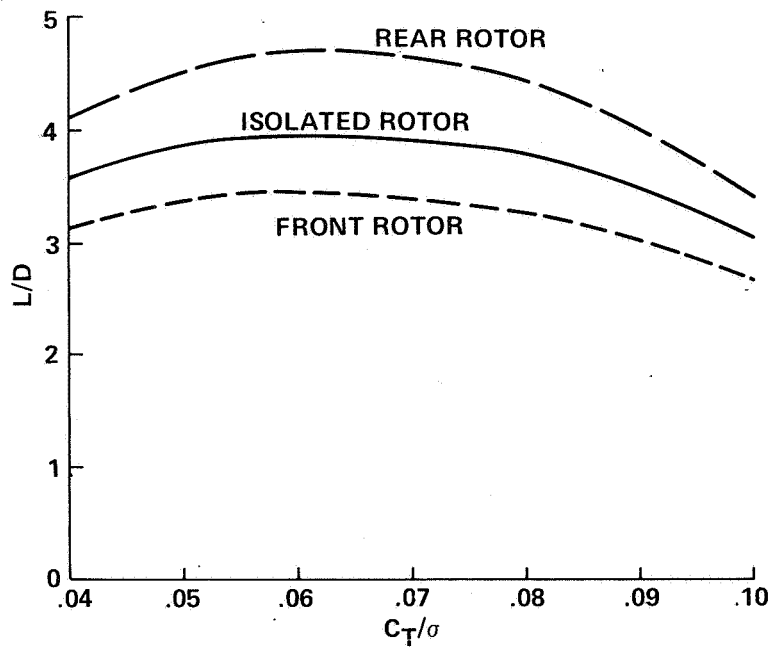


Figure 64.- Lift-to-drag ratio of a front and rear rotor of a typical airship modeled as a 50%-thick ellipsoid (case 5).

1. Report No. NASA TM-85934		2. Government Accession No.		3. Recipient's Catalog No.	
4. Title and Subtitle DEVELOPMENT AND APPLICATION OF AN ANALYSIS OF AXISYMMETRIC BODY EFFECTS ON HELICOPTER ROTOR AERODYNAMICS USING MODIFIED SLENDER BODY THEORY				5. Report Date	
				6. Performing Organization Code	
7. Author(s) Gloria Yamauchi and Wayne Johnson				8. Performing Organization Report No. A-9704	
9. Performing Organization Name and Address NASA Ames Research Center Moffett Field, CA 94035				10. Work Unit No. T-3525	
				11. Contract or Grant No.	
12. Sponsoring Agency Name and Address National Aeronautics and Space Administration Washington, DC 20546				13. Type of Report and Period Covered Technical Memorandum	
				14. Sponsoring Agency Code 505-42-11	
15. Supplementary Notes Point of contact: Gloria Yamauchi, Ames Research Center, MS 247-1, Moffett Field, CA 94035. (415) 965-6719 or FTS 448-6719					
16. Abstract A computationally efficient body analysis designed to couple with a comprehensive helicopter analysis is developed in order to calculate the body-induced aerodynamic effects on rotor performance and loads. A modified slender body theory is used as the body model. With the objective of demonstrating the accuracy, efficiency, and application of the method, the analysis at this stage is restricted to axisymmetric bodies at zero angle of attack. By comparing with results from an exact analysis for simple body shapes, it is found that the modified slender body theory provides an accurate potential flow solution for moderately thick bodies, with only a 10%-20% increase in computational effort over that of an isolated rotor analysis. The computational ease of this method provides a means for routine assessment of body-induced effects on a rotor. Results are given for several configurations that typify those being used in the Ames 40- by 80-Foot Wind Tunnel and in the rotor-body aerodynamic interference tests being conducted at Ames. A rotor-hybrid airship configuration is also analyzed.					
17. Key Words (Suggested by Author(s)) Rotor/body interaction Interactional aerodynamics Axisymmetric bodies				18. Distribution Statement Unlimited Subject Category - 02	
19. Security Classif. (of this report) Unclassified		20. Security Classif. (of this page) Unclassified		21. No. of Pages 119	22. Price* A06